6   LATTICE AND ACCELERATOR PHYSICS

6.1   Lattice and Beam Dynamics

The storage ring lattice is designed to provide a stable, closed orbit on which the electron beam can circulate with long lifetime and efficient injection of beam from the booster. This injection will be capable of filling the ring from zero beam current to the operating values ($\leq$500 mA) in a short time, as well as to provide top-off injection to maintain a constant level of beam current ($<\pm$0.5% variations) and thus provide a constant radiated beam power on the users' beamline components, with low thermal distortions.

The electron beam will be damped by the synchrotron radiation to a small beam emittance lower than that of any storage ring light source currently operating or under construction. The photon beams radiated from undulators will, therefore, have lower emittance and higher brilliance, surpassing any existing light sources in the 2 to 10 keV range in focused beam flux on small specimens.

6.1.1   Physics and Design Goals for the Storage Ring Lattice

The design of the NSLS-II storage ring is driven by goals required to achieve the baseline performance as well as challenge goals that will provide the potential for future upgrades of beam performance. The challenge goals will keep NSLS-II at the frontier of the field for an extended time. Table 6.1.1 lists the required and challenge goals.

Table 6.1.1   Goals for the NSLS-II Design.

Beam Property	Required Goal	Challenge Goal
Ultra low horizontal emittance [nm-rad]	$\leq$1.5 (achromatic)	$\leq$0.5
Vertical emittance [nm-rad]	0.010	0.008
Stored currents [mA]	500	750
ID straights for undulators	$\geq$21	$\geq$25
Electron beam stability [µm]	1	<1
Top-off injection current stability (Δt $\geq$2 min) [%]	<1	<0.1

Several lattices have been studied over the past few years. As work progressed, it became clear that the Double Bend Achromatic lattice could meet the emittance goals while providing an increased number of insertion device straight sections. To achieve our low emittance goals, we maintain achromatic arcs and install damping wigglers in the extra ID straight sections to enhance the SR power without significantly increasing the quantum excitation of the electron beam [6.1.1]. This process yields a net reduction of the beam emittance proportionally related to the ratio of dipole-radiated power to the DW-radiated power, reducing the beam emittance up to five-fold without significantly impacting the DA performance of the ring.

The minimum emittance for a DBA lattice with 2M dipole magnets and electron energy $E_0=\gamma mc^2$ is given by

$$\varepsilon_0^{\min} = \left(7.7 \times 10^{-4}\, nm - rad\right)\gamma^2 / M^3. \tag{6.1-1}$$

The achievable emittance for a realistic lattice design is about twice this minimum value. The momentum compaction is

$$\alpha = \frac{\pi^2}{6M^2} \frac{2\pi \rho_0}{C} ,$$

(6.1-2)

where ρ_0 is the dipole magnet bending radius and C is the ring circumference. Note that the momentum compaction increases linearly with bend radius.

The emittance ε_w with damping wigglers is related to that without damping wigglers, ε_0, by $\varepsilon_w \approx \varepsilon_0 /(1+U_w / U_0)$, where U_w / U_0 is the ratio of the energy lost per turn in the wigglers to that lost in the dipoles. For NSLS-II, we chose to have a large dipole bending radius. This reduces the energy radiated in the dipoles, which means we need to radiate less energy in the wigglers to reduce the emittance by a given factor.

To be more precise, consider a wiggler of length L_w having bending radius ρ_w and period λ_w centered in the insertion section. The ratio of the fractional energy spread with the wiggler to that without is

$$\frac{\delta_w}{\delta_0} = \sqrt{\left[1 + \frac{L_w}{2\pi \rho_0} \frac{4}{3\pi} \left(\frac{\rho_0}{\rho_w}\right)^3\right]\left[1 + \frac{L_w}{4\pi \rho_0} \left(\frac{\rho_0}{\rho_w}\right)^2\right]^{-1}} ,$$

(6.1-3)

and the ratio of the emittance with the wiggler to that without is

$$\frac{\varepsilon_w}{\varepsilon_0} = \frac{1 + f}{1 + \frac{L_w}{4\pi \rho_0}\left(\frac{\rho_0}{\rho_w}\right)^2} .$$

(6.1-4)

The fluctuation factor, f, is given by

$$f = \frac{2C_q \gamma^2}{3\pi^2 \varepsilon_0} \frac{L_w \rho_0}{\rho_w^3} \left[\frac{K_w^2}{5\gamma^2}\langle\beta_x\rangle + \frac{\eta_0^2}{\beta_{x0}} + \beta_{x0}\eta_1^2\right] ,$$

(6.1-5)

where $C_q = 3.84 \times 10^{-13}$ m, and strength parameter $K_w = \lambda_w \gamma / 2\pi\rho_w$. The horizontal beta function is given by $\beta_x (s) = \beta_{x0} + s^2 / \beta_{x0}$, where $s = 0$ is the center of the wiggler and insertion, and $\langle\beta_x\rangle$ denotes the average value of β_x in the wiggler. We express the dispersion function in the wiggler in the form $\eta(s) = \eta_w(s) + \eta_0 + \eta_1 s$, where $\eta_w(s)$ is the sinusoidal dispersion generated by the wiggler itself, and $\eta_0 + \eta_1 s$ is the dispersion generated by errors elsewhere in the ring. Eq. (6.1-5) can be used to determine a tolerance on the dispersion in the insertions arising from errors.

As at ESRF, the NSLS-II lattice has alternating high and low horizontal beta function straight sections for insertion devices. A large value of β_x is desired at the injection septum. Small β_x is desired in undulators for beamlines designed to focus the radiation down to a small spot. The vertical beta function should be small in undulators to optimize brightness. In fact, it is essential that β_y not be large in any of the insertion devices. The linear tune shift produced by an undulator or wiggler is

$$\Delta\nu_y = \frac{\langle\beta_y\rangle L_w}{8\pi\rho_w^2} .$$

(6.1-6)

Small β_y keeps the tune shift within acceptable limits. We have bounded the straight sections with quadrupole quartets in order to provide a local correction for the modification of the betatron functions and phases due to undulator or wiggler focusing.

The tune shift with amplitude due to nonlinear undulator or wiggler focusing is

$$\frac{d\nu_y}{dJ} = \frac{\pi \left\langle \beta_y^2 \right\rangle L_w}{4\lambda_w^2 \rho_w^2} \ .$$

(6.1-7)

To minimize the effect of the nonlinear focusing on dynamic aperture, it is essential to have small β_y in the insertion devices.

This is the approach taken for NSLS-II [6.1.2]. A DBA with 30 periods was chosen as the lattice structure, with a natural emittance of 2.1 nm. One cell of the lattice, shown in Figure 6.1.1, comprises half a super-period with reflection symmetry about the right or left hand end of the cell. The lattice functions have been optimized to achieve achromatic arcs, low emittance and modest chromatic sextupole strengths, small Closed Orbit Amplification Factors, and desired betatron functions in the long and short straight sections, which are required for small impact on the DA of the IDs, as given by Eq. (6.1-6 and 6.1-7). The working point tune was selected for optimization of the sextupole correction of the nonlinear driving terms that limit the DA, as well as reduced COAF and instability sensitivity. The dipole magnets have been optimized (bend radius $\rho_0 = 25$ m, $B_0 = 0.399$ T at 3 GeV) to enhance the reduction of the beam emittance with the DWs. Although the bare lattice doesn't quite meet the required emittance goal (2.1 nm instead of 1.5 nm), this goal is exceeded with only one 7 m DW installed and operated at a peak field of 1.8 T.

Figure 6.1.1   The lattice functions for one-half of a DBA period. A super-period consists of this cell reflected about either ID center: 8 m on the left-hand side or 5 m on the right.
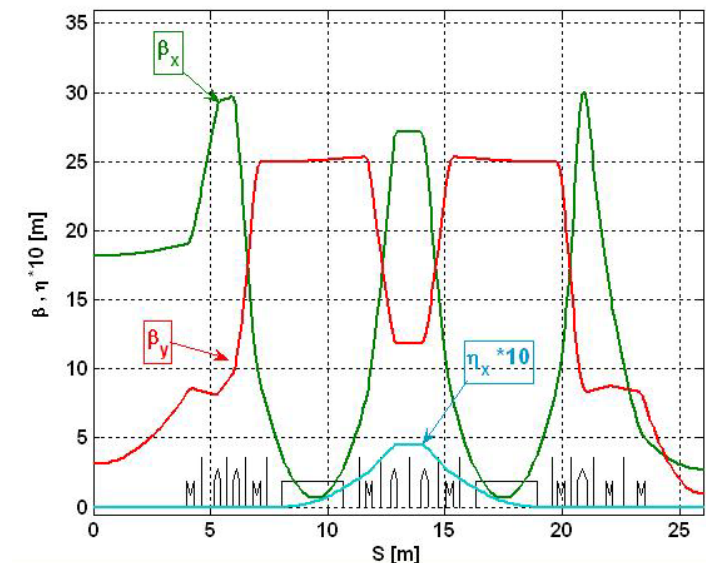
The impact of DWs on the emittance and the energy spread, given by Eq. (6.1-3 and 6.1-4), is shown in Figure 6.1.2 for the designed $\rho_0 = 25$ m and a stronger dipole with 1.5 times the field (2/3 the bend radius). This calculation also assumes no significant spurious dispersion in the straight section, since the individual quadrupole powering in this lattice should allow the dispersion to be corrected cell-by-cell for any dipole variations. The gain in undulator brightness resulting from the smaller emittance provided by more damping wigglers is somewhat reduced by the increased energy spread of the beam, especially at x-ray energies corresponding to higher harmonics of the undulator. Increasing the bend radius from 16.68 m to 25 m reduces both the emittance as well as the energy spread. Continuing to increase the bend radius to larger values is

increasingly less effective at reducing the emittance as it approaches the IBS limit, and at the same time increasingly expensive, as it increases the circumference of the ring. As discussed in Chapter 5, a bend radius of 25 m is about optimal for NSLS-II. The installed RF power also provides a practical limit to the gain from more damping wigglers, since the beam lifetime will be reduced if the radiated power exceeds the installed power necessary for sufficient RF bucket height.

An additional advantage of the low-field dipoles is that their radiated photon energy will be lower than many of the planned ID beams and therefore they will have less impact on the photon beam position monitors used in feedback systems, e.g., as seen at APS [6.1.3]. The photon energy separation between the two beams will allow filters to be used to absorb the dipole beam while the ID photon beam passes through.

Figure 6.1.2   The fractional reduction of the ring emittance and the increase in energy spread for dipole magnets of bend radii: ρ_o = 25 m (proposed for NSLS-II) and ρ_o = 16.7 m dipole that could yield a shorter circumference lattice.
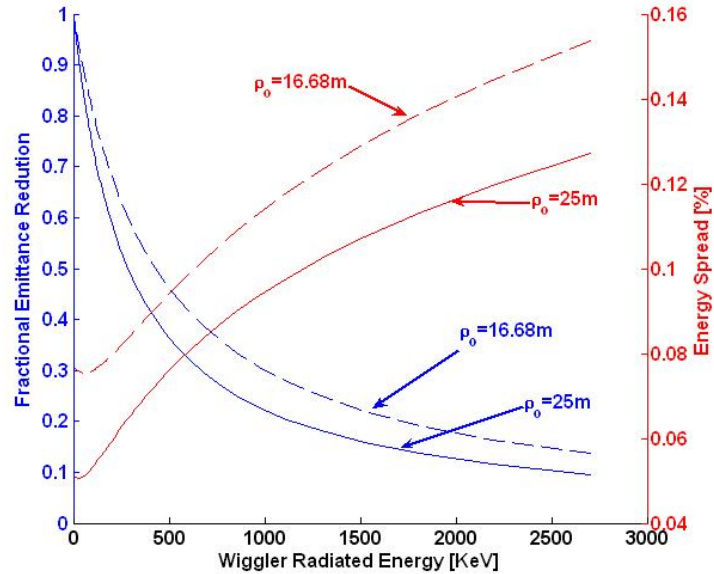
Table 6.1.2 lists the design parameters for this 15 super-period DBA (15×2) lattice. The choice of low dipole field restricts the photon beam energies radiated by the dipoles to 2.4 keV critical energy at 3 GeV. The dipole radiation will provide very bright VUV and soft-x-ray beams. Hard x-rays will be available from the installed DWs (10.8 keV critical energy) with high brilliance and flux.

Table 6.1.2   Storage Ring Parameters.

Energy [GeV]	3
Circumference [m]	780
DBA cells	30 (15 x 2)
Bending radius [m]	25.019
RF frequency [MHz]	499.46
Momentum compaction	0.000368
Tune: v_x, v_y	32.35, 16.28
Natural chromaticity: ξ_x, ξ_y	–100, –41.8
Maximum dispersion [m]	0.45
High-beta 8-m straights: β_x, β_y [m]	18, 3.1
Low-beta 5-m straights: β_x, β_y [m]	2.7, 0.95
Dipole radiated energy loss [keV]	286.5
Dipole critical energy [keV]	2.394

Figure 6.1.3 shows the expected reduction of the emittance as one to eight 7 m DWs are added to the ring.
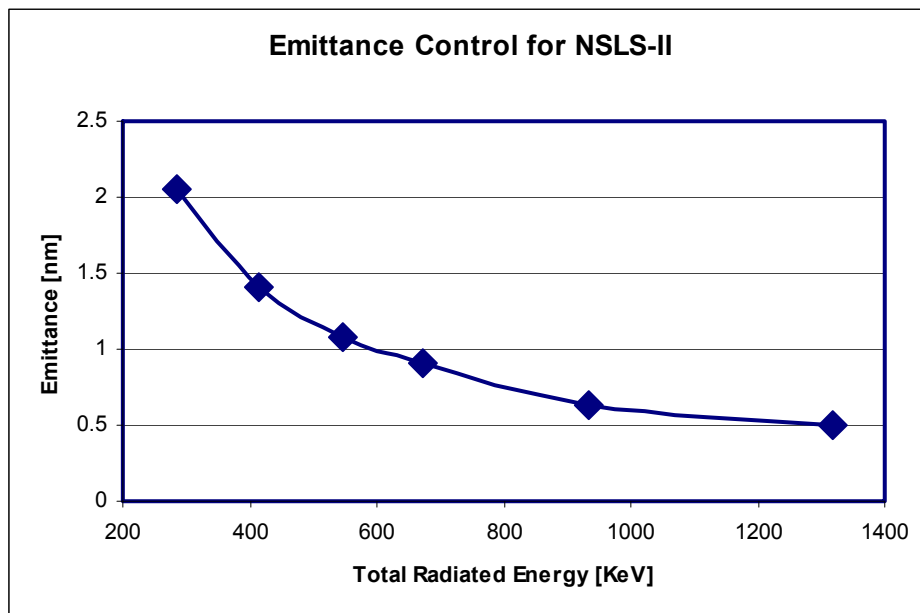

Figure 6.1.3
Emittance reduction for NSLS-II as 0, 1, 2, 3, 5, and 8 DW (7 m each) are installed and operated at 1.8 T peak field.

Table 6.1.3 compares the basic lattice properties with those obtained with 21 or 56 m of DWs installed in the ring. All of these DWs will have a fixed gap and will be available to drive user beamlines.

Table 6.1.3   Effect of Three and Eight 7 m Damping Wigglers on Beam Properties at 3 GeV.

	Zero DWs	Three 7 m DWs (21 m)	Eight 7 m DWs (56 m)
Energy loss [keV]	287	674	1320
RF voltage (3% bucket) [MV]	2.5	3.1	3.9
Synchrotron tune	0.0079	0.00876	0.0096
Natural emittance: ε_x, ε_y [nm-rad]	2.1, 0.01	0.91, 0.008	0.50, 0.005
Damping time: τ_x, τ_s [ms]	54, 27	23, 11.5	12, 6
Energy spread [%]	0.05	0.089	0.099
Bunch duration [ps]	10	15.4	15.5

The lattice shown in Figure 6.1.1, like that at ESRF, has low and high beta function straight sections. However, we have increased the length of the high-β_x straight section to provide for injection, space for RF cavities, and space for longer DWs and user IDs. The drift space between quadrupole magnets is 8 m. The space available for insertion devices is 7 m. The magnet layout for the long ID straight section, with 8 m inner quadrupole spacing, is shown in Figure 6.1.4. Half the long ID is shown with reflective symmetry about the centerline (left-hand side). There are a total of eight quadrupoles (Q1, Q4×2) and eight sextupoles (S1, S4×2) in each ID straight section. Although they are considered as four families of focusing strengths, they will be independently powered to account for magnet-to-magnet differences and for the possibility of shifting the symmetry condition for improved photon beam focusing. The four quadrupole families provide sufficient parameters for correcting the local distortions of the linear lattice when IDs are installed or when the gaps are changed by the users [6.1.4, 6.1.5]. The four families of sextupoles in each long ID are required in order to correct the nonlinearity of the lattice arising from the strong chromatic sextupoles located in the dispersive

regions. For certain working points, some sextupoles have small strengths. These might be dropped from a future optimized design.
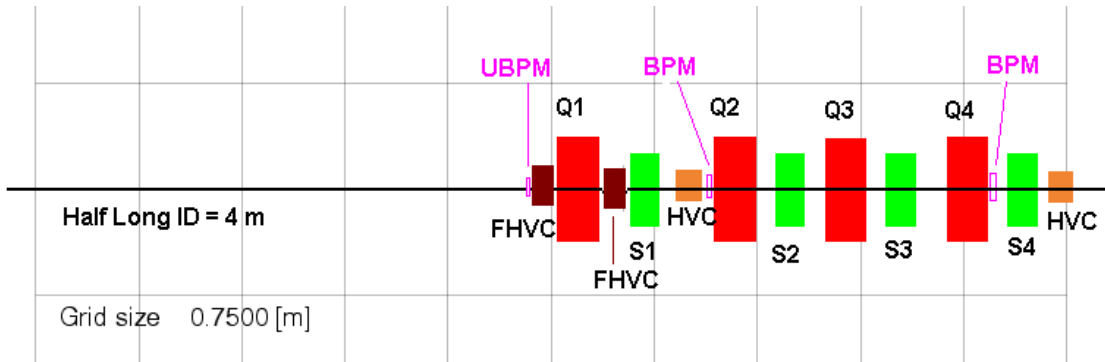

Figure 6.1.4   Layout for half of a long ID straight section, with reflection symmetry on left side.

The short ID straight section layout is shown in Figure 6.1.5. The short ID has a 5 m drift between the inner quadrupoles and is similar to the long ID in layout of the quadrupoles and sextupole families. Differences include additional drift between quadrupoles to reduce the chromaticity, while providing the increased focusing needed for the lower beta functions. To meet the maximum gradient values, one quadrupole (Q33) must be longer than those in the long ID straight section.
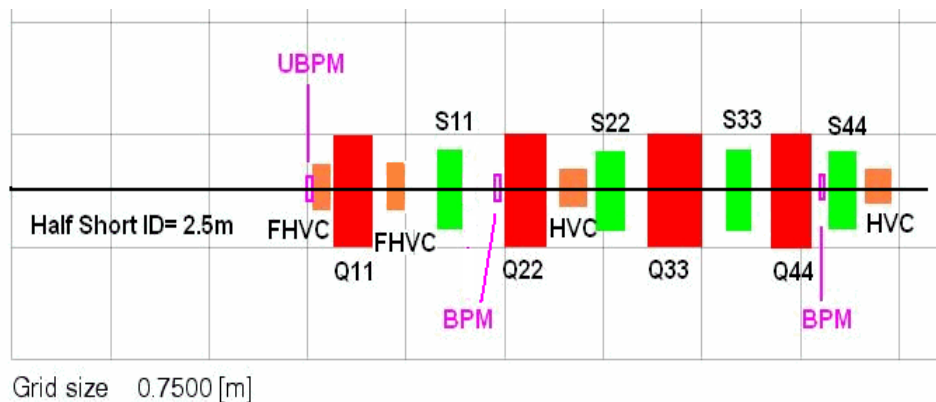

Figure 6.1.5   Layout for half of a short ID straight section, with reflection symmetry on left side.

Two slow horizontal and vertical closed-orbit correction magnets are included in each ID straight section (some also include a skew quadrupole winding). For the purposes of this conceptual design,, we assume independent corrector magnets, as shown in Figures 6.1.4 and 6.1.5. Also shown are two beam position monitors to be used for closed-orbit correction. When a user ID is installed in the ring, it is assumed that two pairs of fast horizontal and vertical correctors and a pair of user BPMs will also be installed. These will be optimized for the aperture of the ID vacuum chamber to yield increased sensitivity to orbit motion and the increased frequency of correction for fast orbit motion required for the ID beamline. To accomplish this will require some advanced engineering, but there is adequate drift space provided. The FHVCs and UBPMs will be used as part of a local feedback system to provide submicron photon beam stability up to 100 Hz. Since the four FHVCs will provide a closed bump, the possibility of adding a photon beam position signal to the feedback system will also be available, without that signal impacting the beam for other users.

Figure 6.1.6 shows the magnet layout for the dispersion region of the lattice with the dipoles included. This region has four quadrupoles in two families and five sextupoles in three families. These magnets give some flexibility for optimizing the dispersion function for reduced chromatic sextupole strength. The third chromatic sextupole allows the linear chromaticity to be compensated, while reducing the higher-order chromatic terms. As in the ID straight sections, two BPMs are included close to the quadrupoles near the ends of the girder. This is to provide improved alignment of the magnets on the girder using a beam based alignment of the BPM to the quadrupoles magnetic center. A third BPM is included near the QF quadrupole (near the maximum dispersion point). This BPM will be used for accelerator physics measurements of the dispersion and beta functions, when needed, and will improve the orbit correction for random alignment errors. Also included are three discrete HVC correctors that will be used for static and global orbit correction. However, since the vertical beta function is small in the middle corrector, only a horizontal correction power supply will be provided in this corrector.
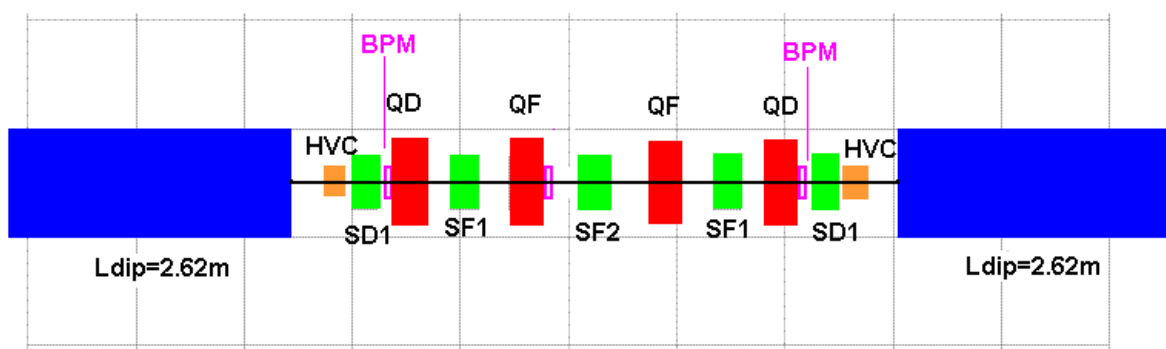

Figure 6.1.6   Layout for the dispersion section, including the two dipole magnets.

Table 6.1.4 lists a summary of the basic storage ring beam components and BPMs in the lattice design and closed-orbit control. Details on the maximum values and tolerances of these magnets are listed in Section 8.1.1.

Table 6.1.4   List of Magnets and BPMs for the NSLS-II Storage Ring.

No. of Elements	Type of Element	Length [m]
60	Dipole	2.62
330	Quadrupole (S)	0.3
30	Quadrupole (L)	0.4
30	Sextupole (L)	0.30
120	Sextupole (M)	0.25
240	Sextupole(S)	0.20
180	H+V Corrector (30 H only PS)	0.15
30	H+V + SQ Corrector (1 SQ per cell)	0.15
210	BPM electronics	0.05
≤20 (initial)	Fast H+V Corrector (as required)	0.10
≤10 (initial)	User ID BPM (2 per ID)	0.10

6.1.2   Nonlinear Dynamics

6.1.2.1   Guidelines

One of the main design challenges for a strongly focusing lattice is to obtain adequate dynamic aperture for injection and Touschek lifetime[1]. As the required strength of the chromatic sextupoles increases, the DA can be improved by introducing extra families of geometric and chromatic sextupoles. However, once the sextupoles become too strong, this is no longer feasible. Eventually, cross terms generate higher-order terms, and when more families are introduced, the lattice will become pathological [6.1.5]. To avoid this, the following guideline has been provided for the linear optics design:

- horizontal chromaticity per cell, $\xi_x \sim 3$,
- peak dispersion, $\eta_x \sim 0.3$ m.

Similarly, we have adopted the guidelines for the DA summarized in Table 6.1.5. This is a conservative approach[2] to satisfy the requirements for the injection aperture for efficient top-off, as well as to ensure sufficient Touschek lifetime.

Table 6.1.5   Dynamic Aperture Guidelines.

	Horizontal and Vertical Dynamic Acceptance [mm·mrad]	Horizontal Dynamic Aperture [mm]	Momentum Acceptance [%]
Bare lattice (2.5 degrees of freedom[3])	~25	±20	±3
"Real" lattice (3 degrees of freedom[4])	~20	±15	±3

This also provides some leeway for magnetic alignment and field tolerances, and nonlinearities due to insertion devices, which, when included, perturb the symmetry of the linear optics and diminish the cancellation of the nonlinear effects, reducing the DA.

6.1.2.2   Sextupole Scheme

The linear lattice has a chromaticity of $\xi_{x,y}^{(1)} \sim (-100, -42)$ and a natural momentum spread of ~0.1% leading to a tune spread of $\Delta \nu_{x,y} \sim (0.1, 0.04)$, which must be corrected[5]. The linear chromaticity is given by

$$\xi_{x,y}^{(1)} = \mp \frac{1}{4\pi} \sum_{k=1}^{N} \left[(b_2 L)_k - 2(b_3 L)_k \eta_{x,k} \right] \beta_{(x,y),k}, \qquad (6.1-8)$$

where (b_2L), (b_3L) are the integrated quadrupole and sextupole strengths, and β and η are the beta function and dispersion, respectively at the quadrupoles and sextupoles, k. The driving terms for linear chromaticity from sextupoles are shown in Figure 6.1.7. Three mirror symmetric chromatic families are introduced inside the dispersion section and 4+4 geometric families in the short and long straight sections, i.e., a total of 11

---

[1] For medium energy rings: ~3 GeV.

[2] Based on the experience from the Swiss Light Source conceptual design, i.e., a highly nonlinear lattice [6.1.6] with straightforward commissioning [6.1.7], excellent top-off injection efficiency [6.1.8], and stability [6.1.9].

[3] With δ (momentum deviation) treated as a parameter, i.e., the adiabatic approximation.

[4] In particular, with synchrotron oscillations.

[5] Moreover, a positive linear chromaticity in the range 0–5 is required to stabilize the head-tail instability.

sextupole families. While a few of the families in the matching sections tend to be weak, they have been left as place holders until a more comprehensive optimization has been completed. Independent power supplies for all the quadrupoles and sextupoles are provided, to allow for local optics correction [6.1.10–6.1.16] and control of residual nonlinear resonances [6.1.17].
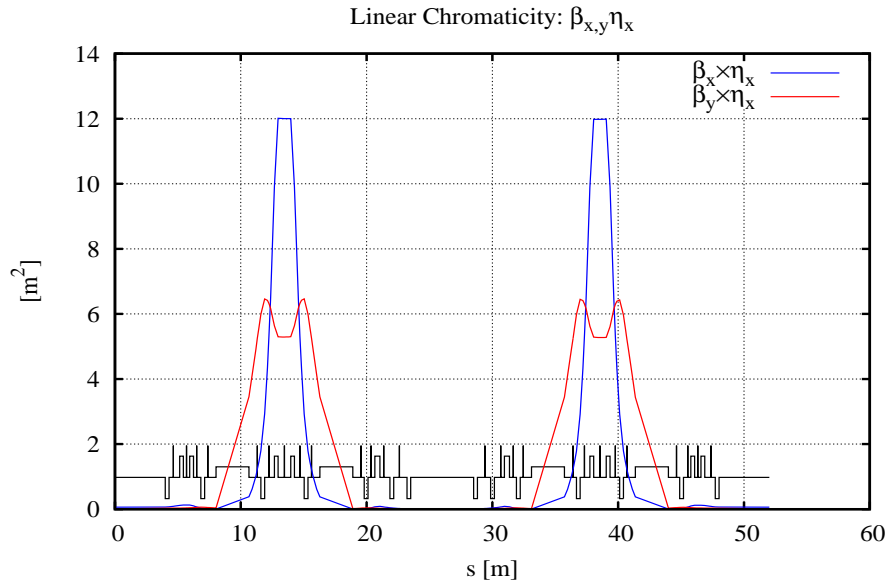

Figure 6.1.7 Driving terms for zeroing linear chromaticity with sextupoles, $\beta_{x,y}\, \eta_x$.

After linear chromaticity has been zeroed, the nonlinear chromaticity may be a limiting factor. The second-order chromaticity is given by 0:

$$\xi_{x,y}^{(2)} = -\frac{1}{2}\xi_{x,y}^{(1)} + \frac{1}{8\pi}\sum_{k=1}^{N}\left\{2(b_3L)_k\frac{\partial\eta_{x,k}}{\partial\delta}\beta_{(x,y),k} - \left[(b_2L)_k - 2(b_3L)_k\eta_{x,k}\right]\frac{\partial\beta_{(x,y),k}}{\partial\delta}\right\}$$
(6.1-9)

The driving terms are shown in Figures 6.1.8 and 6.1.9. Clearly, small variations of the sextupole locations may lead to large changes of the nonlinear chromaticity[6]. In particular, the rather large second-order horizontal dispersion leads to a substantial residual cubic term in the horizontal chromaticity [6.1.19] as discussed in Section 6.1.2.3. As a further refinement, this term should be controlled by including the driving term in the linear optics optimizations.

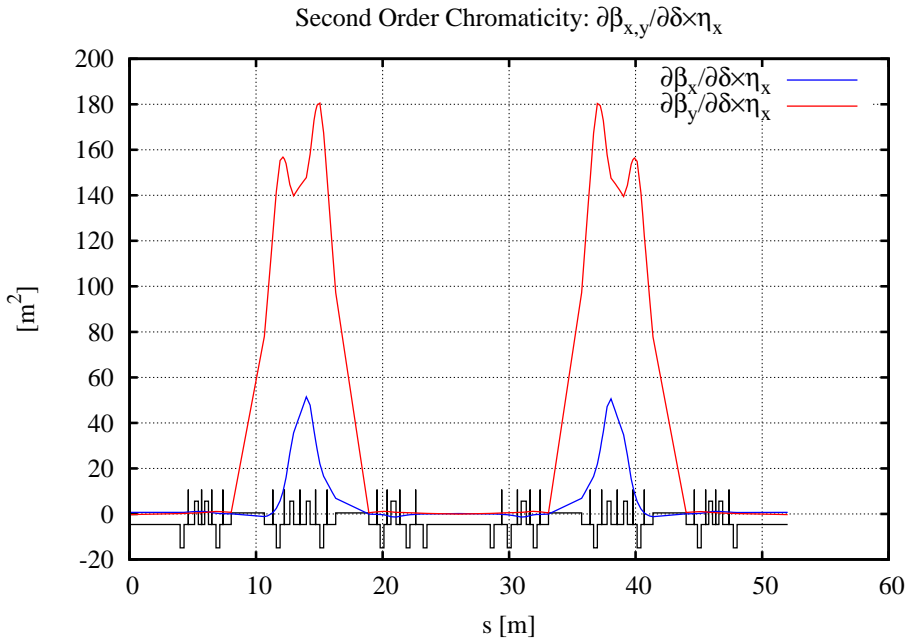[6] As noted from numerical simulations for the DIAMOND conceptual design [6.1.18].

Second Order Chromaticity: $\partial\beta_{x,y}/\partial\delta\times\eta_x$

Figure 6.1.8 Driving terms for second-order chromaticity, $\partial\beta_{x,y}/\partial\delta\times\eta_x$.

Second Order Chromaticity: $\beta_{x,y}\times\partial\eta_x/\partial\delta$
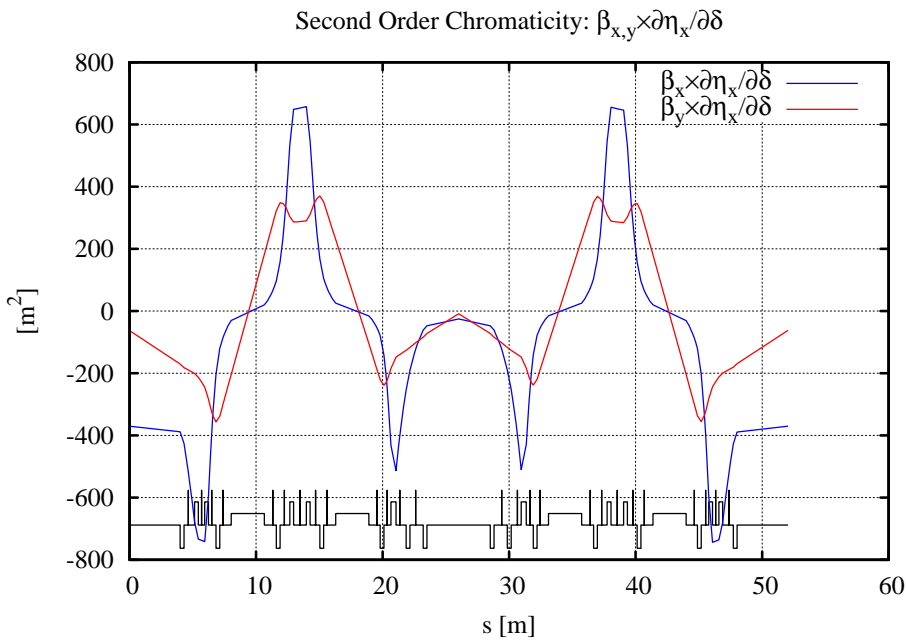

Figure 6.1.9 Driving terms for second-order chromaticity, $\beta_{x,y}\partial\eta_x/\partial\delta$.

6.1.2.3   Dynamic Aperture Optimization

The Poincaré map has the formal Lie series representation [6.1.17]:

$$\mathcal{M} = e^{:h:}\mathcal{M}_{\text{linear}}$$

(6.1-10)

where $\mathcal{M}_{\text{linear}}$ is the linear one-turn map, and the Lie generator h represents the nonlinear kicks transferred to the entrance of the lattice. In particular, the first-order generators have the form:

$$h_3 = \sum_J h_{jklmp}\left(2J_x\right)^{(j+k)/2}\left(2J_y\right)^{(l+m)/2}\delta^p e^{i\left[(j-k)\phi_x+(l-m)\phi_y\right]} + \text{c.c.},$$

$$h_{jklmp} = h^*_{kjmlp} = \sum_{n=1}^{N}\left(b_3 L\right)_n \beta_{xn}^{(j+k)/2}\beta_{yn}^{(l+m)/2}\eta_x^p e^{i\left[(j-k)\mu_{xn}+(l-m)\mu_{yn}\right]} \qquad (6.1\text{-}11)$$

where J, ϕ are the action-angle variables and β, μ the beta functions and phase advances at the sextupoles, n.

In contrast to the linear case, the long-term stability now depends on: $\mathcal{M}_{\text{linear}}$ (i.e., the tune), h, and the initial conditions. In other words, for a systematic approach, the Lie generator and the working point have to be optimized simultaneously. We have implemented a generalized third-order achromat by introducing 11 sextupole families to the super-period, and minimized h over two super-periods, i.e., four DBA cells, for a range of cell tunes. At each working point with optimized sextupole strengths, we evaluated the DA by tracking. To the second order in the sextupole strengths, there are:

- 2+3+2 chromatic terms
- 5+8 geometric terms (modes)
- 3+3 tune shift with amplitude and momentum

This is a total of 26 terms[7] (see Table 6.1.6 for an inventory). These are minimized by varying the sextupole strengths using the following automated method[8] [6.1.5]:

1. For a given cell tune, the Lie generator h and its parametric dependence on the sextupole strengths (i.e., the Jacobian) are calculated for $J_{x,y}$ and δ at the anticipated DA.
2. The norm of $\|h\|$ is minimized[9] and the DA is evaluated by tracking.
3. The cell tune is changed by adjusting the quadrupoles in the matching sections and steps 1–3 are repeated.

The off-momentum aperture is included by using a weighted average for the DA at $\delta = 0, \pm 3\%$. A robust solution is obtained by establishing a broad local maximum for the DA. The tune scan presented in Figure 6.1.10 shows a broad maximum for the DA centered near $(v_x, v_y)=(2.115, 1.105)$ per super-period.

---

[7] The corresponding overconstrained system of nonlinear equations for the sextupole strengths can be minimized because of symmetry and the fact that the higher order terms are due to cross terms of the lower order.

[8] Feasible only because of the use of symmetry and the fact that the higher order terms appear due to cross terms of the lower order.

[9] In particular, a least-square of the individual terms.
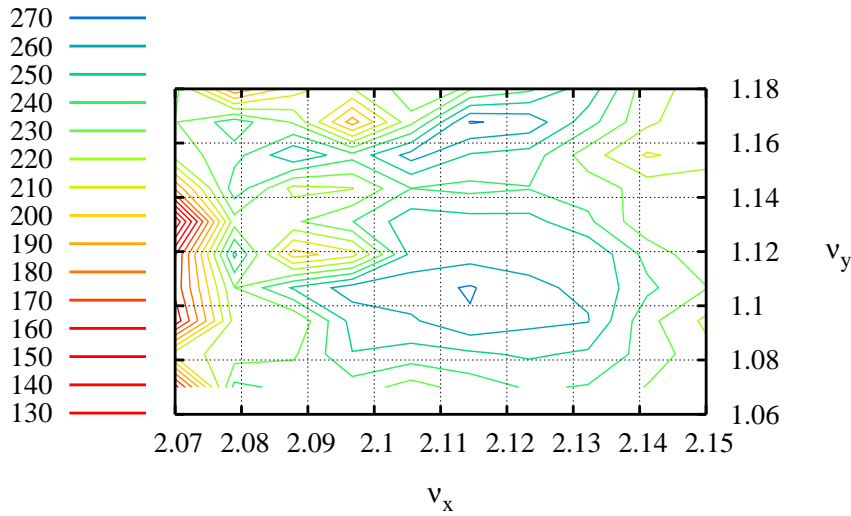
Normalized Dynamic Aperture (bare lattice, N=2)

Figure 6.1.10 Normalized DA ($\mathrm{Area}/\sqrt{\beta_x \beta_y}$) vs. tune per super-period.

The resulting DA is shown in Figure 6.1.11, for $\delta = 0, \pm3\%$.
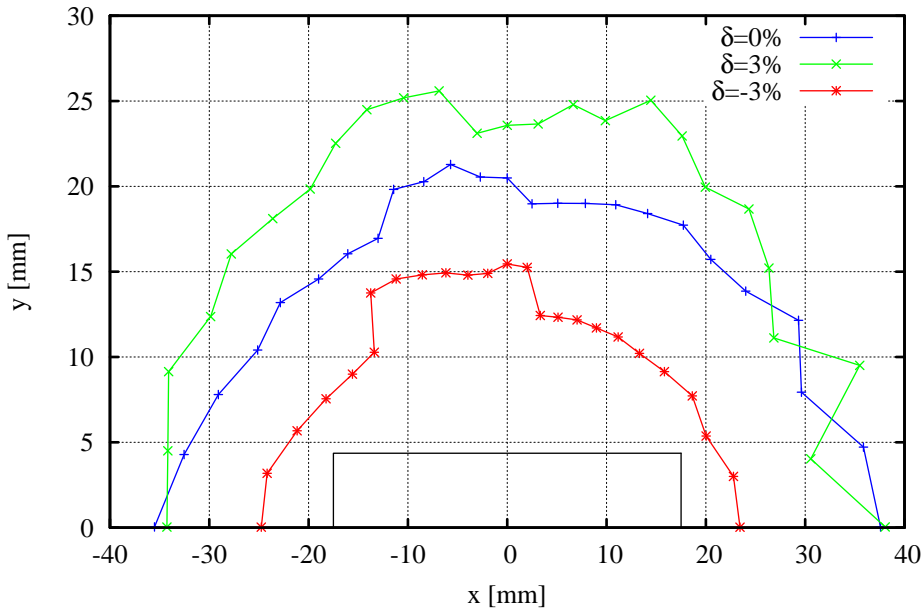
Dynamic Aperture (bare lattice, 2.5 DOF)

Figure 6.1.11 DA for $\delta = 0$, $\pm3\%$ for the optimized tune and sextupoles at the center of the long straight section (i.e., at injection), $\beta_{x,y}$ = (18.2, 3.2) m.

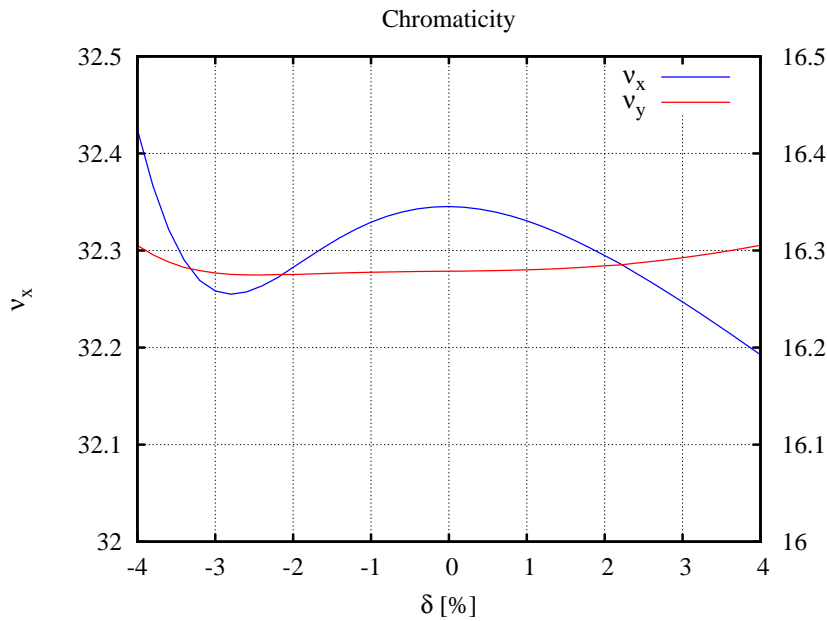The linear chromaticity is zeroed, and the residual nonlinear chromaticity is shown in Figure 6.1.12.

Chromaticity

Figure 6.1.12   Residual nonlinear chromaticity for the optimized tune and sextupoles.

As mentioned earlier, the horizontal chromaticity has a substantial cubic term originating from h_{10002} driving second-order dispersion. The crossing between the horizontal and vertical tunes during synchrotron oscillations should be avoided in further optimizations. Otherwise, the Touschek lifetime can be affected. The amplitude-dependent tune shifts are shown in Figures 6.1.13 and 6.1.14, and the residual Lie generators are listed in Table 6.1.6.
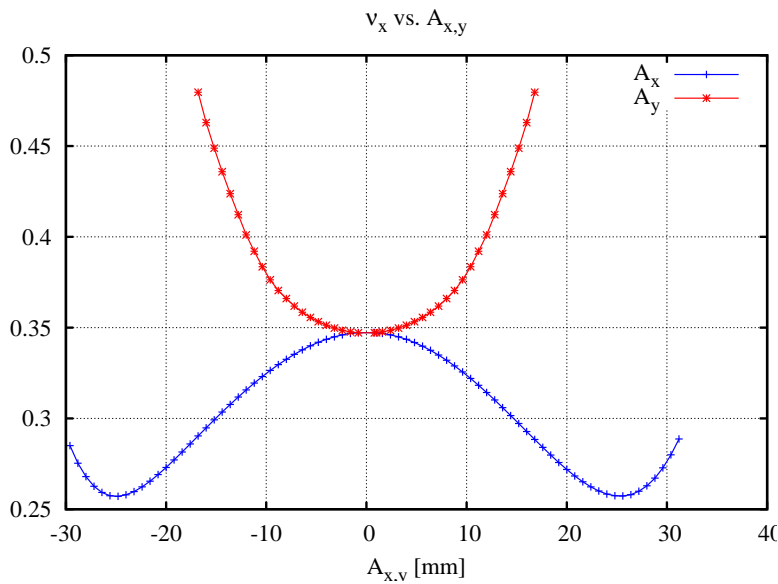
ν_x vs. $A_{x,y}$

Figure 6.1.13   Horizontal tune, v_x, vs. transverse amplitude (x_0, y_0) at the long straight section for $A_x = (x_0, y_0{\sim}0)$ and $A_y = (x_0{\sim}0, y_0)$.
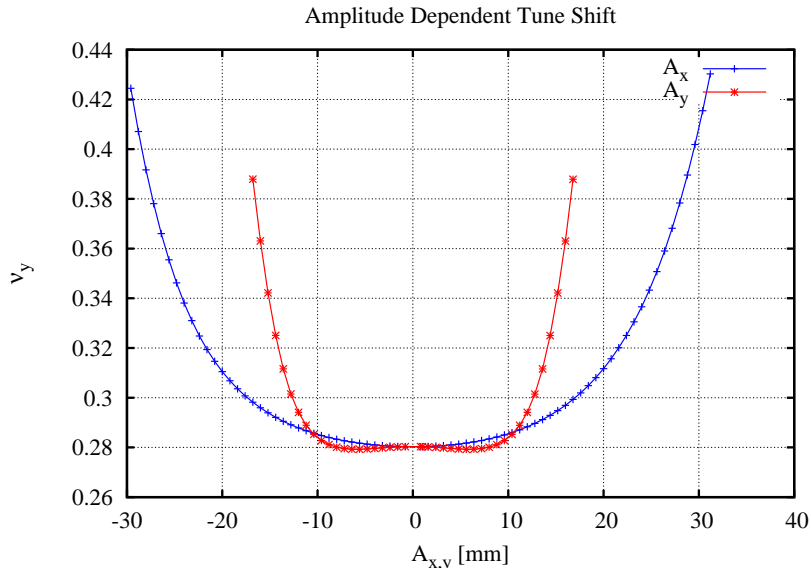
Figure 6.1.14 Vertical tune, v_y, vs. transverse amplitude (x_0, y_0) at the long straight section for: $A_x = (x_0, y_0 \sim 0)$ and $A_y = (x_0 \sim 0, y_0)$.

A frequency map [6.1.15] shows diffusion rate as a function of amplitude or tunes. The diffusion rate, as defined by

$$D\left(v_x, v_y\right) = \log_{10}\left(\sqrt{\left(\Delta v_x\right)^2 + \left(\Delta v_y\right)^2} \right),$$

(6.1-12)

is an indicator of chaotic behavior, where Δv is the tune change between the first and second half of the particle tracking with initial amplitude $J_{x,y}$. The frequency map for the optimized working point and sextupole settings for zero linear chromaticity is shown in Figure 6.1.15, with the diffusion parameter plotted as a color-weighted value. Note that increased diffusion occurs at $A_x \sim 25$ mm and $A_y \sim 8$ mm, because $\partial v/\partial A = 0$. Hence, as a further refinement, it could be avoided by also controlling the derivative of the amplitude-dependent tune shifts at these large amplitudes.

Table 6.1.6   Residual Normalized Lie Generators.

Lie Generator	Effect	Normalized Value
$\left\| h_{11001} \right\|$	$\partial \nu_x / \partial \delta$	1.6×10^{-11}
$\left\| h_{00111} \right\|$	$\partial \nu_y / \partial \delta$	1.3×10^{-12}
$\left\| h_{10002} \right\|$	$\partial \eta_x / \partial \delta$	3.3×10^{-6}
$\left\| h_{20001} \right\|$	$\nu_x \pm \nu_s$	6.0×10^{-7}
$\left\| h_{00201} \right\|$	$\nu_y \pm \nu_s$	3.5×10^{-8}
$\left\| h_{21000} \right\|$	ν_x	6.4×10^{-7}
$\left\| h_{10110} \right\|$	ν_x	1.5×10^{-7}
$\left\| h_{30000} \right\|$	$3\nu_x$	2.1×10^{-8}
$\left\| h_{10020} \right\|$	$\nu_x - 2\nu_y$	5.4×10^{-8}
$\left\| h_{10200} \right\|$	$\nu_x + 2\nu_y$	7.1×10^{-7}
$\left\| h_{20110} \right\|$	$2\nu_x$	2.2×10^{-8}
$\left\| h_{31000} \right\|$	$2\nu_x$	8.8×10^{-8}
$\left\| h_{40000} \right\|$	$4\nu_x$	7.4×10^{-9}
$\left\| h_{20020} \right\|$	$2\nu_x - 2\nu_y$	3.4×10^{-7}

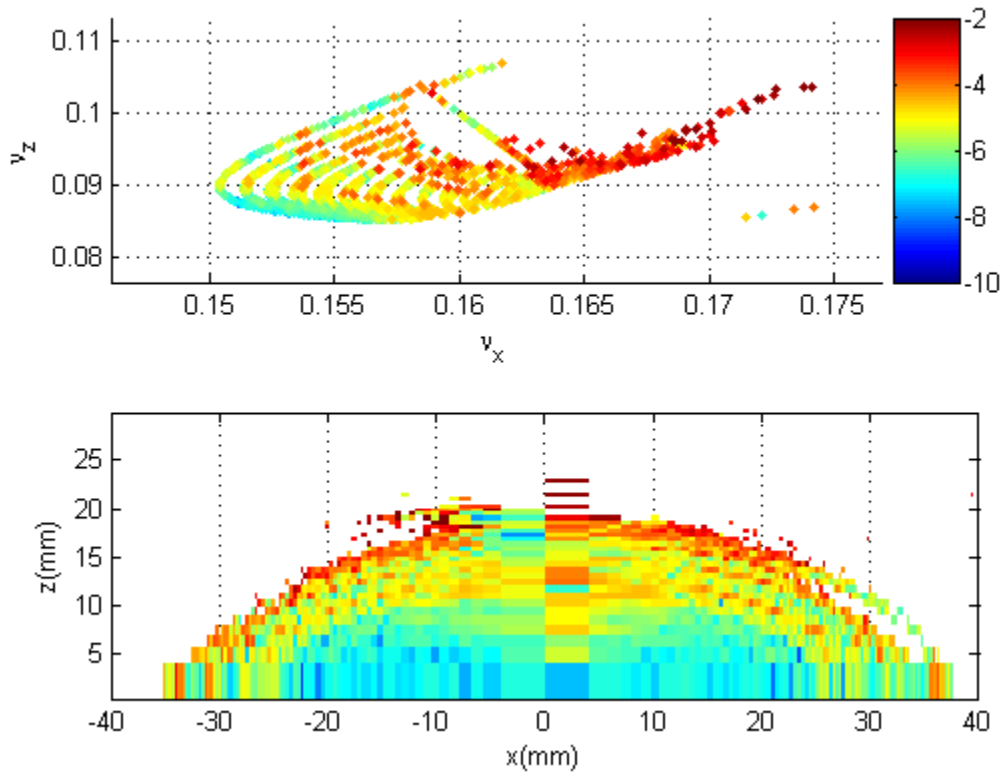| Lie Generator	Effect	Normalized Value
$\left\| h_{20200} \right\|$	$2\nu_x + 2\nu_y$	1.3×10^{-9}
$\left\| h_{11200} \right\|$	$2\nu_y$	5.5×10^{-8}
$\left\| h_{00310} \right\|$	$2\nu_y$	1.5×10^{-7}
$\left\| h_{00400} \right\|$	$4\nu_y$	2.3×10^{-8}
$\left\| h_{22000} \right\|$	$\partial \nu_x / \partial J_x$	1.1×10^{-6}
$\left\| h_{11110} \right\|$	$\partial \nu_{x,y} / \partial J_{y,x}$	1.3×10^{-7}
$\left\| h_{00220} \right\|$	$\partial \nu_y / \partial J_y$	6.9×10^{-7}
$\left\| h_{22001} \right\|$	$\partial^2 \nu_x / \partial J_x \partial \delta$	7.0×10^{-7}
$\left\| h_{11111} \right\|$	$\partial^2 \nu_{x,y} / \partial J_{y,x} \partial \delta$	3.7×10^{-7}
$\left\| h_{00221} \right\|$	$\partial^2 \nu_y / \partial J_y \partial \delta$	7.6×10^{-8}
$\left\| h_{11002} \right\|$	$\partial^2 \nu_x / \partial \delta^2$	3.9×10^{-6}
$\left\| h_{00112} \right\|$	$\partial^2 \nu_y / \partial \delta^2$	1.1×10^{-7}

Figure 6.1.15   Frequency map vs. transverse amplitudes at the Long Straight Section, $\beta_{x,y}$ = (18.2, 3.2) m.

6.1.2.4   Impact of Alignment and Field Tolerances on Dynamic Aperture

Systematic and random magnetic field errors further reduce the DA, and their impact has been evaluated by simulations. Figure 6.1.16 shows the impact on the DA as the random quadrupole gradient errors are increased for all the quadrupoles of the lattice. At a relative RMS error of $\Delta b_2/b_2 \approx 5 \times 10^{-4}$, they reduce the DA by ~20%, which is taken as the tolerance level for the quadrupole powering errors.
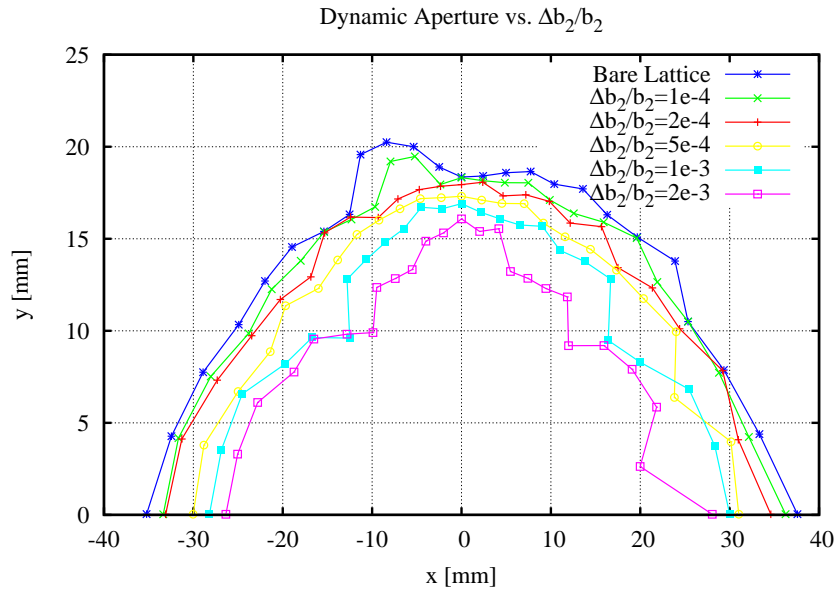
Dynamic Aperture vs. $\Delta b_2/b_2$

Figure 6.1.16 DA sensitivity versus the fractional gradient errors in the quadrupoles.

This reduction in DA originates from distortions of the linear optics at the sextupole magnets that perturb the influence of the carefully balanced sextupole strengths that were chosen to minimize the nonlinear driving terms. The resulting RMS beta and phase advance beats at the sextupoles can therefore be used as a tolerance level, regardless of their source [6.1.20]. These latter tolerance levels, as well as the gradient tolerance level, are listed in Table 6.1.7.

Table 6.1.7   Optics Tolerances for Robust DA of the NSLS-II Lattice.

Location	At the Quadrupoles	At the Sextupoles		
Parameter	$\left(\dfrac{\Delta b_2 L}{b_2 L}\right)_{\text{rms}}$	$\left(\dfrac{\Delta \beta_{x,y}}{\beta_{x,y}}\right)_{\text{rms}}$	$\left(\Delta \nu_{x,y}\right)_{\text{rms}}$	$\left(\Delta x_{\text{cod}}, \Delta y_{\text{cod}}\right)_{\text{rms}}$
Tolerance	$\sim 5 \times 10^{-4}$	$\sim (0.02, 0.03)$	$\sim (0.003, 0.01)$	$\sim (50, 50)_{\mu m}$

Similarly, a tolerance level can be specified for the residual Closed-Orbit Distortions at the sextupoles, which introduce beta and phase advance beats proportional to the sextupole gradients times the COD offset. This impact on the DA was simulated by introducing random transverse alignment errors to all the sextupoles and is shown in Figure 6.1.17 vs. the RMS error. At a level of $\sigma_x = \sigma_y \sim 50$ µm, the DA area is reduced by about 20%. These RMS values can be taken as the tolerance level for the misalignments and residual COD at the sextupoles that must be maintained by the global orbit correction system (see Table 6.1.7).
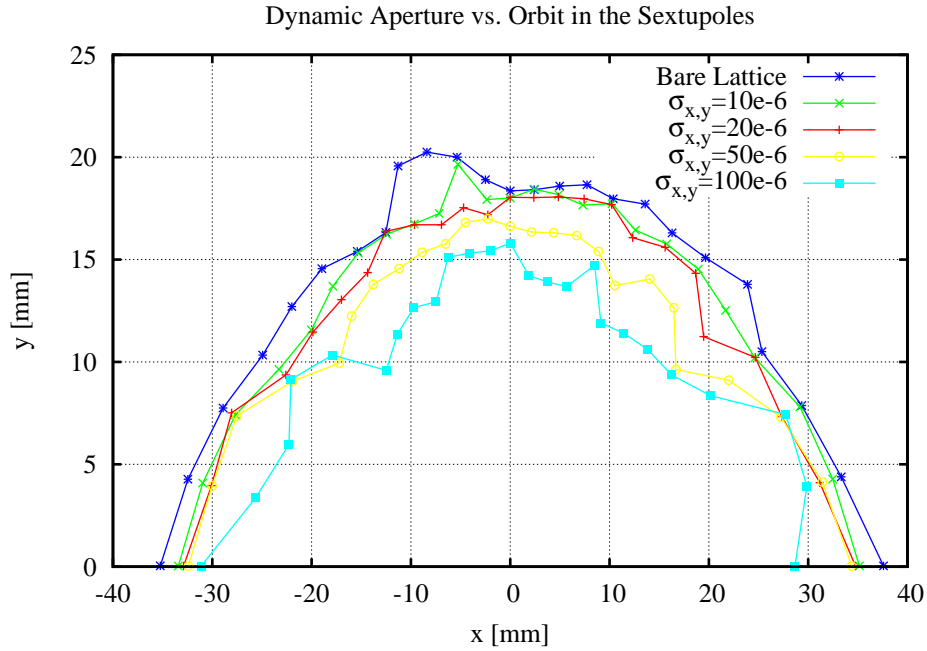
Dynamic Aperture vs. Orbit in the Sextupoles

Figure 6.1.17   DA sensitivity to transverse alignment errors of the sextupoles.

Correspondingly, the required transverse magnet alignment tolerances are summarized in Table 6.1.8, assuming the COD errors are corrected using the seven BPMs and seven correctors of the lattice. Details on the global orbit correction scheme are given in Section 6.1.2.5.

Table 6.1.8   Transverse Magnet Alignment Tolerances.

	Δx RMS [μm]	Δy RMS [μm]	Roll RMS [m-rad]
Dipole	100	100	0.5
Girder	100	100	0.5
Quadrupoles	30	30	0.2
Sextupoles	30	30	0.2

The magnetic field error tolerances are specified in terms of the normal and skew multipole coefficients (b_n, a_n), defined by the normalized transverse magnetic field expansion:

$$\frac{1}{(B\rho)}\left[B_x(x,y) + i\,B_y(x,y)\right] \equiv \sum_n (b_n + i\,a_n)(x + i\,y)^{n-1} = \sum_n (b_n + i\,a_n)\,e^{i(n-1)\varphi} \tag{6.1-13}$$

where $n = 1, 2, 3, \ldots$ are the dipole, quadrupole, sextupole, … components, respectively.

In particular, the multipole errors, $\Delta B_n^{(N)}$, relative to the desired field component, b_N, are normalized at a reference radius R and defined by[10]

$$\Delta B_n^{(N)}(R) \equiv R^{n-N}\,\frac{\Delta b_n}{b_N} \quad or \quad \Delta A_n^{(N)}(R) \equiv R^{n-N}\,\frac{\Delta a_n}{b_N} \tag{6.1-14}$$

---

[10] Using the peak B-field for insertion devices.

where $(\Delta b_n, \Delta a_n)$ are the multipole field errors.

The tolerances for the multipole errors are given in Table 6.1.9 using values achieved at the SLS facility [6.1.21, 6.1.22]. The impact is an additional ~20% DA reduction for the lattice with the previously defined alignment tolerances. Future work will include parametric studies for a more precise specification.

Table 6.1.9   Tolerance Levels for RMS Normalized Multipole Errors.

Magnet Type	Normalized Field Error ($R = 28$ mm)				
Quadrupoles	$\Delta B_2^{(2)}$	$\Delta B_3^{(2)}$	$\Delta A_3^{(2)}$	$\Delta A_3^{(2)}$	$\Delta A_3^{(2)}$
	2.5×10^{-4}	2.8×10^{-4}	2.9×10^{-4}	1.9×10^{-4}	1.4×10^{-4}
Sextupoles	$\Delta B_3^{(3)}$	$\Delta B_4^{(3)}$	$\Delta A_4^{(3)}$	$\Delta B_5^{(3)}$	
	5.0×10^{-4}	5.2×10^{-4}	4.9×10^{-4}	3.5×10^{-4}	

Note: Based on tolerances from SLS.

Similarly challenging is the impact of the linear optics distortions from the insertion devices listed in Table 6.1.10. In particular, the proposed superconducting undulators will substantially affect the nonlinear dynamics in the vertical plane due to their short period (see Section 6.1.2.8). The effect of elliptically polarized undulators on the DA remains to be studied. Table 6.1.11 lists the allowed multipole field tolerances for these undulators [6.1.25]. The potential configuration includes the following IDs:

- CPMUs in the 5 m straights
- CPMUs in the 8 m straights
- DWs in the 8 m straights
- EPUs in the 8 m straights[11]

Details on the impact of these insertion devices and the control of their nonlinear terms are presented in Section 6.1.2.8.

Table 6.1.10   Insertion Device Parameters and Their Impact on the Vertical Tune.

ID	λ_u [mm]	B [T]	K_u	L_u[m]	Gap[mm]	$\Delta\nu_y$
SCU (2+1)	14	1.7	2.2	2	~5	0.002
CPMU (3)	19	1.24	2.2	3	5	0.002
DW	100	1.8	16.8	7	~11	0.028
EPU	~40	0.88	(3.3, 3.3)	~4	~6.5	TBD

Table 6.1.11   RMS Normalized Field Errors for Insertion Devices (CPMU, $R = 20$ mm).

Multipole	$\Delta B_3^{(1)}$	$\Delta A_3^{(1)}$	$\Delta B_4^{(1)}$	$\Delta A_4^{(1)}$
Random	6.6×10^{-7}	6.6×10^{-7}	2.2×10^{-8}	2.2×10^{-8}

Note: Based on tolerances from the Swiss Light Source.

---

[11] Presumably as 2×1 m canted devices; see Table 6.1.14.

6.1.2.5   Control of Closed-Orbit Distortions

While essentially a linear problem, effective orbit control is crucial for robust DA[12] and orbit stability. From a DA point of view, the main objective for the global orbit correction system is to establish and maintain an orbit at the magnetic centers of the sextupoles (to avoid breaking the symmetry of the linear optics), to within ~50 µm (see Table 6.1.7). As a rough guideline, the BPMs should be spaced by ~90º in phase advance and placed close to the sextupoles. With a horizontal DBA cell tune of ~1.1, about six BPMs per cell should provide good coverage. In order to center the orbit in all the BPMs, one corrector for each BPM is needed. In theory, the DA can be restored if the BPM is at the sextupole magnetic center, 0. The number of correctors can be reduced in the vertical plane, since the cell tune is only ~0.5. From the horizontal phase advance (Figure 6.1.18), it is clear that at least one BPM is required in each of the dispersive and straight sections.
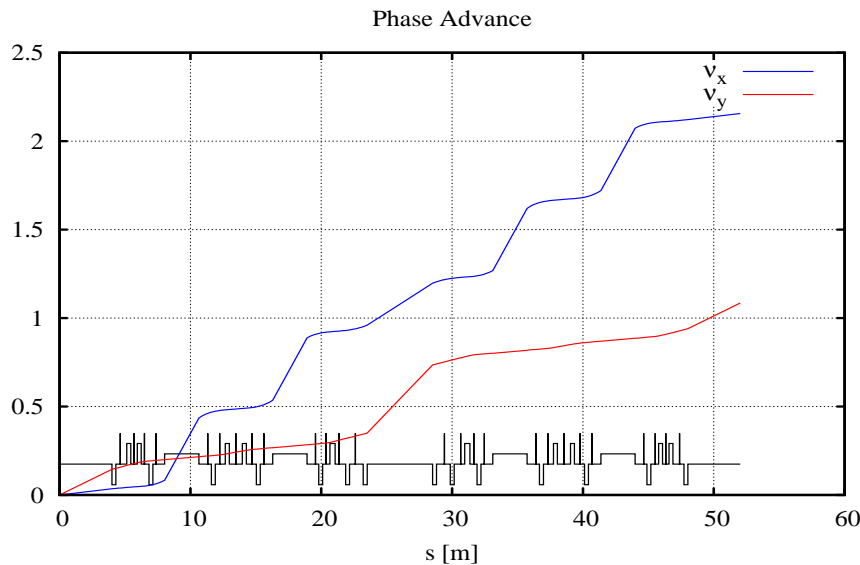
Figure 6.1.18   Normalized Phase Advance for one super-period.

Figures 6.1.19 a and b show the corrected horizontal and vertical RMS closed-orbit distortions (for 1,000 seeds) due to 100 µm RMS random horizontal and vertical quadrupole misalignment errors, with the (H-BPM×H-Corrector, V-BPM×V-Corrector) = (7×7, 7×6) baseline configuration outlined in Section 6.1.1. Clearly, the resulting orbit is well within the guidelines of Table 6.1.7. Note that a BPM is included at the center of each DBA. With some fine tuning of the BPM placement, this BPM can be removed, leading to a (6×6, 6×6) configuration. The BPM buttons will be kept for optics checks during commissioning. Beam-based alignment [6.1.29, 6.1.30] with BPMs at the end of the girders will make it possible to reduce orbit errors below the survey and alignment tolerances for the girders, particularly since the alignment tolerances for the magnetic centers on the girders are tighter than the girder alignment in the tunnel.

---

[12] To avoid the collapse of DA observed in the ALS CDR [6.1.26], eventually addressed by "Global Matching of the Normalized Ring" [7.1.10–7.1.15].
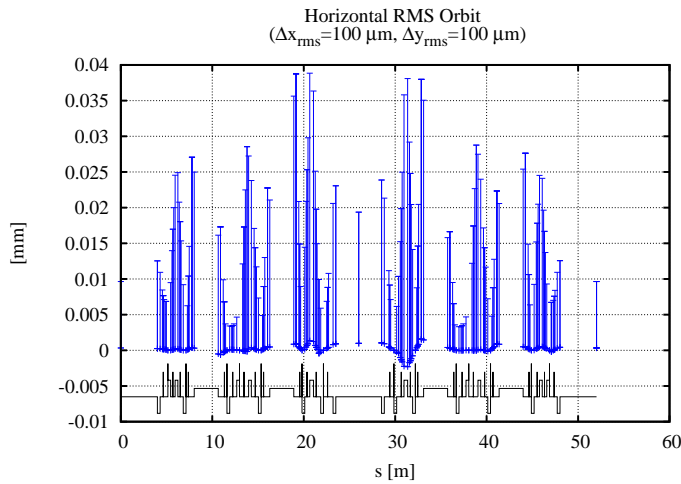
Figure 6.1.19 a Corrected horizontal RMS COD (over 1,000 seeds) for one super-period.
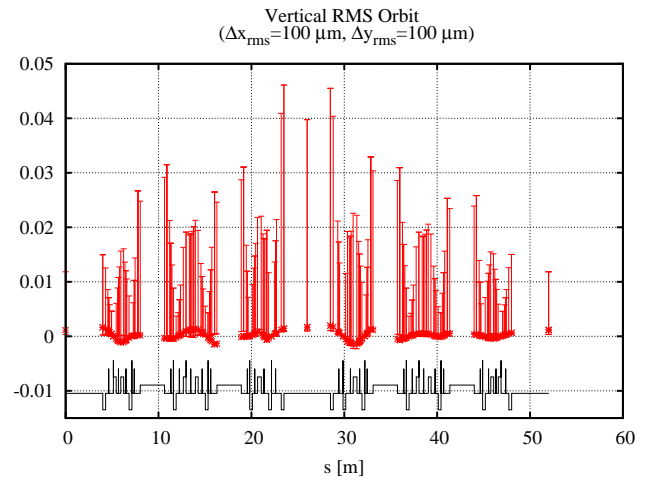
Figure 6.1.19 b Corrected vertical RMS COD (over 1,000 seeds) for one super-period.

Although placing the BPMs close to the sextupoles reduces the residual COD at the sextupoles, the BBA resolution is better for quadrupole centering (<10 µm both H and V) by at least a factor of three [6.1.28]. This allows for orbit centering beyond the magnet alignment tolerance on the girder. Therefore, we have adopted the (7×7, 7×6) correction scheme, with the BPMs close to the quadrupoles for BBA with a resolution of 10 µm. The impact on the DA of the corrected COD resulting from the alignment tolerances[13] listed in Table 6.1.8 is shown in Figure 6.1.20 (for 10 random seeds). Clearly the (7×7, 7×6) orbit correction system provides adequate DA, and provides margin for error.
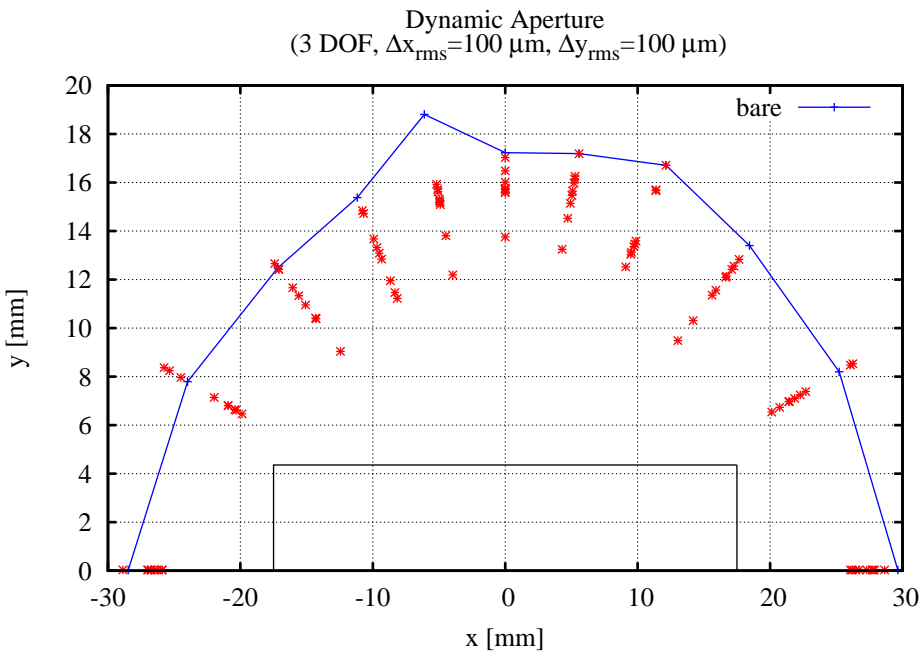

Figure 6.1.20 DA for lattice with transverse misalignment errors, according to Table 6.1.8. These CODs are corrected with the baseline (7×7, 7×6) system.

---

[13] Except for roll errors, to be treated later.

6.1.2.6   Control of Vertical Beamsize

The vertical beamsize is given by

$$\sigma_y = \sqrt{\beta_y \varepsilon_y + \left(\eta_y \sigma_\delta\right)^2} \tag{6.1-15}$$

where β_y and η_y are the vertical beta function and dispersion, ε_y is the vertical emittance, and σ_δ is the momentum spread. The design goal is $\varepsilon_y \sim 0.01$ nm-rad, corresponding to $\sigma_y \sim 5$ μm in the short straights. The non-vanishing vertical emittance originates from:

- linear coupling of the horizontal emittance due to roll errors of the quadrupoles and vertical orbit displacement in the sextupoles,
- and vertical dispersion due to roll errors of the dipoles and linear coupling of the horizontal dispersion.

Local control of the vertical beamsize is straightforward. In particular, by controlling the off-diagonal beam response matrix elements given by [6.1.29]:

$$\frac{\partial y_k}{\partial p_{x,i}} = -\frac{(\Delta a_2 L)_j \sqrt{\beta_{x,i}\beta_{x,j}\beta_{y,j}\beta_{x,k}}\cos\left(\left|\mu_{x,i\to j}\right| - \pi\nu_x\right)\cos\left(\left|\mu_{y,j\to k}\right| - \pi\nu_y\right)}{4\sin(\pi\nu_x)\sin(\pi\nu_y)} + O(\Delta a_2 L)^2,$$

$$\frac{\partial x_k}{\partial p_{y,i}} = -\frac{(\Delta a_2 L)_j \sqrt{\beta_{y,i}\beta_{y,j}\beta_{x,j}\beta_{y,k}}\cos\left(\left|\mu_{y,i\to j}\right| - \pi\nu_y\right)\cos\left(\left|\mu_{x,j\to k}\right| - \pi\nu_x\right)}{4\sin(\pi\nu_x)\sin(\pi\nu_y)} + O(\Delta a_2 L)^2 \tag{6.1-16}$$

for a dipole kick, $p_{(x,y)i}$ at i, due to a skew quadrupole $(a_2 L)$ at j. produces an orbit change $(\Delta x_k, \Delta y_k)$ at a BPM located at k. Similarly, the local control of the vertical dispersion is done by:

$$\Delta\eta_{y,k} = -\frac{(\Delta a_2 L)_j \eta_{x,j}\sqrt{\beta_{y,j}\beta_{x,k}}\cos\left(\left|\mu_{x,j\to k}\right| - \pi\nu_x\right)}{2\sin(\pi\nu_y)} + O(\Delta a_2 L)^2 \tag{6.1-17}$$

The driving term for the linear coupling is shown in Figure 6.1.21, whereas the driving term for vertical dispersion is similar to the one for vertical linear chromaticity, (see Figure 6.1.7). We have found that adequate control is obtained by introducing one skew quadrupole:

- in each long matching section
- in one of the dispersion cells for each super-period

for a total of $15 + 15 = 30$ skew quadrupoles for the full lattice. The corresponding (linear) $82,110 \times 30$ system of equations

$$\left[\frac{\partial \overline{x}}{\partial \overline{p}_y}, \frac{\partial \overline{y}}{\partial \overline{p}_x}, \Delta \overline{\eta}_y\right]^T = S \cdot \overline{(\Delta a_2 L)} \tag{6.1-18}$$

was solved in a least-square sense by the Singular Value Decomposition method. The vertical dispersion after correction for the coupling introduced by the roll errors in Table 6.1.8, is shown in Figure 6.1.22. It turns out that the vertical emittance can be corrected significantly below $\varepsilon_y \sim 0.01$ nm-rad. To optimize the Touschek

lifetime, a vertical dispersion wave[14] is introduced to obtain the desired vertical beamsize, e.g., η_y = 5 mm => $\sigma_y \sim \eta_y \sigma_\delta = 5$ μm (see Figure 6.1.23). Since it is straightforward to measure the beam response matrix and vertical dispersion on the real storage ring, the correction algorithm implemented for this simulation will eventually be used for commissioning as well.
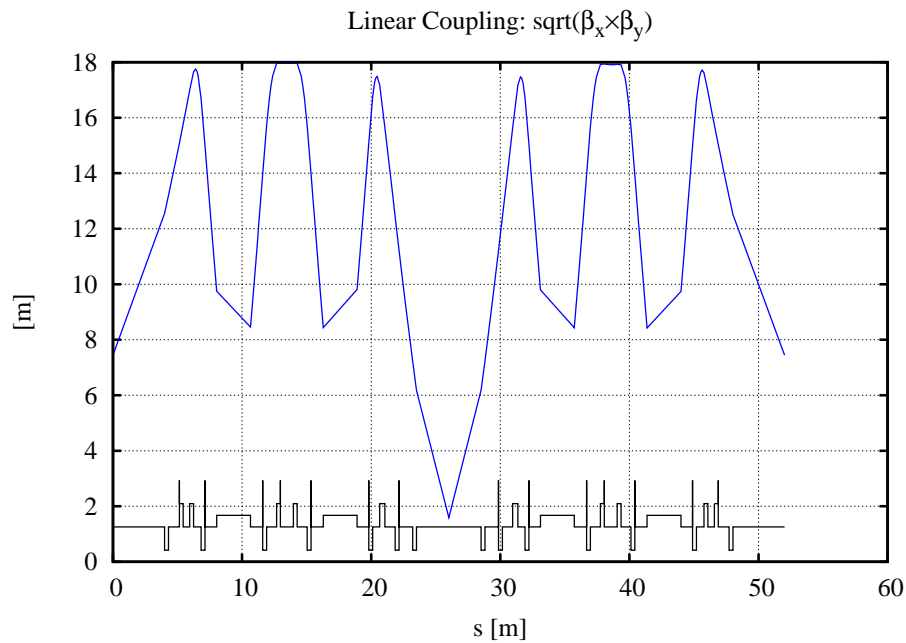
Linear Coupling: sqrt($\beta_x \times \beta_y$)

Figure 6.1.21 Driving term for linear coupling, for one super-period.

Vertical Dispersion
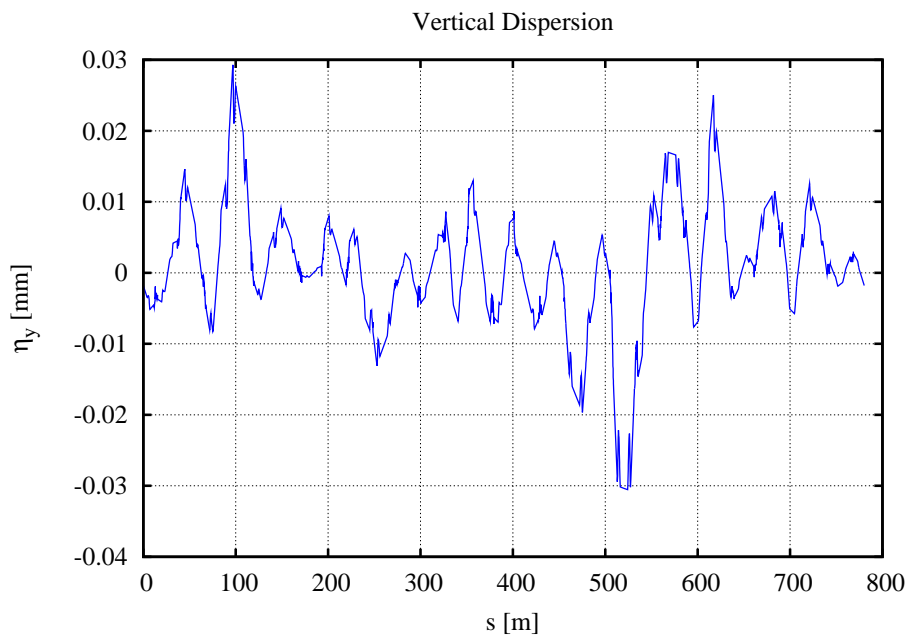
Figure 6.1.22 Corrected vertical dispersion for the quadrupole and dipole roll tolerances.
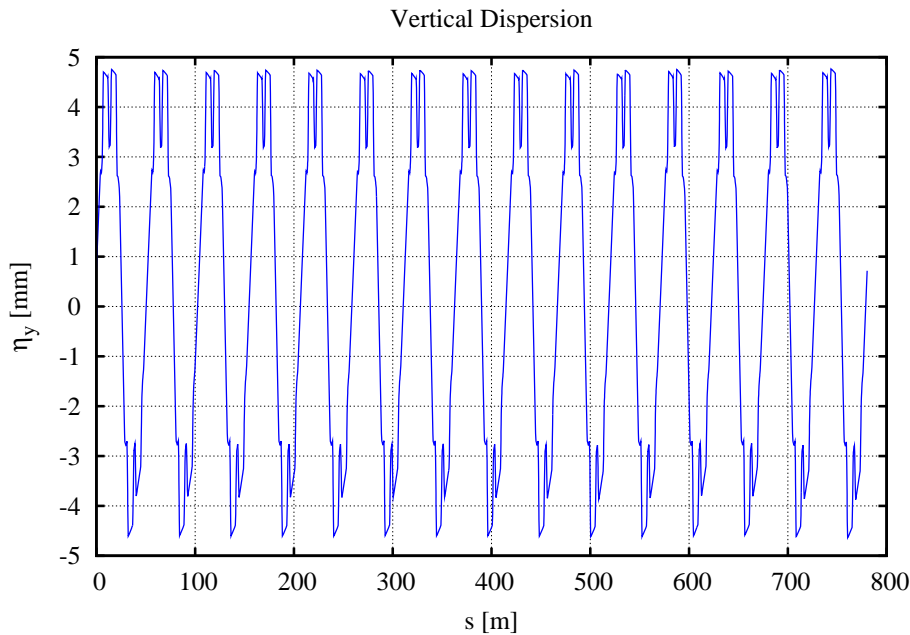
---

[14] To avoid affecting the dynamics 0.

Figure 6.1.23 Corrected vertical dispersion with a residual 5 mm dispersion wave for vertical beamsize control.

6.1.2.7   Robustness of DA

The introduction of alignment errors in the lattice leads to orbit distortions, which generate magnetic field errors due to feed-down in the multipoles. These errors are summarized in Table 6.1.12. A robust DA requires that the global orbit correction system maintains the orbit centered in the sextupoles, since feed-down leads to gradient errors. To correctly evaluate this impact, correlations between magnet-magnet alignment errors, e.g., from girder misalignments, need to be included. Also, real magnets are not pure dipoles, quadrupoles, or sextupoles, requiring systematic and random multipole errors to be included. A detailed study of the individual maximum tolerance levels of these multipole errors remains to be done, but the realistic values listed in Table 6.1.9 have been used to evaluate the impact on the DA.

Table 6.1.12   Effect of Mechanical Tolerances on the Magnetic Field Quality.

	Dipole	Quadrupole	Sextupole
Horizontal orbit		horizontal dipole error	gradient error
Vertical orbit		vertical dipole error	skew quadrupole error
Roll error	vertical dipole error	skew quadrupole error	skew sextupole error

Also, due to the nonlinear chromaticity, tracking for at least one synchrotron oscillation period is required to obtain realistic estimates of the DA, since the off-momentum particle will be slowly crossing betatron resonances, which may limit the stability to smaller amplitudes. The design goal for the RF acceptance is ±3%. To obtain a conservative estimate of the momentum aperture, an RF voltage sufficient to produce a 4% bucket height was used to evaluate the DA. The impact on the DA and momentum aperture is shown in Figures 6.1.24 – 6.1.26, where the black-outlined rectangle (Figure 6.1.24) represents the physical aperture of the lattice, propagated to the center of the long straight section. The 10 seeds shown represent 10 lattices generated with randomly distributed alignment and multipole errors having RMS values given by the tolerance values and corrected for COD, as described above. The tracked particles undergo synchrotron

oscillations, but do not radiate. Since the radiation damping will also lead to the crossing of resonances, it should also be included in refined studies.

Low-emittance lattices tend to have a small linear momentum compaction, α_1, requiring the second-order term, α_2, to be included for a proper evaluation of the RF bucket, which becomes distorted and reduces the momentum acceptance [6.1.31]. The source of this distortion is a second stable fixed point, which has an energy offset given by the ratio:

$$\alpha_1/\alpha_2 \approx 3.7 \times 10^{-4} / 4.1 \times 10^{-4} = 92\% .$$

(6.1-19)

Since it only becomes important for ratios <20%, it will not pose a problem for this lattice[15]. This is further demonstrated by the phase space for the longitudinal Hamiltonian (shown in Figure 6.1.27), including terms to α_3, as well as the radiation loss of 35 m of damping wigglers.

To summarize, the DA guidelines from Table 6.1.5 are easily met for the bare lattice, as well as when the impact of realistic alignment and field tolerances, listed in Tables 6.1.8 and 6.1.9, are included in the lattice model using the correction schemes described above.
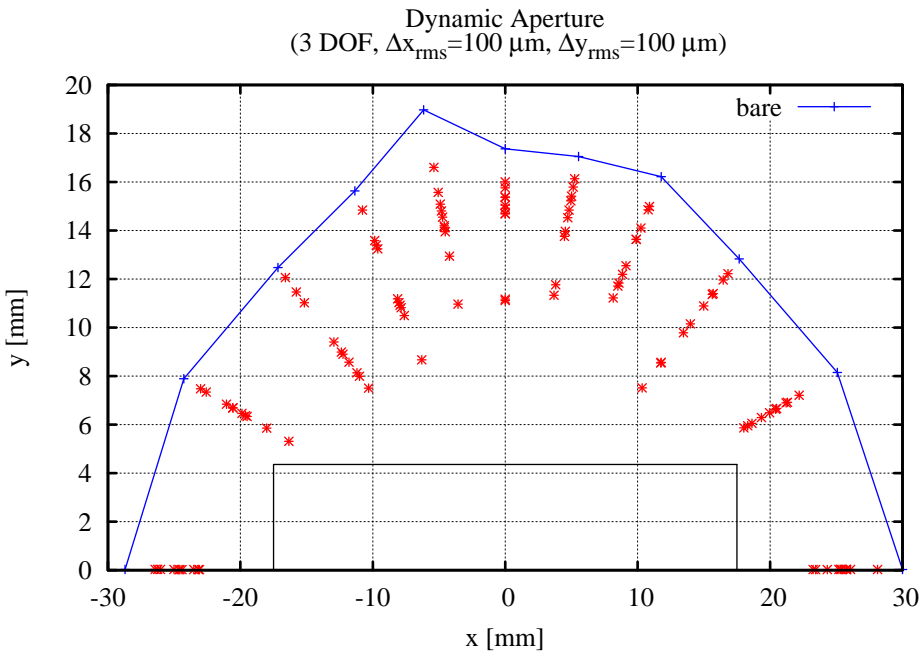

Figure 6.1.24 DA for a "realistic" lattice (10 seeds) with engineering tolerances and corrections. The black outline indicates the physical aperture.

---

[15] An advantage of the achromatic straights for the DBA lattice.

Horizontal Momentum Aperture
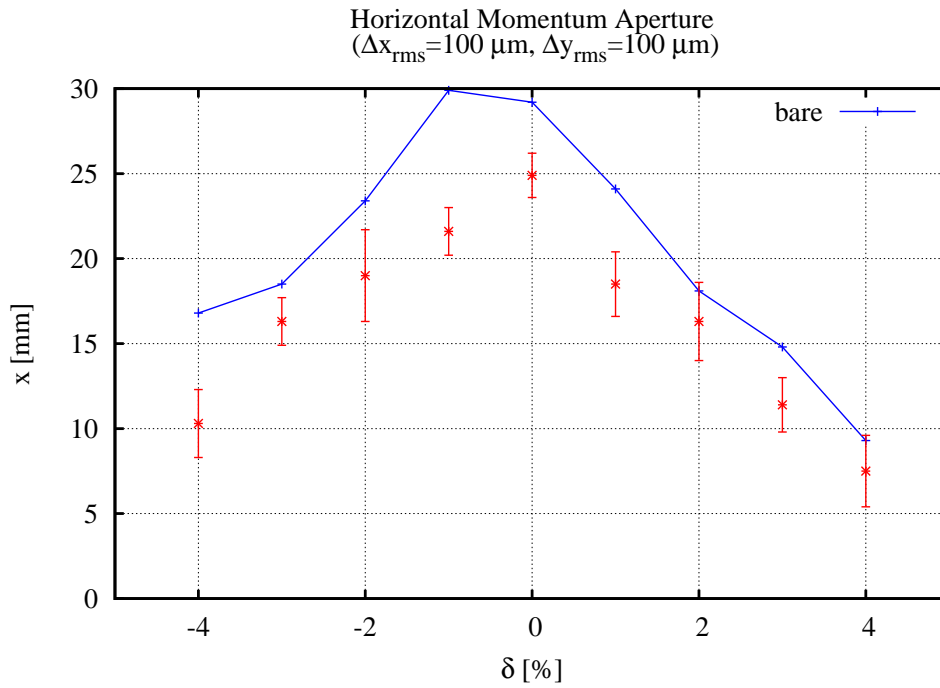$(\Delta x_{rms}=100\ \mu m,\ \Delta y_{rms}=100\ \mu m)$

Figure 6.1.25
Average and RMS horizontal momentum aperture for a "realistic" lattice (10 seeds) with engineering tolerances and corrections.
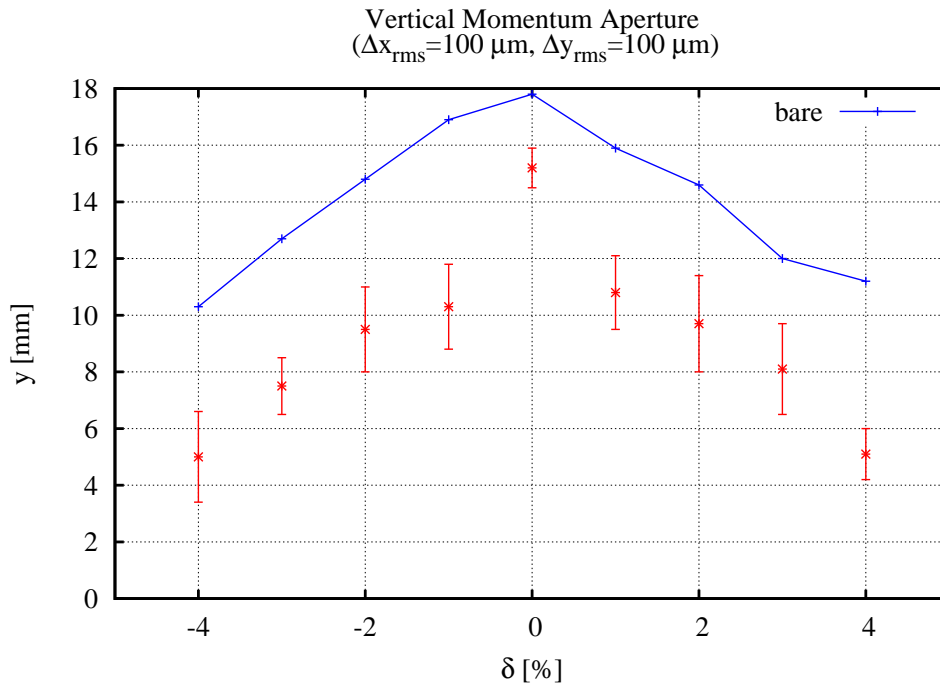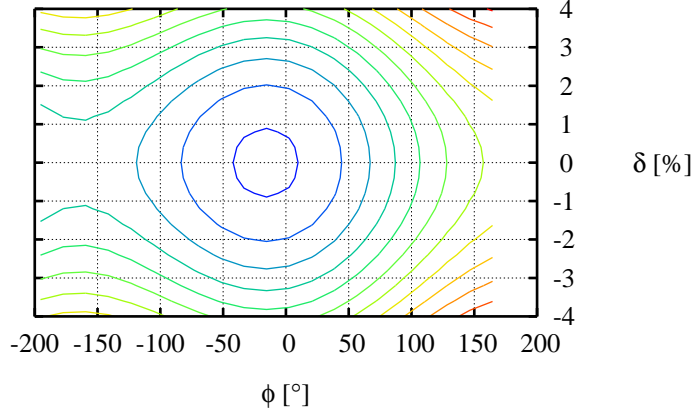
Vertical Momentum Aperture
$(\Delta x_{rms}=100\ \mu m,\ \Delta y_{rms}=100\ \mu m)$

Figure 6.1.26
Average and RMS vertical momentum aperture for a "realistic" lattice (10 seeds) with engineering tolerances and corrections.

Longitudinal Phase Space to $O(\alpha_4)$

Figure 6.1.27   Longitudinal phase-space, including the radiation loss from damping wigglers.

6.1.2.8   Control of Impact from Insertion Devices

The Hamiltonian for an ID averaged over one undulator period, λ_u, is given by [6.1.32, 6.1.33]:

$$\langle H \rangle_{\lambda_u} \approx \frac{p_x^2 + p_y^2}{2(1+\delta)} - \frac{B_u^2 y^2}{4(B\rho)^2 (1+\delta)} + \frac{\pi^2 B_u^2 y^4}{3(B\rho)^2 \lambda_u^2 (1+\delta)} - \delta + O\left(p_{x,y}^4\right) \tag{6.1-20}$$

with phase-space coordinates $\vec{x} = \left[x, p_x, y, p_y, \delta, c\Delta t\right]$, peak field B_u, and magnetic rigidity $(B\rho)$[16]. Note that both the leading-order linear and nonlinear effect scales with $1/(B\rho)^2$, i.e., the effect is reduced with the energy squared for a given undulator field, B_u. The term quadratic in y introduces a vertically focusing term with the integrated gradient

$$(b_2 L) \approx -\frac{B_u^2 L_u}{2(B\rho)^2} \tag{6.1-21}$$

i.e., quadratic in B_u. The beta-beat at location i due to integrated quadrupole kicks, $(\Delta b_2 L)_j$, is given by:

$$\frac{\Delta \beta_{(x,y),i}}{\beta_{(x,y),i}} = \sum_{j=1}^{N} \frac{(\Delta b_2 L)_j \beta_{(x,y),j} \cos\left(\left|2\mu_{(x,y),i \to j}\right| - 2\pi\nu_{(x,y)}\right)}{2\sin\left(2\pi\nu_{(x,y)}\right)} + O(\Delta b_2 L)^2 \tag{6.1-22}$$

where β, μ, ν are the beta functions, phase advance, and tune. Similarly, the phase-beat is given by:

$$\Delta \mu_{(x,y),i} = -\sum_{j=1}^{N} \frac{\text{sgn}\left(\mu_{(x,y),i \to j}\right)(\Delta b_2 L)_j \beta_{(x,y),j}\left(\sin\left(2\pi\nu_{(x,y)}\right) + \sin\left(\left|2\mu_{(x,y),i \to j}\right| - 2\pi\nu_{(x,y)}\right)\right)}{4\sin\left(2\pi\nu_{(x,y)}\right)} + O(\Delta b_2 L)^2 \tag{6.1-23}$$

---

[16] $(B\rho) \approx 10.007$ T-m at 3 GeV.

and the total tune shift is given by

$$\Delta v_{(x,y)} = \pm \frac{1}{4\pi} \sum_{j=1}^{N} (\Delta b_2 L)_j \, \beta_{(x,y),j} + O(\Delta b_2 L)^2 \tag{6.1-24}$$

The parameters for the proposed insertion devices are summarized in Table 6.1.10 and the impact of three DWs on the linear optics is shown in Figure 6.1.28, where the beta-beat is rather obvious.
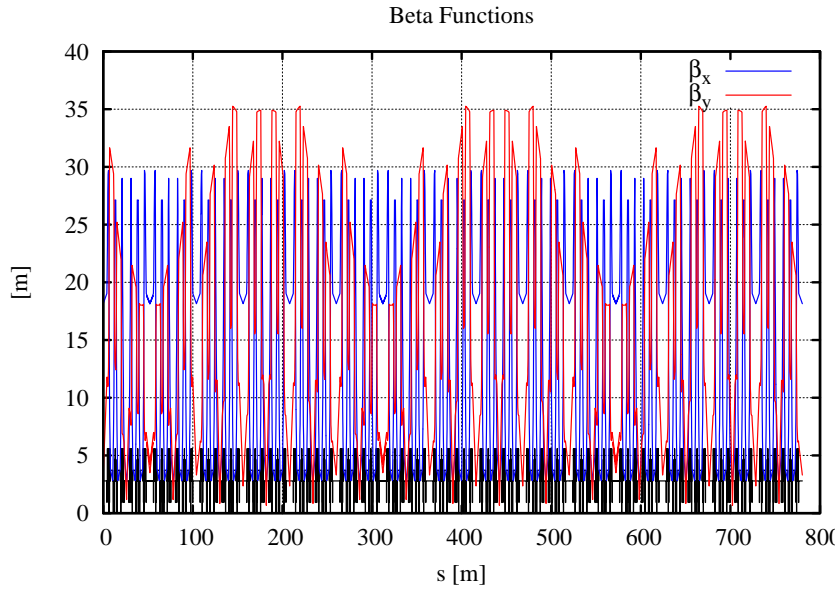

Figure 6.1.28   Perturbed beta functions of the lattice with three DWs installed.

The perturbation of the optics is corrected by adjusting the quadrupole quadruplets in the matching sections. With four quadrupole strengths as parameters, it is expected[17] that the beta- and phase advance beat can be removed in both planes. In particular, the optics deviations at all of the lattice sextupoles, *i,* are represented in a linearized system of equations that includes the focusing impact of all installed IDs *(Δb₂L)ⱼ*. These equations are given in matrix form by

$$\left[\left(\frac{\Delta \beta_{(x,y)}}{\beta_{(x,y)}} \right)_i , \Delta \mu_{(x,y),i} , \Delta v_{x,y} \right]^{\mathrm{T}} = A \cdot \left[\Delta \bar{b}_2 \, L \right] \tag{6.1-22}$$

which was solved using an iterated SVD algorithm[6.1.34, 6.1.35], see Figure 6.1.29. The corrected beta and phase advance beats satisfy the optics tolerances specified in Table 6.1.7.

---

[17] If the parameters are independent.
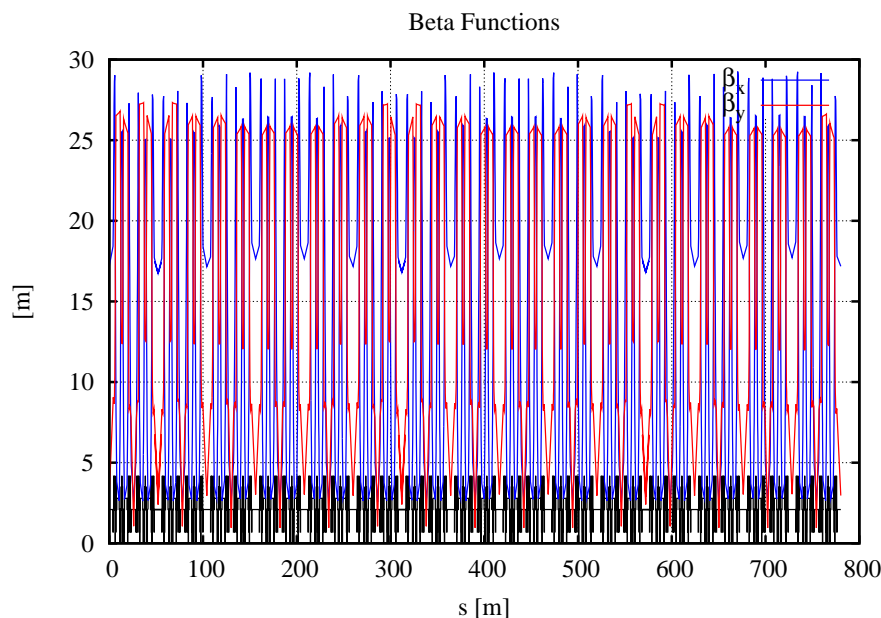
Beta Functions

Figure 6.1.29 Corrected beta functions for the lattice with three DWs installed.

The leading order nonlinear part of the ID focusing contains an octupole-like term in the vertical plane which drives amplitude dependent vertical tune shift and $2\nu_y$ and $4\nu_y$ resonances. Table 6.1.13 presents a comparison of the magnitude of the main driving terms from the IDs with those from sextupoles in the lattice.

Table 6.1.13   Lie Generators from the Sextupole Scheme and a Single ID.

Lie Generator	Effect	Sextupole Scheme	DW (Long Straight)	CPMU (Short Straight)	CPMU (Long Straight)	SCU (Short Straight)	SCW (Short Straight)	EPU
h00220	$\partial\nu_y/\partial J_y$	606.9	1,089.2	1,102.6	3,681.3	1,259.6	TBD	TBD
h00310	$2\nu_y$	76.2	52.3	6.9	379.1	39.5		
h00400	$4\nu_y$	46.6	58.7	13.7	228.3	11.3		

The effect on the DA of a lattice with corrected magnet misalignment errors and one ID (one at a time for the DW, CPMU, and SCU IDs) is shown in Figure 6.1.30. While there is a substantial reduction of the vertical DA when one CPMU or SCU is introduced, nevertheless the DA remains outside the physical aperture and it does not degrade significantly as additional devices are included (Figure 6.1.31).

Although the long straight sections are primarily planned for machine components and DWs, there will be four uncommitted long straights. The high power radiated by a 7 m DW raises the question of the feasibility of splitting the wiggler into sections, which could be canted, yielding multiple lower-power beamlines from one long ID. Also, the potential of inserting multiple short undulators with canting in the long IDs is being considered as a method for obtaining more than four beamlines from the uncommitted long straight sections. In principle, one can introduce a small angular separation of the photon beams with three or four corrector magnets that bend the electron beam in the straight section by an angle θ, with little perceived impact. However, this adds horizontal dispersion to the achromatic straight section, which reduces the effectiveness of the DW in lowering emittance.
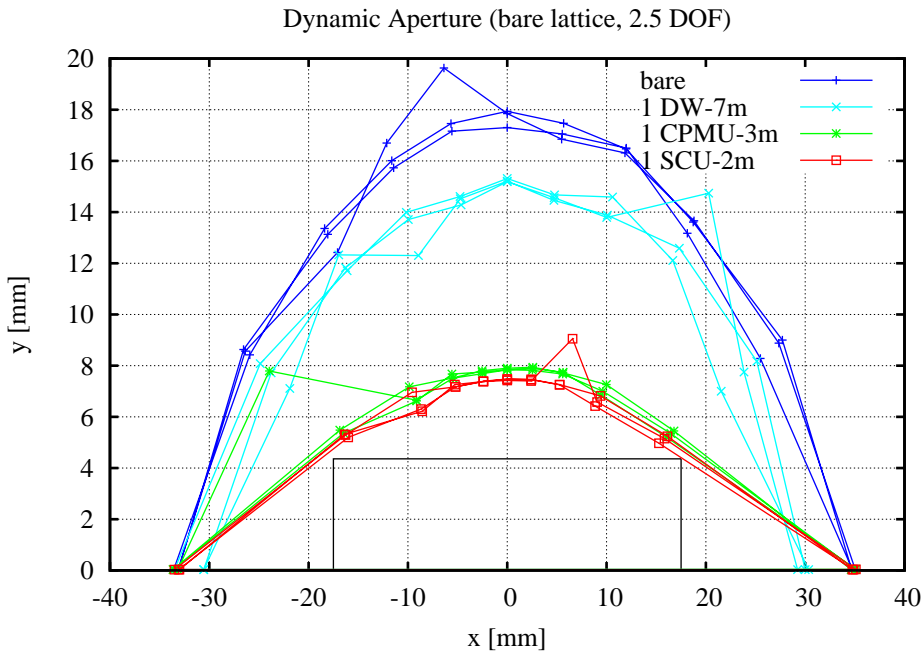
Figure 6.1.30 DA for the lattice with transverse alignment errors (for three seeds) and a single ID, one type at a time, for DWs, CPMUs, or SCUs.
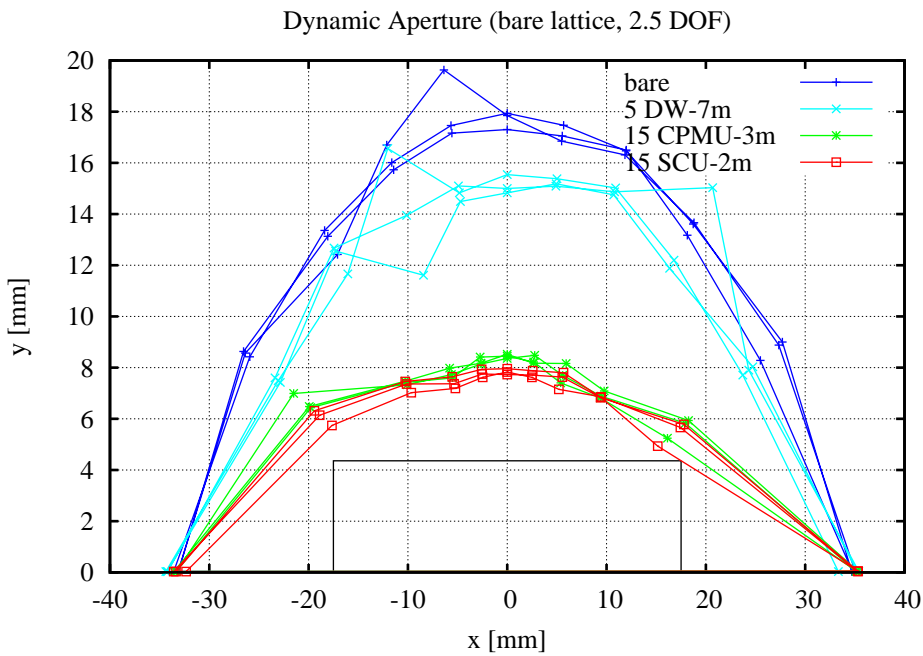

Figure 6.1.31 DA for the lattice with transverse alignment errors (for three seeds) and multiple IDs, one type at a time for five DWs, 15 CPMUs, or 15 SCUs.

A preliminary evaluation of the feasibility of canting of the IDs to yield either two or three separated photon beams per straight section is summarized in Table 6.1.14. We have found that a two-way canting angle of ≤3 mrad contributes with a few mm of horizontal dispersion and increases the emittance by less than 10%. For a three-way canting angle of 3 mrad, the emittance increase is >20%. For the undulators, this impact is considerably less, since they only provide a small amount of damping. These results were obtained with corrected optics using the four quadrupoles in matching sections.

Table 6.1.14 Emittance Increase Due to Canting of the DW and the CPMU Undulator.

Configuration	Cant Angle $(\theta/2, -\theta, \theta/2)$ [m-rad]	Cant Angle $(\theta, -\theta, -\theta, \theta)$ [m-rad]	Peak η_x [mm]	σ_δ [%]	ε_x [nm]
Bare Lattice				0.051	2.04
5×7 = 35 m DWs				0.090	0.66
5×(2×3.5) = 35 m DWs	1.5, -3, 1.5		6	0.090	0.71
	2.5, -5, 2.5		10	0.090	0.80
5×(3×2.33) = 35 m DWs		1, -1, -1, 1	3	0.089	0.67
		3, -3, -3, 3	8	0.089	0.80
35 m DWs + 1×2 = 2 m CPMU				0.089	0.64
35 m DWs + 1×(2×1) = 2 m CPMU	1, -2, 1		3	0.089	0.64
8×7 = 56 m DWs				0.094	0.48
8×(2×3.5) = 56 m DWs	1.5, -3, 1.5		6	0.094	0.54

6.1.2.9 Future Work in Lattice and Beam Dynamics Issues

The work presented here shows that the present lattice is very robust for the errors and realistic magnets and IDs studied to this point. Additional work is needed to evaluate 1) the implications of going to higher energy, 2) tailoring by, and refocusing for, multiple IDs per straight, and 3) corrections for longer IDs. This involves the following tasks.

- scan the individual field tolerances for maximum allowable values
- study the impact of multipole errors in the IDs
- evaluate the DA for the complete set of alignment and field errors with a full complement of IDs and corrections
- Move the working point to avoid crossing of the horizontal and vertical tune off-momentum, to avoid a reduction of Touschek lifetime when roll errors are introduced. Changing the sextupole values has already shown promise in avoiding this tune-crossing by reducing the second-order chromaticity.
- evaluate the acceptable range of positive linear chromaticity for head–tail stabilization
- reduce the nonlinear chromaticity by controlling second-order horizontal dispersion in the linear optics design
- evaluate the impact of a reduced number of BPMs and correctors
- evaluate the impact of removing one quadrupole family in the short matching sections
- evaluate the impact of removing 1+1 sextupole families in the short and long matching sections
- evaluate the impact of elliptically polarizing undulators and provide guidelines for their integration into the lattice
- evaluate the Touschek life time for a realistic lattice, i.e., with vertical apertures, misalignments and field errors, insertion devices, and related corrections
- evaluate the phase-space dynamics with radiation damping (one damping time) for a realistic lattice
- study the injection dynamics of the stored beam bump and the injected beam pulse
- evaluate the feasibility of reducing the amplitude-dependent tune shifts from the IDs, by introducing octupoles

References

[6.1.1]   H. Weidemann, NIM **A266**, p. 24 (1988).

[6.1.2]   S. Krinsky, et. al., EPAC06, p.3487 (2006).

[6.1.3]   G. Decker, and O. Singh, *Phys. Rev. STAB* **2,** p. 112801 (1999).

[6.1.4]   S. Krinsky, J. Bengtsson, and S. Kramer, "Consideration of a Double Bend Achromatic Lattice for NSLS-II," pp. 3487–3489, EPAC06.

[6.1.5]   J. Bengtsson, "A Control Theory Approach for Dynamic Aperture," pp. 3478–3480, EPAC06.

[6.1.6]   J. Bengtsson, W. Joho, P. Marchand, G. Mülhaupt, L. Rivkin, and A. Streun, "Increasing the Energy Acceptance of High Brightness Synchrotron Light Storage Rings," *Nucl. Instr. Meth. A* **404**, 237–247 (1998).

[6.1.7]   A. Wrulich, et al., "Commissioning of the Swiss Light Source," pp. 224–226, PAC01.

[6.1.8]   A. Wrulich, et al., "Achievements of the SLS Commissioning," PSI. Scientific Report 2001 Vol. VII, 2002.

[6.1.9]   M. Böge, "Achieving Sub-Micron Stability in Light Sources," pp. 211–213, EPAC04.

[6.1.10]   J. Bengtsson, and E. Forest, "Global Matching of the Normalized Ring" Workshop on Effects of Errors in Accelerators, their Diagnosis and Corrections," Corpus Christi, TX, Oct. 3–8, 1991.

[6.1.11]   J. Bengtsson, and M. Meddahi, "Modeling of Beam Dynamics and Comparison with Measurements for the Advanced Light Source (ALS)," pp. 1022–1024, EPAC94.

[6.1.12]   D. Robin, G. Portmann, H. Nishimura, and J. Safranek, "Model Calibration and Symmetry Restoration of the Advanced Light Source," pp. 971–973, EPAC96.

[6.1.13]   J. Safranek, "Experimental Determination of Storage Ring Optics Using Orbit Response Measurements," *Nucl. Instr. and Meth. A* **388**, 27-36 (1997).

[6.1.14]   D. Robin, C. Steier, J. Safranek, and W. Decking, "Enhanced Performance of the Advanced Light Source through Periodicity Restoration of the Linear Lattice," pp. 136–138, EPAC00.

[6.1.15]   J. Laskar, L. Nadolski, D. Robin, and C. Steier, "Global Dynamics of the Advanced Light Source Revealed through Experimental Frequency Map Analysis," *Phys. Rev. Lett.* **85**, 558–561 (2000).

[6.1.16]   J. Bengtsson, "X-Ray Ring Optics: the Inverse Problem," NSLS Tech Note 540 (2005).

[6.1.17]   J. Bengtsson, "The Sextupole Scheme for the Swiss Light Source (SLS): An Analytic Approach," SLS Note 9/97 (1997).

[6.1.18]   Diamond Synchrotron Light Source: Report of the Design Specification," CCLRC (2002).

[6.1.19]   S.L. Kramer, S. Krinsky, and J. Bengtsson, "Comparison of Double Bend and Triple Bend Achromatic Lattice Structures for NSLS-II," pp. 384–386, EPAC06.

[6.1.20]   J. Bengtsson, "On the NSLS-II Dynamic Aperture: Robustness," NSLS-II Tech Note 8 (2005).

[6.1.21]   A. Streun, "SLS Dynamic Acceptance Degradation due to Magnet Multipole Errors," SLS-TME-TA-1998-0002 (1998).

[6.1.22]   E.I. Antokhin, et al., "Multipoles of the SLS Storage Ring: Manufacturing and Magnetic Measurements," IEEE Trans. of Appl. Super. vol. 12, no. 1, 51–54 (2002).

[6.1.23]   J. Safranek, C. Limborg, A. Terebilo, K.I. Blomqvist, P. Elleaume, and Y. Nosochkov, "Nonlinear Dynamics in a SPEAR Wiggler," *Phys. Rev. ST* **5,** 010701 (2002).

[6.1.24]   C. Steier, G. Portmann, and A. Young, "Commissioning of the First Elliptically Polarizing Undulator at the ALS," pp. 2343–2345, EPAC00.

[6.1.25]   B. Singh, and A. Streun, "Limits for Normal and Skew Sextupole and Octupole Field Errors in the First (I_1) and Second (I_2) Field-Integrals of Insertion Devices planned for SLS," SLS-TME-TA-2001-0170 (2001).

[6.1.26]   "1-2 GeV Synchrotron Radiation Source Conceptual Design Report," LBNL PUB-5172 (1986).

[6.1.27]   G. Portmann, D. Robin, and L. Schachinger, "Automated Beam Based Alignment of the ALS Quadrupoles," pp. 2693–2695, EPAC96.

[6.1.28]   S.L. Kramer, "Beam Based Alignment," NSLS-II Tech Note (2006).

[6.1.29]   J. Bengtsson, and I. Pinayev, "NSLS-II: Control of Vertical Emittance," NSLS-II Tech Note (2006).

[6.1.30]   C. Steier, D. Robin, A. Wolski, G. Portmann, and J. Safranek, "Coupling Correction and Beam Dynamics at Ultralow Vertical Emittance in the ALS," pp. 3213–3215, PAC03.

[6.1.31]   D. Robin, E. Forest, C. Pellegrini, and A. Amiry, "Quasi-Isochronous Storage Rings," *Phys. Rev. E* **48**, 2149–2156 (1993).

[6.1.32]   L. Smith, "Effect of Wigglers and Undulators on Beam Dynamics," LBL-21391 (1986).

[6.1.33]   Y. Wu, V.N. Litvinenko, and J.M.J. Madey, "Lattice and Dynamic Aperture of the Duke FEL Storage Ring," pp. 218–220, PAC93.

[6.1.34]   T. Shaftan and J. Bengtsson, "Impact of Insertion Devices on the NSLS-II lattice," NSLS-II Tech. Note (2006).

[6.1.35]   T. Shaftan, J. Bengtsson, and S. Kramer, "Control of Dynamic Aperture with Insertion Devices," pp. 3490–3492, EPAC06.

6.2   Collective Effects

6.2.1   Introduction

In this section, we discuss the effect of multi-particle interactions [6.2.1] on the electron beam in the NSLS-II storage ring. The storage ring has 500 MHz RF and a revolution period of 2.6 μs. The baseline design configuration corresponds to filling 80% of the RF buckets and leaving a 20% gap to allow for ion clearing. In this case we have M = 1040 bunches, each containing $N_e = 7.8 \times 10^9$ electrons ($N_e e$ = 1.25 nC) corresponding to a total average current $I_{av} = M N_e e / T_0$ = 500 mA and a single-bunch current $I_0 = N_e e / T_0$ = 0.5 mA. For an RMS bunch duration σ_t = 15 ps, the peak bunch current is $I_p = N_e e / \sqrt{2\pi}\sigma_t$ = 33 A.

Limitations on the single bunch current result from the short-range wakefield (broadband impedance). The longitudinal microwave instability depends primarily on the impedance of the vacuum vessel. The transverse mode coupling instability depends on the resistive wall impedance and the geometric impedance due to changes in the vacuum chamber cross-section.

Limitations on the total average current arise from the long-range wakefield (narrowband impedance). The longitudinal coupled-bunch instability is predominantly driven by the longitudinal higher-order modes in the RF cavity. The transverse coupled-bunch instability is primarily due to the resistive wall and the transverse higher-order modes in the RF cavity.

The most accurate approach to estimating the instability thresholds for NSLS-II is to carry out computer simulation tracking studies using the wakefields determined by numerical calculations of the wakefield for each component comprising the storage ring. This is a large effort that is now underway. Here, we shall provide estimates of the instability thresholds using a simplified model of the ring impedance, which has been developed based on impedance calculations performed to-date and on the experience at existing storage rings [6.2.2], especially APS and ESRF. We also present results of impedance calculations obtained thus far using the electromagnetic simulation code GdfidL [6.2.3].

In addition to the wakefield effects mentioned above, we also discuss intrabeam scattering. We report estimates of the Touschek lifetime resulting from single scattering, and of the increase in emittance due to multiple scattering.

We plan to use third-harmonic Landau cavities to increase the bunch length and synchrotron tune spread. Lengthening the bunch will be useful in raising the longitudinal microwave instability threshold, increasing the Touschek lifetime and reducing the effect of intrabeam scattering on the emittance. Increasing the bunch length and synchrotron tune spread improves the effectiveness of positive chromaticity in raising the single and coupled bunch transverse instability thresholds. The beam dynamics issues involved in the operation of the Landau cavities will be addressed.

6.2.2   Wakefields and Impedance

We provide a short overview of wakefields and impedance [6.2.4, 6.2.5] to clarify the approach we plan to adopt. Consider a point charge q (the drive particle) traveling very close to the speed of light in the z-direction through a vacuum enclosure displaced from the design trajectory by $\vec{r}_d$. A unit test charge travels at a distance s behind the first (see Figure 6.2.1) on a trajectory parallel to the z-axis but displaced by $\vec{r}_t = (x, y)$. The change of momentum $\Delta\vec{p}$ of the second particle, caused by the electromagnetic field of the first, is given by

$$\Delta\vec{p} = \int_{-\infty}^{\infty} dt \left[\vec{E}\left(\vec{r}_t, z, t \right) + c\,\hat{z} \times \vec{B}\left(\vec{r}_t, z, t \right) \right]_{z=ct-s} . \qquad (6.2\text{-}1)$$
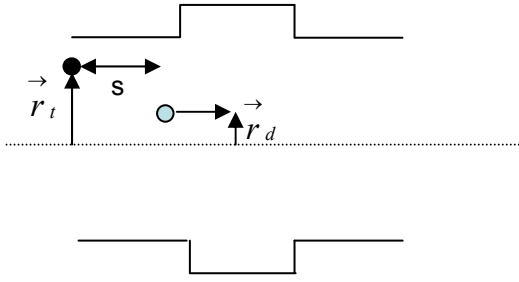
Figure 6.2.1.   A drive particle *d* leading a test particle *t* through a vacuum structure.

For $\vec{r}_t = \vec{r}_d = 0$, we define the longitudinal wakefield $w_\parallel(s)$ [volt/coul] by

$$w_\parallel(s) = -\frac{c}{q}\Delta p_z = -\frac{1}{q}\int_{-\infty}^{\infty} dz\, E_z\left(z, t = \frac{z+s}{c} \right), \qquad (6.2\text{-}2)$$

and the longitudinal impedance $Z_\parallel(k)$ [ohms] is determined by the Fourier transform,

$$Z_\parallel(k) = \int_{-\infty}^{\infty} \frac{ds}{c} w_\parallel(s) e^{iks} . \qquad (6.2\text{-}3)$$

For a Gaussian bunch containing N_e electrons, the energy loss is $\Delta E = \kappa_\parallel (eN_e)^2$ and the power loss is $P = \kappa_\parallel I_0^2 T_0$, where the energy loss factor $\kappa_\parallel$ [V/C] is given by

$$\kappa_\parallel = \int_{-\infty}^{\infty} \frac{c\,dk}{2\pi} \operatorname{Re} Z_\parallel(k) e^{-k^2\sigma_s^2} . \qquad (6.2\text{-}4)$$

The transverse wakefield [V/C-m] is

$$\vec{w}_{\perp}\left(s,\vec{r}_t,\vec{r}_d\right) = \frac{c}{q}\Delta\vec{p}_{\perp} = \frac{1}{q}\int_{-\infty}^{\infty}dz\left[\vec{E}\left(\vec{r},z,t\right) + c\,\hat{z}\times B\left(\vec{r},z,t\right)\right]_{t=\frac{z+s}{c}}. \tag{6.2-5}$$

The transverse impedance $\vec{Z}_{\perp}$ [Ω/m] is determined by the Fourier transform,

$$\vec{Z}_{\perp}\left(\vec{r}_t,\vec{r}_d,k\right) = \frac{-i}{c}\int_0^{\infty}ds\,\vec{w}_{\perp}\left(\vec{r}_t,\vec{r}_d,s\right)e^{iks}. \tag{6.2-6}$$

When the vacuum enclosure has reflection symmetry about the xz and yz planes, the transverse wakefield vanishes for $\vec{r}_t = \vec{r}_d = 0$ and the first terms in a Taylor expansion yield [6.2.6],

$$w_x\left(s,x_t,x_d\right) \cong w_{Dx}\left(s\right)x_d + w_{Qx}\left(s\right)x_t \tag{6.2-7}$$

$$w_y\left(s,y_t,y_d\right) \cong w_{Dy}\left(s\right)y_d - w_{Qy}\left(s\right)y_t \tag{6.2-8}$$

where w_D is the dipole wakefield and w_Q is the quadrupolar wake. The dipole and quadrupolar impedances are determined by the Fourier transforms

$$Z_x\left(x_t,x_d,k\right) \cong Z_{Dx}\left(k\right)x_d + Z_{Qx}\left(k\right)x_t \tag{6.2-9}$$

$$Z_y\left(y_t,y_d,k\right) \cong Z_{Dy}\left(k\right)y_d - Z_{Qy}\left(k\right)y_t \tag{6.2-10}$$

The coherent betatron tune shift in a Gaussian bunch of N_e electrons produced by the transverse dipole impedance is approximately given by

$$\Delta\nu_{x,y} = \frac{e^2 N_e}{4\pi E}\sum_j \beta_{x,y,j}\kappa_{x,y,j}, \tag{6.2-11}$$

where E is the electron energy and $\beta_{x,y,j}$ is the average value of the betatron function at the jth impedance element and $\kappa_{x,y,j}$ [V/C-m] is the kick factor of the jth element defined by

$$\kappa_{x,y,j} = \frac{c}{\pi}\int_0^{\infty}dk\,\mathrm{Im}\,Z_{Dx,y,j}\left(k\right)e^{-k^2\sigma_s^2}. \tag{6.2-12}$$

In a similar manner the quadrupolar impedance contributes to an incoherent tune spread. Some authors employ the effective impedance $\left(Z_{x,y}\right)_{eff}$ defined by

$$\left(Z_{x,y}\right)_{eff} = \frac{\int\limits_{-\infty}^{\infty} dk\, Z_{Dx,y}(k)\, e^{-k^2 \sigma_s^2}}{\int\limits_{-\infty}^{\infty} dk\, e^{-k^2 \sigma_s^2}} \tag{6.2-13}$$

The kick factor is related to the effective impedance by

$$\kappa_{x,y} = \frac{c}{2\sqrt{\pi}\sigma_s}\, \mathrm{Im}\left(Z_{Dx,y}\right)_{eff}. \tag{6.2-14}$$

To estimate instability thresholds, we use a model in which the impedance is comprised of a broadband resonator plus the resistive wall. The analytic forms for the wakefield and impedance of these elements are summarized in Table 6.2.1.

Table 6.2.1   Analytic Expressions for Impedance and Wakefield.

Resonator	
$Q' = \sqrt{Q^2 - 1/4} \qquad k_r' = k_r Q'/Q$	
$w_\parallel(s) = \dfrac{c k_r R_s}{Q_s} \exp\left(-\dfrac{k_r s}{2Q_s}\right) \left[\cos k_r' s - \dfrac{1}{2Q_s'} \sin k_r' s\right]$	$w_\perp(s) = \dfrac{c k_r R_\perp}{Q_\perp'} \exp\left(-\dfrac{k_r s}{2Q_\perp}\right) \sin k_r' s$
$Z_\parallel(k) = \dfrac{R_s}{1 - iQ_s\left(k/k_r - k_r/k\right)}$	$Z_\perp(k) = \dfrac{k_r}{k} \dfrac{R_\perp}{1 - iQ_\perp\left(k/k_r - k_r/k\right)}$
$\kappa_\parallel = \dfrac{\omega_r R_s}{2Q_s} \qquad (k_r \sigma_s \ll 1)$ $\kappa_\parallel = \dfrac{\omega_r R_s}{4\sqrt{\pi}\, Q_s^2 (k_r \sigma_s)^3} \qquad (k_r \sigma_s \gg 1)$ $(Z/n)_0 = R_s(\omega_0/\omega_r)$	$\kappa_\perp \cong \dfrac{1}{\sqrt{\pi}} \dfrac{c R_\perp}{Q_\perp} (k_r^2 \sigma_s) \quad (k_r \sigma_s \ll 1)$ $\kappa_\perp \cong \dfrac{c}{2\sqrt{\pi}\, \sigma_s} \dfrac{R_\perp}{Q_\perp} \qquad (k_r \sigma_s \gg 1)$
Resistive Wall [6.2.7]	
$s_0 = \left(2b^2 / Z_0 \sigma_{cond}\right)^{1/3}$	
$w_\parallel(s) \cong \dfrac{-cZ_0 L}{4\pi\sqrt{2\pi}\, b^2} \left(\dfrac{s_0}{s}\right)^{3/2} \qquad (s \gg s_0)$	$w_\perp(s) \cong \dfrac{cZ_0 s_0 L}{2\pi b^4} \sqrt{\dfrac{2 s_0}{\pi s}} \qquad (s \gg s_0)$
$Z_\parallel(k) \cong \dfrac{(1-i)Z_0 s_0 L}{4\pi b^2} \sqrt{k s_0} \quad (0 \le k \ll 1/s_0)$	$Z_\perp(k) \cong \dfrac{2}{kb^2} Z_\parallel(k) \quad (0 \le k \ll 1/s_0)$
$\kappa_\parallel \cong 1.2 \dfrac{cZ_0}{4\pi} \dfrac{L}{2\pi b^2} \left(\dfrac{s_0}{\sigma_s}\right)^{3/2}$	$\kappa_\perp \cong 0.58 \dfrac{c Z_0}{4\pi} \dfrac{2 s_0 L}{b^4} \sqrt{\dfrac{s_0}{\sigma_s}}$
Extreme Anomalous Skin Effect [6.2.8]	
$s_0 = (Bb)^{3/5} / \sin(\pi/10)$	
$B = 3^{1/6} 2^{-4/3} \pi^{-1/3} Z_0^{-1/3} (l/\sigma_{cond})^{1/3} \cong 3.9 \times 10^{-7}\, m^{2/3}$ (Cu @ 4 K, specular reflection)	
$w_\parallel(s) \cong \dfrac{-2cB Z_0 L}{3\pi\, \Gamma(1/3)b} s^{-5/3} \qquad (s \gg s_0)$	$w_\perp(s) \cong \dfrac{2c B Z_0 L}{\pi\, \Gamma(1/3)b^3} s^{-2/3} \quad (s \gg s_0)$
$Z_\parallel(k) \cong \dfrac{(1-\sqrt{3}\,i)B Z_0 L}{2\pi b} k^{2/3} \; (0 \le k \ll 1/s_0)$	$Z_\perp(k) \cong \dfrac{2}{b^2 k} Z_\parallel(k) \; (0 \le k \ll 1/s_0)$
$\kappa_\parallel = 0.16 \dfrac{cZ_0}{4\pi} \dfrac{L}{\pi b^2} \left(\dfrac{s_0}{\sigma_s}\right)^{5/3}$	$\kappa_\perp \cong 0.21 \dfrac{c Z_0}{4\pi} \dfrac{2 s_0 L}{b^4} \left(\dfrac{s_0}{\sigma_s}\right)^{2/3}$

6.2.3   Estimates of Instability Thresholds

To estimate the instability thresholds, we considered an approximate model of the storage ring impedance, including the long-range wakefield due to the longitudinal and transverse higher-order modes in the CESR-B cavities. The storage ring vacuum chamber is approximated by 720 m of aluminum with a vertical half-aperture of 12.5 mm. We also included 20 in-vacuum undulators, each with 3 m copper chambers of vertical half-aperture 2.5 mm. The geometric impedance due to cross-section changes in the vacuum vessel is approximated by longitudinal and transverse broadband resonators. The parameters for the resonators are based on experience at other storage rings [6.2.2, 6.2.9], especially APS and ESRF, as well as on the impedance calculations we have performed to date. We believe the model is conservative and that it may be possible to build NSLS-II with lower impedance. The details of the impedance model are presented in Table 6.2.2, and some key parameters needed in the estimation of instability thresholds are given in Table 6.2.3.

Table 6.2.2   Impedance Model.

CESR-B cavity higher-order modes (see Tables 6.2.4 and 6.2.5.)	$\beta_x = 18m$
720 m of aluminum with half-gap of 12.5 mm and β_{av} = 7.6 m:	$\kappa_{\parallel} = 4.0\,V/pC \quad \kappa_y = 0.68\,KV/pC/m$
60 m of copper with half-gap of 2.5 mm and β_{av} = 2 m:	$\kappa_{\parallel} = 1.3\,V/pC \quad \kappa_y = 5.6\,KV/pC/m$
Transverse broadband impedance with f_r = 30 GHz, R_y = 1 $M\Omega$/m, Q_y=1, and β_{av} = 7.6m	$\kappa_y = 19\,KV/pC/m$
Longitudinal broadband impedance with $f_r = 30GHz$, $R_s = 30k\Omega$,	$\left(\mathrm{Im}Z_{\parallel}/n\right)_0 = 0.4\Omega \quad \kappa_{\parallel} = 35V/pC$

Table 6.2.3   Parameters for Threshold Calculations

Energy, E [GeV]	3
Revolution period, T_0 [μs]	2.6
Momentum compaction, α	3.7×10^{-4}
Energy loss, U [keV]	1172
RF voltage, V [MV]	3.7
Synchrotron tune, ν_s	0.0094
Damping time: τ_x, τ_s [ms]	13, 6.5
Energy spread, $\sigma_{\varepsilon 0}$ [%]	0.09
Bunch duration, σ_{t0} [ps]	15

6.2.3.1   Transverse Mode Coupling Instability (TMCI)

An approximate relation [6.2.10] determining the threshold of the TMCI at zero chromaticity is given by

$$\frac{\Delta \nu_y}{\nu_s} = \frac{e\, I_0^{th}}{2\,E\,\nu_s\,\omega_0} \sum_j \beta_{yj}\kappa_{yj} \cong 0.7 \,, \tag{6.2-15}$$

where I_0^{th} is the threshold bunch current, β_{yj} is the average value of the vertical beta function in the jth element, and κ_{yj} is its kick factor. $E = \gamma\,mc^2$ is the electron energy and ν_s is the synchrotron tune. Consider a current of 0.5 mA bunch. Using the NSLS-II parameters as described in Table 6.2.3, we find that to be below the TMCI threshold requires

$$\sum_j \beta_{yj}\, \kappa_{yj} < 180\ KV/pC\,.$$

(6.2-16)

Using the values of the kick factors and beta functions as specified in Table 6.2.2, we find that $\sum_j \beta_{yj}\, \kappa_{yj} = 160\ KV/pC$. Therefore, 0.5 mA bunches are below the TMCI threshold for zero chromaticity.

6.2.3.2 Longitudinal Microwave Instability

At very low single-bunch current, the longitudinal density is determined by the equilibrium between radiation damping and quantum fluctuations. As the bunch current increases, the longitudinal charge distribution is modified by the wakefield. Below the threshold of the microwave instability, the energy distribution remains unchanged, and the longitudinal charge distribution $f_0\left(\tau/\sigma_{\tau 0}\right)$ is determined by the time-independent solution of the Haissinski equation [6.2.11],

$$f_0(q) = A \exp\left[-\frac{1}{2} q^2 + S \int_q^{\infty} dq' \int_{q'}^{\infty} dq'' f_0(q'') w(q''-q') \right],$$

(6.2-17)

where the constant A is chosen to satisfy the normalization

$$\int_{-\infty}^{\infty} dq f_0(q) = 1$$

(6.2-18)

In the case of a broadband resonator with shunt impedance R_s, resonant frequency ω_s, and quality factor $Q_s = 1$, the scaled current is defined by

$$S = \frac{e\, I_0\, R_s\, \omega_r}{E_0\, \nu_s\, \omega_0\, \sigma_\varepsilon}$$

(6.2-19)

and

$$w(q) = \exp\left(-\frac{q \omega_r \sigma_{t0}}{2} \right)\left[\cos\left(q\omega_r'\sigma_{t0}\right) - \frac{1}{2\sqrt{0.75}} \sin\left(q\omega_r'\sigma_{t0}\right) \right].$$

(6.2-20)

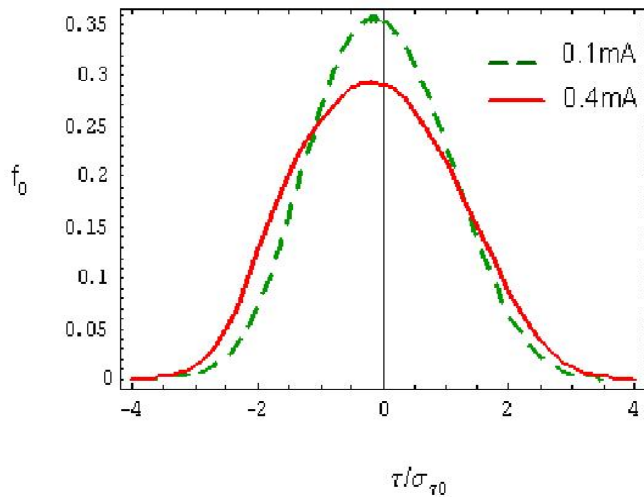In Figure 6.2.2, we show the Haissinski distribution for currents of 0.1 mA and 0.4 mA.

Figure 6.2.2 Longitudinal distribution as determined from the Haissinski equations.

Once the current exceeds the microwave instability threshold, both the energy distribution and the charge distribution are modified and are no longer time-independent. In the case of a broadband resonator with shunt impedance R_s, resonant frequency ω_s, and quality factor $Q_s = 1$, Oide and Yokoya [6.2.12] have shown that the single-bunch current threshold is given by

$$I_0^{th} = \frac{E \nu_s \sigma_\varepsilon}{e R_s \left(\omega_r / \omega_0 \right)} S\left(\omega_r \sigma_t \right).$$

(6.2-21)

In Figure 6.2.3, we show the function $S\left(\omega_r \sigma_t\right)$ as determined by Oide and Yokoya (solid curve), and by tracking using the computer code ELEGANT [6.2.13] (symbols). A useful fit to the scaling function, in the regime x >0.2, is given by

$$S(x) = 11 + 9.4(x - 0.7)^2.$$

(6.2-22)
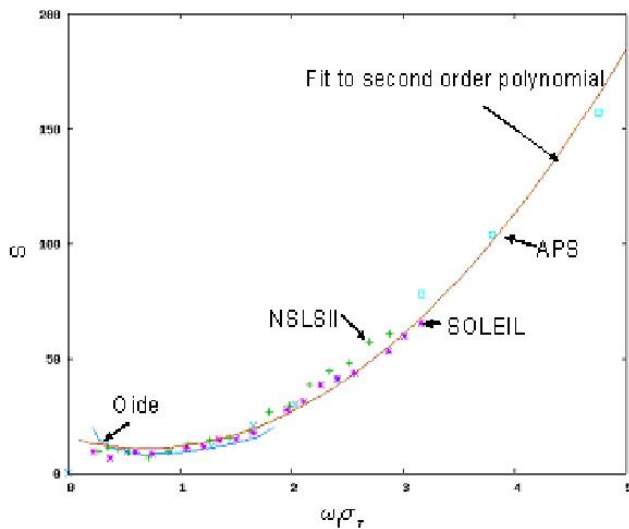
Figure 6.2.3. The scaling function $S\left(\omega_r \sigma_{t0}\right)$ as determined by Oide and Yokoya (solid curve) and by tracking using ELEGANT (characters). The threshold is defined to be when the energy spread has increased by 5% over the zero current value.

In the limit when $\omega_0 \sigma_{t0} \gg 1$, the threshold condition becomes

$$I_0^{th} = 9.4 \frac{E v_s^2}{e\alpha (\mathrm{Im} Z / n)_0} (\omega_0 \sigma_{t0})^3,$$ (6.2-23)

where $(\mathrm{Im} Z / n)_0 = R_s (\omega_0 / \omega_r)$. This has the same form as the Boussard [6.2.14] criterion, except that in the Boussard case, the constant 9.4 is replaced by the smaller value $\sqrt{2\pi}$. The reason that the Boussard criterion gives too pessimistic a threshold is that it does not take into account the bunch lengthening due to potential well distortion.

In Figure 6.2.4, we show the dependence of the bunch length and the energy spread as calculated using the program ELEGANT. This shows that 0.5 mA bunches will suffer negligible increase in energy spread due to the longitudinal microwave instability.
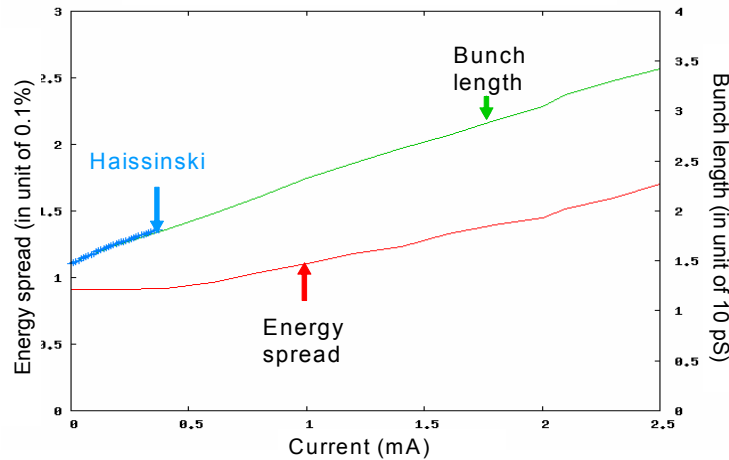
Figure 6.2.4. Bunch length and energy spread for broadband resonator. Resonant frequency $f_\gamma = 30$ GHz, shunt impedance $R_s = 30\ k\Omega$, and $Q_s = 1$. This corresponds to $(\mathrm{Im}Z/n)_0 = 0.4\ \Omega$.

6.2.3.3 Transverse Coupled Bunch Instability Driven by Resistive Wall Impedance

As discussed in Section 6.2.3.1, the short-range part of the resistive wall impedance contributes to the single-bunch TMCI. The long-range tail contributes to the transverse coupled bunch instability. A rough approximation to the growth rate of the fastest growing transverse coupled bunch mode driven by the resistive wall impedance (at zero chromaticity) is given by

$$\frac{1}{\tau_{gr}} \cong \frac{e c I_{av}}{2 E} \frac{\beta_y}{C} \mathrm{Re} Z_\perp^{rw}(\omega_0) \frac{1}{\sqrt{1-q}},$$ (6.2-24)

where C = 780 m is the ring circumference, β_y is the average value of the vertical beta function in the resistive wall, and q = 0.28 is the fractional part of the vertical tune. Equating the growth time to the radiation damping time provides an estimate of the instability threshold. Using the model parameters given in Tables 6.2.2 and 6.2.3, we find the threshold is at a total average current of 15 mA, far below the design value of 500 mA. Running at positive chromaticity will increase this threshold value.

Particle tracking [6.2.15] has been used to estimate transverse stability thresholds for coupled bunch modes. In these calculations we include both the long-range and short-range resistive wall wakefields as well as the short-range longitudinal and transverse wakefields, as described in Table 6.2.2. To keep the problem

manageable, we assume that all RF buckets contain identical bunches interacting via a single coupled bunch mode. A single bunch is tracked and the effect of other bunches is obtained by appropriate phase shifts under the assumption that the coherent frequency shift is small compared to the characteristic frequency width in the long-range transverse impedance. This should be an excellent approximation for the resistive wall impedance, which dominates the long-range transverse wake. The resistive wall impedance is due to 60 m of Cu with vertical aperture 5 mm and average beta function 2 m, in conjunction with 720 m of Al with aperture 25 mm and average beta function 7.6 m. The broadband transverse resonator has $R_\perp$ = 1 M-Ohm/m with $Q_\perp$ = 1 and 30 GHz resonant frequency at beta function 7.6 m. A longitudinal resonator with R_s = 30 k-Ohm, resonant frequency 30 GHz, and Q_s = 1 dominates the longitudinal impedance.

Three cases were simulated. Case 0 is a "stripped" case with no longitudinal wakes, no quadrupolar wakes (also referred to as detuning wakes), and no third-harmonic RF. Case 1 has the full suite of collective effects but no third harmonic cavity. Case 2 includes a perfect third harmonic cavity. The single-bunch threshold current as a function of vertical chromaticity is shown in Figure 6.2.5. In cases 1 and 2, a chromaticity of 4 allows for an average bunch current of about 0.5 mA and hence for an average stored current of 500 mA. This demonstrates the importance of running at positive chromaticity. Note also that bunch lengthening and enhanced synchrotron frequency spread introduced by the longitudinal wakefield and the third-harmonic cavity increase the effectiveness of positive chromaticity to stabilize the beam.
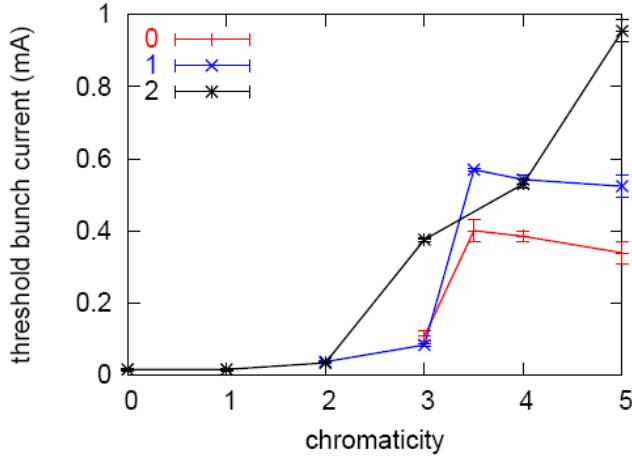

Figure 6.2.5   Threshold single bunch current vs. chromaticity for: (0) no longitudinal wakes, no quadrupolar wakes, and only fundamental RF; (1) all the impedances but only fundamental RF; (2) all impedances as well as fundamental and third-harmonic RF.

6.2.3.4   CESR-B Cavity Longitudinal Impedance and Coupled Bunch Growth Rates

The longitudinal higher-order modes (HOM) in an RF cavity can result in coupling between bunches, leading to unstable synchrotron oscillations. In the case of M equally spaced and populated point bunches, the coherent synchrotron frequency Ω_μ of the μth multi-bunch mode can be approximated by

$$\Omega_\mu - \omega_0 \nu_s = \frac{i e \alpha \omega_0 I_{av}}{4 \pi \nu_s E} \sum_{j=-\infty}^{\infty} (M j + \mu) Z_\| \big[(M j + \mu + \nu_s)\omega_0\big] \qquad (6.2-25)$$

and

$$(\mu = 0,1,2,\ldots,M-1). \qquad (6.2-26)$$

A 3D GdfidL [6.2.3] model has been created for the CESR-B cavity [6.2.16]. The model consists of the niobium cavity with the asymmetric beam tubes, warm-to-cold transitions, and ferrite-lined HOM dampers, and it tapers to the 25×50 mm elliptical ring beampipes. The cavity has a fluted beam tube that allows the

lowest dipole mode to be coupled out to the HOM damper. This made it essential to use a 3D model for calculating the HOMs. To benchmark such a complex model, C-Fish [6.2.17] and Superfish [6.2.18] models of the cavity with complex permitivity and permeability were created. The results were compared to GdfidL and to measured data on a ferrite-lined pillbox cavity that was measured on the bench.

The Superfish model approximates the fluted beampipe by a cylindrical tube with the same cutoff frequency. An outline of the cavity geometry with the field lines of the 1586 MHz mode is shown in Figure 6.2.6.
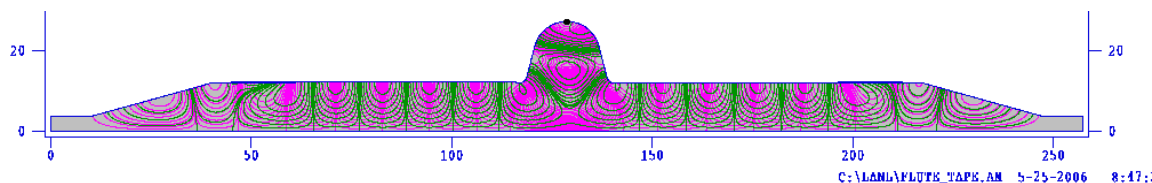
Figure 6.2.6   CESR-B cavity geometry input to C-Fish.

The first eight HOMs calculated are given in Table 6.2.4. Superfish correctly calculates the surface resistivity of niobium as a function of frequency, but only takes the complex permeability and permitivity as a single input. The permitivity of the ferrite load is relatively constant and does not contribute significantly to damping the HOM, but the ferrite permeability properties vary considerably, so specific values (Table 6.2.4) closest to the HOM frequencies were calculated. The ferrite properties were obtained from the Canadian Light Source [6.2.19]. The measurements were made at several discrete frequencies in the band of interest.

Table 6.2.4   CESR-B Higher-Order Longitudinal Modes.

Superfish			GdfidL		
Frequency (MHZ)	Shunt Impedance (Ohms)	Q	Frequency (MHZ)	Shunt Impedance (Ohms)	Q
952.4	112	222	950.55	8.14	350
973.32	57.07	332	976.62	54.6	420
1014.85	498	112	1014.38	505	150
1184.65	44.1	43	1181.5	13.2	60
1331.15	38.7	40	1361	65.6	20
1487.5	12.5	53	1481.5	46	40
1586.58	27.8	169	1580	7.5	30

We also performed studies of HOMs in CESR-B assembly using GdfidL code, shown in Figure. 6.2.7. The studies took off from time-domain simulation of 1 pC charge passing through the structure. For the longitudinal impedance computation, the beam is moving on-axis, in comparison with the transverse impedance computation when the beam trajectory is shifted off-axis with an offset taken as 3×STEPSIZE. To get a result for the impedance, which is Fast Fourier Transforming of the wake function with higher frequency resolution, the wakepotenial is computed up to an s-value of 50 meters. Parameters of the ferrite material are taken as $\varepsilon_r = 13.4$, $\mu_r = 0.9$, $\tan\delta_\varepsilon = 0.02$, $\tan\delta_\mu = 2.33$, $\sigma_\varepsilon = 0.05$ Ω^{-1}/m^{-1}, and $\sigma_\mu = 46395$ Ω/m at a frequency of 2.8 GHz [6.2.19].
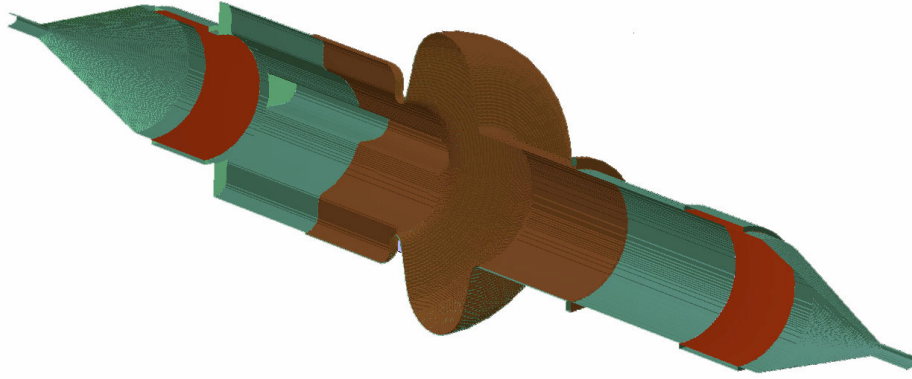
Figure 6.2.7   3D model of CESR-B cavity assembly in GdfidL.

These parameters were used in ZAP [6.2.20] to calculate the growth rates for nominal ring and beam parameters. The maximum growth time was 120 ms for the sum of three cavity impedances, much longer than the longitudinal damping time of 6.5 ms, and so the beam is longitudinally stable for cavity HOMs.

To summarize the CESR-B cavity studies, longitudinal CB growth rates were calculated for the first few HOM of the CESR-B cavity and were found to be below the damping rate, even for three installed cavities without stagger tuning. However, the combination of small-bunch length exciting higher frequency modes and ferrite loss decreasing at higher frequency could lead to unstable modes whose growth rate exceeds the damping rate, so this analysis must be extended to higher frequencies. To enable this, we are pursuing measurements of the ferrite properties to 6 GHz with Ron Hutcheon, who provided the data below 3 GHz that were used in these calculations. This work must also be extended to the third harmonic cavities.

6.2.3.5   CESR-B Cavity Transverse Impedance and Coupled Bunch Growth Rates

The transverse higher-order modes in an RF cavity can result in coupling between bunches, leading to unstable betatron oscillations. In the case of M equally spaced and populated point bunches, the coherent synchrotron frequency Ω_μ of the μth multi-bunch mode can be approximated by

$$\Omega_\mu - \omega_0 \nu_x = -i \frac{e\,c\,I_{av}}{2\,E} \frac{\beta_x^{cav}}{C} \sum_{j=-\infty}^{\infty} Z_\perp \big[\big(M\,j + \mu + \nu_y \big) \omega_0 \big],$$

(6.2-27)

where $\mu = 0,1,2,\ldots M-1$). The same GdlfidL model used to compute the longitudinal cavity impedances was used to compute the transverse modes. The first 15 modes are listed in Table 6.2.5.

Table 6.2.5   CESR-B Higher-Order Transverse Modes.

Time domain #	Frequency [MHz]	$R_\perp$ [kΩ/m]	$Q_{\perp,load}$
$f1$	608	2.2	60
$f2$	653	3.1	60
$f3$	681	15.6	70
$f4$	769	1.6	30
$f5$	864	1.03	50
$f6$	917	0.72	40
$f7$	964	0.66	30
$f8$	1045	0.8	30
$f9$	1146	1.17	30
$f10$	1243	2.3	70
$f11$	1299	0.36	160
$f12$	1344	0.31	40
$f13$	1405	0.33	70
$f14$	1433	0.22	100
$f15$	1464	0.44	70

The horizontal betatron function is 18 m at the RF cavities. These modes were used in ZAP [6.2.20] to calculate the transverse coupled-bunch growth rates. For 500 mA average current distributed uniformly in all the buckets around the ring and zero chromaticity, the coupled bunch growth time is 40 ms, which is longer than the radiation damping time of 13 ms. Therefore, the transverse cavity modes will not lead to unstable coupled-bunch betatron oscillations.

6.2.4   Impedance Budget

Extensive calculations have been performed of the wakefield and impedance produced by the storage ring components. Results of the calculations are summarized in Table 6.2.6, where we present the longitudinal kick factor (Eq. 6.2-4)], the transverse kick factors (Eq. 6.2-12) and the imaginary part of the longitudinal impedance at low frequency divided by $n = \omega/\omega_0$. The values given correspond to a single element. The number of times a given object is located in the ring is stated.

Table 6.2.6   Calculated Impedance for Storage Ring Components.

Object	Number of occurrences	$\kappa_\parallel$ V/pC	$(ImZ_\parallel/n)_0 \Omega$	κ_x V/pC/m	κ_y V/pC/m
Absorber	180	3.4×10^{-3}	9.2×10^{-6}	0.5	0.002
Bellows [1]	180	8.7×10^{-3}	124×10^{-6}	0.8	2
BPM	270	20×10^{-3}	47×10^{-6}	0.9	1.1
CESR-B cavity	3	3.6	40×10^{-3}	58	58
Dipole Chamber	60	0.24×10^{-3}	0.5×10^{-6}	0.045	0.0
Flange [1]	300	0.47×10^{-3}	16×10^{-6}	0.141	0.141
Injection Region	1	TBD	TBD	TBD	TBD
SCU chamber geometric	TBD	7.4×10^{-3}	495×10^{-6}	58	190
SCU chamber ease	TBD	5.6×10^{-3}		13	26
IR chamber	-5	TBD	TBD	TBD	TBD
CPMU geometric	TBD	95×10^{-3}	1.1×10^{-3}	136	425
CPMU resistive wall	TBD	66×10^{-3}		112	225
Al resistive wall	1	4.0		272	545
Scraper	2	TBD	TBD	TBD	TBD

[1]Values for bellows and flanges were calculated by Nagaoka [6.2.21] for SOLEIL with σ_s = 6 mm. The values for the CESR-B cavity were calculated using GdfidL with σ_s = 4 mm. The other geometric impedances were calculated with σ_s = 3 mm. The resistive wall and extreme anomalous skin effect estimates were made with σ_s = 4.5 mm. The bunch-length dependence of the wakefields will be determined in future work.

The Al vacuum chamber is taken to be of length 720 m with vertical half-height 12.5 mm. The copper-plated RF shield for the in-vacuum permanent magnet undulator is 3 m long with vertical half-height of 2.5 mm. The superconducting undulator chamber is 2 m long with vertical half-height 2.5 mm and is cold copper in the extreme anomalous skin effect regime [6.2.8]. The vertical resistive wall wake of the elliptic chamber is taken to be 0.8 times the value for the circular chamber and the horizontal wake is 0.4 times the circular value [6.2.22]. Results not yet determined are indicated in the table.

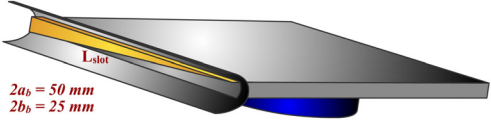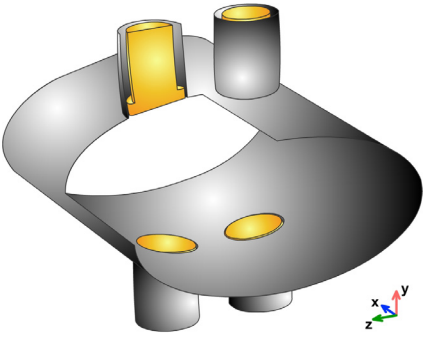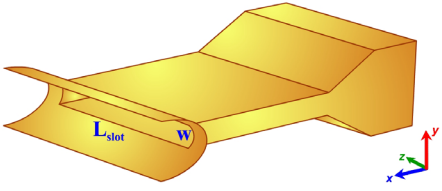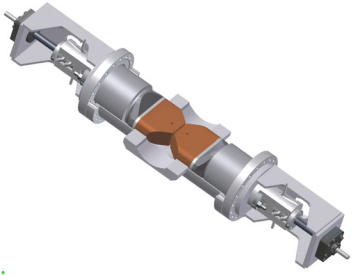### 6.2.4.1   Insertion Device Chambers

While most of the components listed in Table 6.2.7 are fairly common and have been successfully used in many machines, we feel that significant attention is warranted for studies and optimization of the impedance due to insertion device chambers. This need is based on experience at modern light sources, where installations of small-gap ID chambers have significantly affected beam dynamics [6.2.24], as well as on the requirements for NSLS-II, which is expected to have a large number of ID chambers (~20) with gap down to 5 mm beam stay-clear. Both the resistive wall component and the geometric component due to the transitions have been studied. Furthermore, in addition to the dipole impedances, which directly cause beam instabilities, we have estimated the quadrupolar component [6.2.25], which results in incoherent frequency shift and indirectly contributes to the instabilities through the Landau damping.

For the purposes of impedance budget we consider two representative ID chamber geometries: 1) a variable-gap, in-vacuum, permanent magnet undulator, and 2) a 5 mm fixed-gap elliptical chamber (4.2 K Cu inner surface) for a superconducting small-gap undulator.

Resistive wall contribution has been estimated analytically. While the inner chamber cross-sections are either complex H-like or elliptical shapes we have conservatively used the formulas in Table 6.2.1 for round cross-sections. It is known [6.2.22] that as the chamber gets flatter (while height is kept fixed), the longitudinal impedance passes through a minimum equal to about 90% of the round-pipe value, while the transverse impedance monotonically approaches ~80% of its round-pipe value. Copper coating and a minimum full gap of 5 mm were assumed for the estimates.

Geometric impedance contributions due to transitions [6.2.26] were calculated using EM code GdfidL [6.2.3] as well as checked against a recently developed analytical approach [6.2.25].

Table 6.2.7   Description of Components.

Absorber

To protect the vacuum chamber and insertion devices in the ring from damage due to synchrotron radiation, photon absorbers are used. The model consists of a regular elliptical beampipe with 50 mm (W) and 25 mm (H), with a rectangular slot 10 mm high, 180 mm long, and 180 mm deep. A triangular copper burr is located inside the slot for synchrotron radiation absorption. It projects 5 mm inside the regular elliptical beampipe.

BPM

Due to excitation of resonant modes in the buttons, the impedance, kick factor, and loss factor depend very strongly on the BPM button geometry. The BPM button geometry can be optimized to reduce impedance contribution and heating, without losing its resolution. To estimate BPM contribution to the transverse and longitudinal impedance, buttons designed for the SOLEIL BPM were modeled on the regular elliptic beampipe for NSLS-II. Results of the transverse impedance were compared with results for the SOLEIL BPM geometry; in both cases, 50 Ω/m was computed.

Dipole Chamber

The dipole vacuum chamber for NSLS-II has an elliptical cross-section. Inside the chamber there is a slot 10 mm high. As was shown by Stupakov [6.2.23], the slot length does not affect the impedance. For this numerical computation, the slot length is taken to be 80 mm. The horizontal impedance of this geometry depends on beampipe radius and height of the slot.

Scraper-H

From the impedance estimations of other laboratories, horizontal or vertical beam scrapers can produce impedance comparable with that of a rectangular step or a tapered transition with a small angle of opening. Two scrapers of the presented geometry, one horizontal and the other vertical, are under consideration for application in the NSLS-II ring.

6.2.4.1.1   In-Vacuum Undulator

A 3D model of the CPMU [6.2.26] is shown in Figure 6.2.8 (a, top). This model is motivated by the geometry of the X13 Mini-Gap Undulator [6.2.27] currently operating at the NSLS x-ray ring and has been tailored to meet the NSLS-II requirements. The device consists of two magnet arrays of width $w_m = 100$ mm and thickness 34 mm, located inside a rectangular vacuum chamber of width $w_{vc} = 180$ mm and height $h_{vc} = 170$ mm. The tapered transition consists of two parts: 1) a fixed portion between the regular beampipe and the undulator vacuum chamber; and 2) a flexible-height portion with one end fixed to the interior of the undulator vacuum chamber and the other end fixed to the moveable magnet array. The flexible portion only consists of flat upper and lower conductive plates with no side walls. For simplicity in the 3D model, we used a

continuous smooth taper of length 180 mm. Also, due to mesh limitations, we have shortened the magnet section length to 0.5 m.

Figure 6.2.8 (a, bottom) shows the transverse wakepotential for the considered geometry and 3 mm RMS bunch length. The wakepotential has a Gaussian-like part corresponding to mainly inductive broadband impedance, as well as a characteristic long-range tail.

The short-range wakefield in the CPMU is predominantly determined by the tapers; the long-range wake depends on the cross-sectional geometry of the vacuum enclosure and the length of the magnet. The oscillations in the long-range part are due to multiple narrowband impedance resonances that are possible to characterize in terms of waveguide theory [6.2.28]. Due to limitations on the mesh, we have not yet been able to carry out a systematic study of the length dependence.

a   **b**
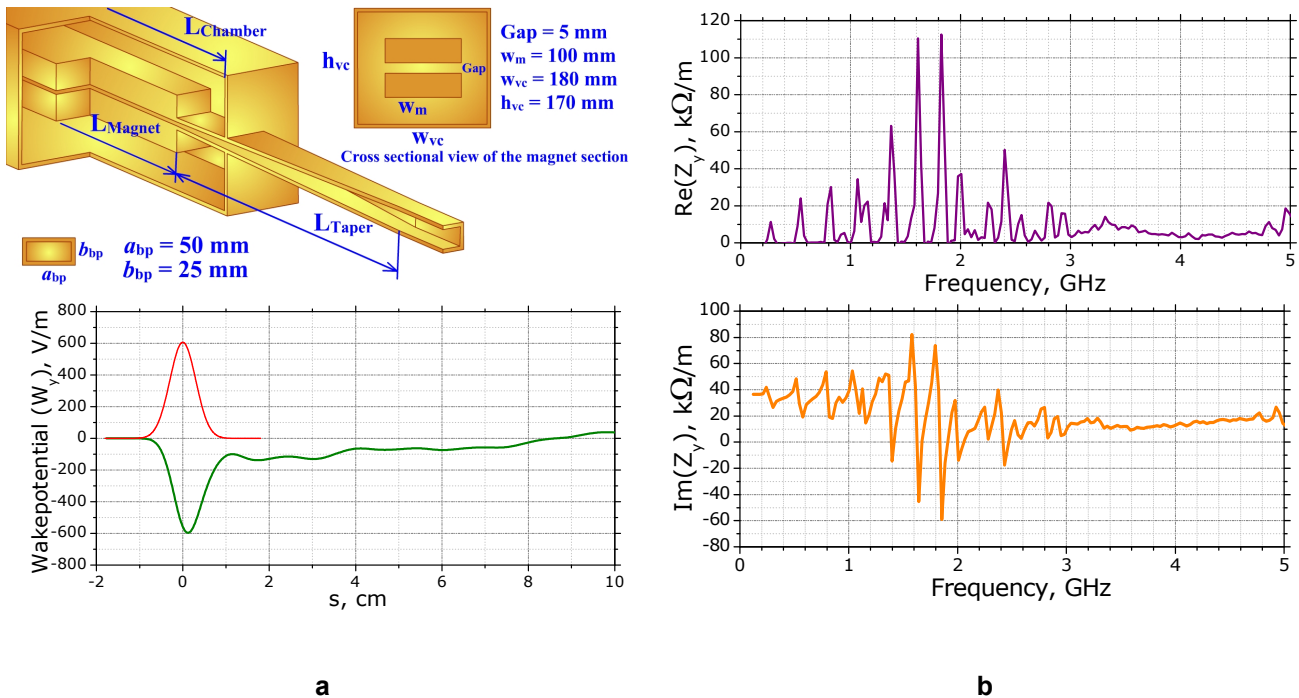
Figure 6.2.8 (a, top) Geometry of CPMU with L_{taper} = 180 mm; (a, bottom) Short-range transverse wakepotential of in-vacuum permanent magnet undulator chamber; (c, top and bottom) Low-frequency behavior of the real and imaginary parts of the transverse impedance of CPMU. Impedances determined by FFT of the computed wakepotential up to s = 7 m.

6.2.4.1.2   Superconducting Undulator

Similar calculations were performed for the elliptic vacuum chamber of a superconducting undulator. The geometry of the tapered elliptic vacuum chamber is shown in Figure 6.2.9 (a, top). The small-gap magnet region of the elliptic vacuum chamber for the superconducting undulator is fixed and has major axis $2a_s$ = 15 mm and minor axis $2b_s$ = 5 mm, with a magnet section length of 2000 mm. The tapers must smoothly transition between the magnet section and the regular beampipe, which has a major axis $2a_b$ = 50 mm and minor axis $2b_b$ = 25 mm.

Transverse impedance in the low-frequency limit and the kick factor for the tapered vacuum chamber are independent of the distance between the tapers. The inner section length was reduced to 100 mm for GdfidL calculations. The resulting wakepotential for 3 mm RMS long bunch and the taper length of L_{Taper} = 180 mm

is shown in Figure 6.2.9 (a, bottom). It corresponds to κ_y = 190 V/pC/m and Im Zy($\omega\rightarrow$0) = 6.5 kΩ/m. When we increased the taper length, κ_y and Im Z_y($\omega\rightarrow$0) decreased inversely proportional to L_{Taper}. The taper length of the elliptic vacuum chamber is chosen to optimize its contribution to the total impedance as well as space in the ring. Note that resonance peaks are observed inside the vacuum chamber in all cases of the transverse impedance calculations. These peaks are not resolved with a wakefield length of 1.5 m. A more detailed investigation of the electrodynamic properties of the tapered elliptic vacuum chamber uncovered the existence of trapped modes. These modes have been identified and classified [6.2.28]. In principle, these modes may affect multi-bunch dynamics and will be systematically studied.
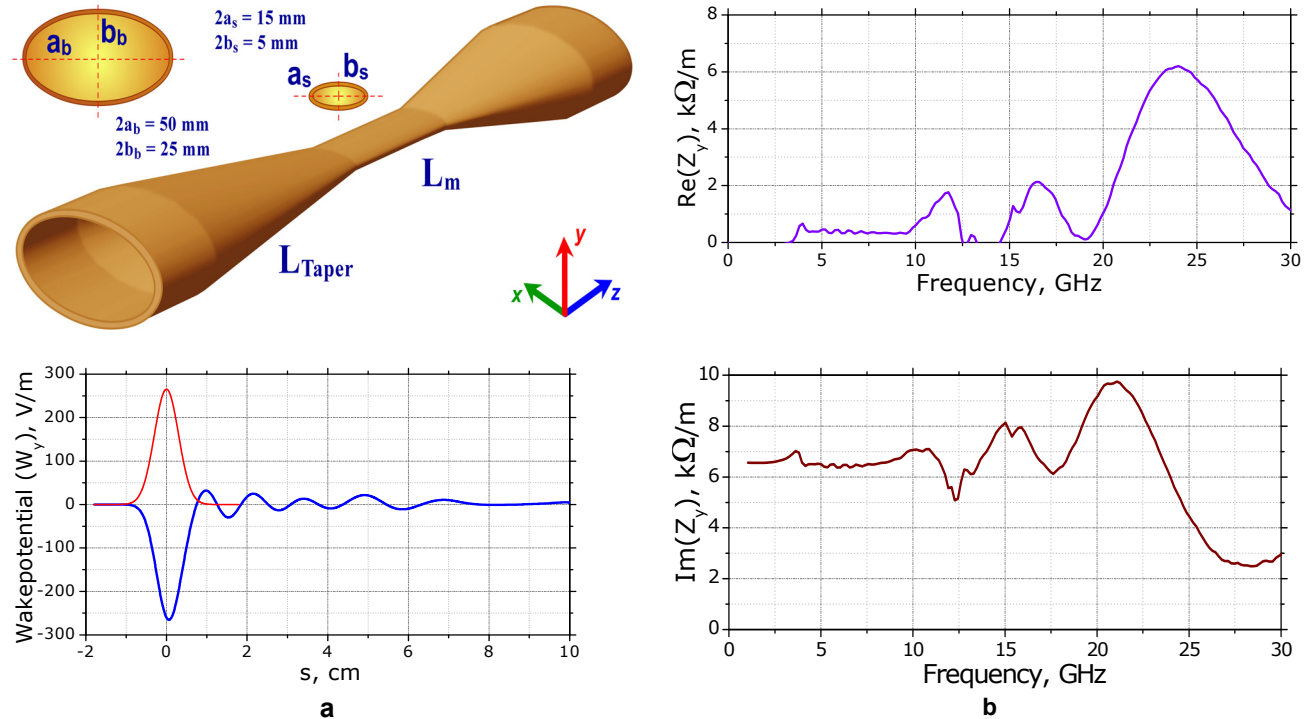
Figure 6.2.9 (a, top) Tapered elliptical vacuum chamber for superconducting small-gap undulator (L_{Taper} = 180 mm). (a, bottom) Transverse wakepotential; (b, top) Real part of the transverse impedance. (b, bottom) Imaginary part of the transverse impedance. Impedances correspond to FFT of the computed wakepotential up to s = 1.5 m.

6.2.4.2   CESR-B Short-Range Wake

CESR-B type superconducting cavities are considered here for acceleration of the beam in the NSLS-II storage ring. Two main 500 MHz RF cavities are required. In addition, one passive 1500 MHz bunch lengthening harmonic cavity will be located in the ring. To avoid additional transitions between the round pipes of cavities and the elliptical regular beampipe, three cavities (two main cavities and one harmonic cavity) are planned for installation in one straight section and the remaining cavities in the other straight section. The complicated nature of the RF cavities will require significant computational resources, to establish the longitudinal and transverse impedances for these assemblies. The most difficult part is a computation of the short-range wakefield for a 3 mm RMS bunch length. These data are required for determining the kick and loss factors.

Investigation of longitudinal and transverse impedances of cavities and transitions [6.2.29, 6.2.30] has begun, using simplified geometries. The first approximation simplifies the geometry of a single cavity as currently installed in the Cornell Electron Storage Ring, CESR. The 3D model of the 500 MHz CESR-B assembly is shown in Figure 6.2.7. Its length is 2.6 m. The geometry consists of the single main 500 MHz RF

cavity with the attached round beampipe of 120 mm on one side, and the fluted beampipe for HOM coupling on the other. Inside the round beampipe, close to the transition on both sides of the structure, ferrite material is located for HOM damping. Our first calculations were done using a thickness of 10 mm, due to the limitations in the mesh size. In the future, calculations will be done for the realistic thickness of 3.2 mm. Parameters of the ferrite material C-48 at different frequencies are taken from a [6.2.19]. They are presented only up to a frequency of 2.8 GHz. Using these data, we have analyzed the contribution to the longitudinal and transverse impedance due to the CESR-B assembly. The RF coupler is not included in these computations. This simplification allows using a quarter of the structure, which drastically reduces required computer resources and computation time.

The current structure has two tapered transitions. The regular beampipe planned for the NSLS-II storage ring has an elliptical cross-section 50 mm wide and 25 mm high. The round beampipe attached to the 500 MHz RF cavity has a radius of 120 mm. To accommodate the difference in cross-sections, smooth transitions must be provided. Their lengths should be calculated to optimize for transverse and longitudinal impedances. Every transition contributes to the impedance. However, in each round beampipe, near each tapered transition, ferrite material is located for HOM damping. Transitions cannot be accurately estimated without including the effects of the ferrite material because the modes generated at discontinuities by a passing bunch can be damped in the ferrite material. Hence, to get approximate impedance data from these tapered transitions, ferrite material should be included in the analysis.

Table 6.2.6 (beginning of Section 6.2.4) presents results of the kick factor and the loss factor for a 4 mm RMS bunch length. These data are a sum of numerical computations in the two separate geometries. The first geometry is a simple RF cavity with attached round and fluted beampipes. On the end of the pipes, "PORT" boundary conditions were specified. The second geometry is a round beampipe, lined with ferrite material, with a radius of 120 mm transitioning by 300 mm tapers on both sides to the regular elliptical beampipe. In this way, the cavity contribution was calculated separately from the rest of the assembly.

6.2.5   Intrabeam Scattering

Small-angle Coulomb scattering within a beam leads to the excitation of betatron and synchrotron oscillations of particles, which usually increases beam emittances in all phase planes. This effect, often called intra-beam scattering (IBS) or multiple Coulomb scattering, is proportional to the beam 3D phase-space density and depends strongly on beam energy, becoming more severe for high intensity, low energy machines.

When IBS is included, the steady-state beam properties with radiation damping are defined by

$$\varepsilon_x = \frac{\varepsilon_{x0}}{1 - \tau_x / T_x}, \quad \varepsilon_y = \frac{\varepsilon_{y0}}{1 - \tau_y / T_y}, \quad \sigma_p^2 = \frac{\sigma_{p0}^2}{1 - \tau_p / T_p}, \tag{6.2-28}$$

where subscript 0 indicates the beam properties in the absence of IBS, $\tau_{x,y,p}$ stand for synchrotron radiation damping times, and $T_{x,y,p}$ are the IBS growth times discussed below. These equations indicate that the IBS effect becomes important when IBS rates are significant in comparison with the radiation damping rates. Because the IBS growth times $T_{x,y,p}$ depend on beam current as well as beam emittances, energy spread, and bunch length, the above equations are coupled, and solving them requires some iterative procedure. Sometimes a fourth equation is added that expresses the current-dependent relation of the bunch length to the energy spread, to account for the potential well distortion. If the vertical emittance is dominated by weak coupling (which is our expectation for NSLS-II), the effect simplifies to 2D, and the second equation is replaced by $\varepsilon_y = \kappa \, \varepsilon_x$, where κ stands for the coupling coefficient.

The basic theoretical framework of IBS effect was established long ago by Piwinski [6.2.31] and Bjorken and Mtingwa (B–M) [6.2.32] using two different approaches. These theories express IBS rise times $T_{x,y,p}$ as

complicated integrals of beam parameters, such as energy and phase space density, as well as lattice properties. The B–M theory has been extended to include arbitrary vertical-horizontal and vertical-longitudinal coupling [6.2.33]. The resulting growth rates are local quantities, and have to then be averaged around the lattice. Many accelerator physics codes include some variations of the B–M approach. In addition to these general procedures which are fairly computer intensive, there exist a number of more approximate formulations of IBS effect that simplify the treatment for certain parameter regimes. For example, Bane [6.2.34] has recently shown the equivalence of the Piwinski and B–M treatments in the regime applicable for high energy machines. In this regime, Bane has found that B–M results reduce to fairly compact expressions for IBS rise times, which we have found useful for NSLS-II.

The IBS approaches mentioned above result in growth times proportional to the so-called Coulomb log factor, equal to $ln(b_{max}/b_{min})$, where $b_{max, min}$ are impact parameters, which are not well defined. Often, b_{max} is taken equal to σ_y. To fix b_{min}, a so-called "tail-cut" procedure was suggested by Raubenheimer [6.2.35]. He pointed out that, since IBS results in non-Gaussian beam distributions, tail particles could be overemphasized; therefore, one must chose b_{min} to eliminate interactions having collision rates smaller than SR damping rates.

The NSLS-II emittance is strongly dominated by the IDs and damping wigglers. Rather than assuming some fixed ID makeup, we have calculated IBS effects as a function of radiation losses in the machine, having ε_{x0} vary from the ~2 nm bare lattice value down to about 0.4 nm. The zero-current vertical emittance ε_{y0} was fixed at the diffraction limit for 1 Å x-rays (8 pm-rad), corresponding to κ varying from ~0.5% for bare lattice to about 2% for $\varepsilon_{x0} = 0.4$ nm.

Most NSLS-II calculations have been performed with the code ZAP [6.2.20], which implements the 2D procedure of the B–M theory [6.2.32], i.e., the vertical emittance is assumed dominated by coupling. We used 500 mA for the total ring current, and assumed it uniformly distributed into 80% of the 500 MHz RF buckets. As we changed the amount of radiation losses, the RF voltage was adjusted to keep the RF energy acceptance constant at 3%. Electron beam parameters in the absence of IBS, used as input to ZAP (such as horizontal emittance, energy spread, bunch length, and radiation damping times) were calculated analytically by scaling bare lattice values by the amount of radiation losses. The results given by ZAP are shown in Figure 6.2.10.
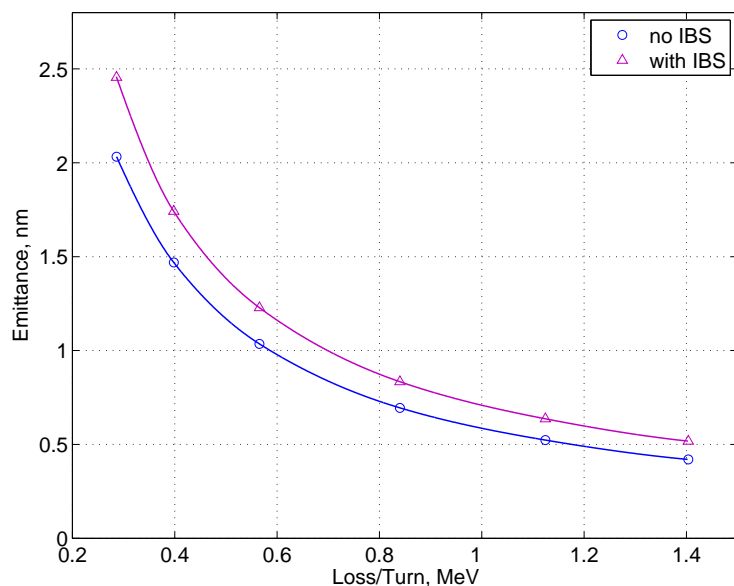

Figure 6.2.10   Horizontal emittance vs. total SR loss.

Note that the IBS-induced relative emittance blow-up does not exceed 20%, and remains fairly independent of the amount of radiation losses (and hence the emittance). This implies that for smaller emittances, increased IBS rates due to denser bunches are offset by the increase in radiation damping. This is quite contrary to a more typical situation in a storage ring light source not dominated by IDs, where

decreasing the emittance by adjusting the lattice (and hence keeping the SR rates fixed) can result in an increase of IBS-induced emittance blow-up. We have also found that the IBS rise times calculated by ZAP are in reasonable agreement (better than 50 %) with the estimates we have done using Bane's formalism.

Note that the results presented in Figure 6.2.10 are based on several conservative assumptions. First, calculations are performed at zero-current bunch length, while in reality the bunch will be longer, due to potential well distortion and the harmonic RF system. At even higher single-bunch currents, used in special operating modes, the microwave instability will result in an even stronger increase in bunch length as well as energy spread, reducing the IBS effect further. In addition, the calculations of Coulomb log that are used in ZAP use $b_{max} = \sigma_x$ and do not include the tail-cut procedure. As a result, the Coulomb log value ZAP assumes for NSLS-II parameters is about 17, while more recent estimates [6.2.33] that include the cut would reduce it to about 10.

We have also done some cross-checks of the bare lattice case using the SAD code from KEK [6.2.36]. SAD has been extensively benchmarked against the experimental results from the ultra-low emittance ATF storage ring. SAD does include the tail-cut, so it results in smaller IBS induced blow-up compared to ZAP. However, when scaled for the Coulomb log, the codes are in good agreement. SAD allows for full 3D treatment of IBS and will be used in the future to study the effects of vertical dispersion for NSLS-II.

To summarize, our calculations to date indicate that under pessimistic assumptions, IBS-induced relative emittance blow-up for NSLS-II should not exceed 20% at nominal bunch intensity and therefore it should not present a problem. Furthermore, we have found the magnitude of the blow-up to be fairly independent of the NSLS-II emittance, since the increased IBS rates for denser bunches are compensated by faster radiation damping. Future studies will include accounting for a more comprehensive ID makeup, considering the effects of vertical dispersion, and further developing some models of bunch lengthening.

6.2.6   Touschek Lifetime

The beam lifetime in most modern synchrotron radiation sources is limited by the Touschek effect, which describes the collision of two electrons inside a bunch, leading to momentum transfer from the transverse (usually horizontal) plane into the longitudinal direction. If the resulting longitudinal momentum exceeds the momentum acceptance of the accelerator, these particles are lost.

The Touschek lifetime is calculated as [6.2.37],

$$\frac{1}{\tau} = \frac{r_e^2 cq}{8\pi e \gamma^3 \sigma_s} \cdot \frac{1}{C} \cdot \oint_C \frac{F((\delta_{acc}(s)/\gamma \sigma_{x'}(s))^2)}{\sigma_x(s)\sigma_{x'}(s)\sigma_z(s)\delta_{acc}^2(s)} ds, \tag{6.2-29}$$

where r_e denotes the classical electron radius, q the bunch charge, σ_s the RMS bunch length, C the circumference of the storage ring, and $\sigma_x(s)$ and $\sigma_z(s)$ the RMS horizontal and vertical beam radii, including the dispersion term.

$$\sigma_{x'}(s) = \frac{\varepsilon_x}{\sigma_x(s)} \sqrt{1 + \frac{H(s)\sigma_\delta^2}{\varepsilon_x}} \tag{6.2-30}$$

is the RMS beam divergence for $\alpha_x = 0$, with

$$H(s) = \gamma_x \eta^2 + 2\alpha_x \eta \eta' + \beta_x \eta'^2 \tag{6.2-31}$$

the chromatic invariant. The function F(x) is defined as

$$F(x) = \int_0^1 (\frac{2}{u} - \ln\frac{1}{u} - 2) \cdot \exp(-x/u) du. \tag{6.2-32}$$

While the Touschek lifetime depends linearly on the bunch length as well as on the vertical beamsize, its dependence on the horizontal beamsize (or emittance) is more complicated. For large horizontal beamsize, the particle density of the bunch becomes very small, thus greatly decreasing the probability of two electrons colliding. On the other hand, a large horizontal emittance results in large horizontal momenta that can be transferred into the longitudinal plane due to a Touschek scattering event. The dependence of the resulting Touschek lifetime on horizontal emittance is illustrated in Figure 6.2.11.
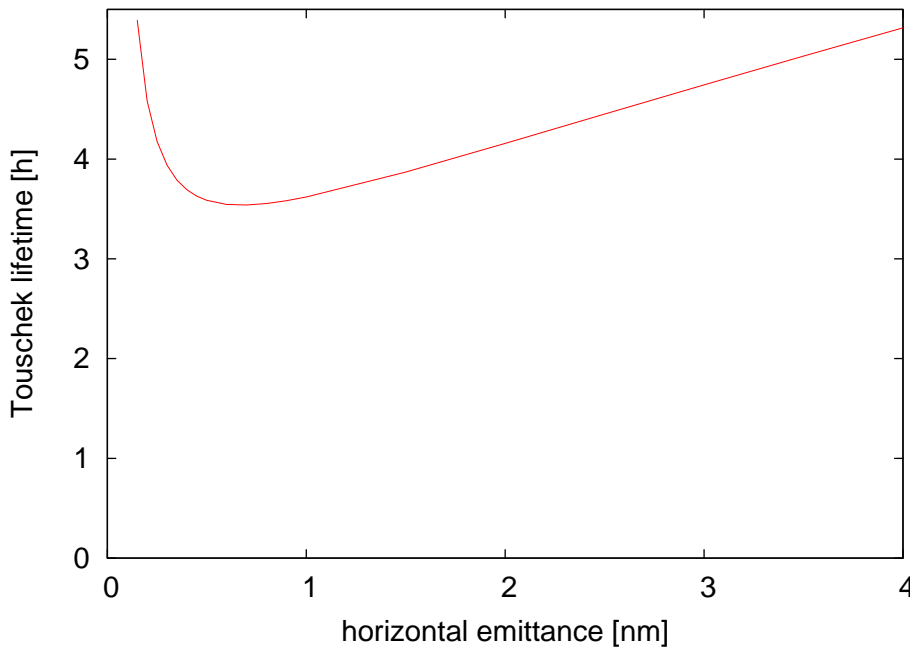
Figure 6.2.11 Touschek lifetime vs. horizontal emittance.

Experience at facilities like ALS and SLS has shown that nonlinear betatron coupling plays a significant role in limiting the momentum acceptance of the storage ring, especially in the presence of small vertical apertures due to small-gap insertion devices. Therefore, tracking has been performed using the TRACY-2 code. Since Touschek scattering occurs near the center of the bunch, the momentum acceptance δ_{acc} needs to be determined for particles starting at a longitudinal position s with coordinates $x = x' = y = y' = 0$. In general, this yields different momentum acceptances δ_{acc}^+ for positive and δ_{acc}^- for negative momenta, resulting in different Touschek lifetimes τ^+ and τ^-. Based on these two results, the total Touschek lifetime τ_{tot} is computed as

$$\frac{1}{\tau_{tot}} = \frac{1}{2} \cdot \left(\frac{1}{\tau^+} + \frac{1}{\tau^-} \right). \tag{6.2-33}$$

The Touschek lifetime was calculated for four different combinations of RF voltage and vertical aperture in the long straights, 2.5 MV and 5.0 MV in combination with ±2.5 mm and ±5.0 mm vertical aperture. The resulting momentum acceptances vs. longitudinal start position *s* around the ring are shown in Figure 6.2.12.
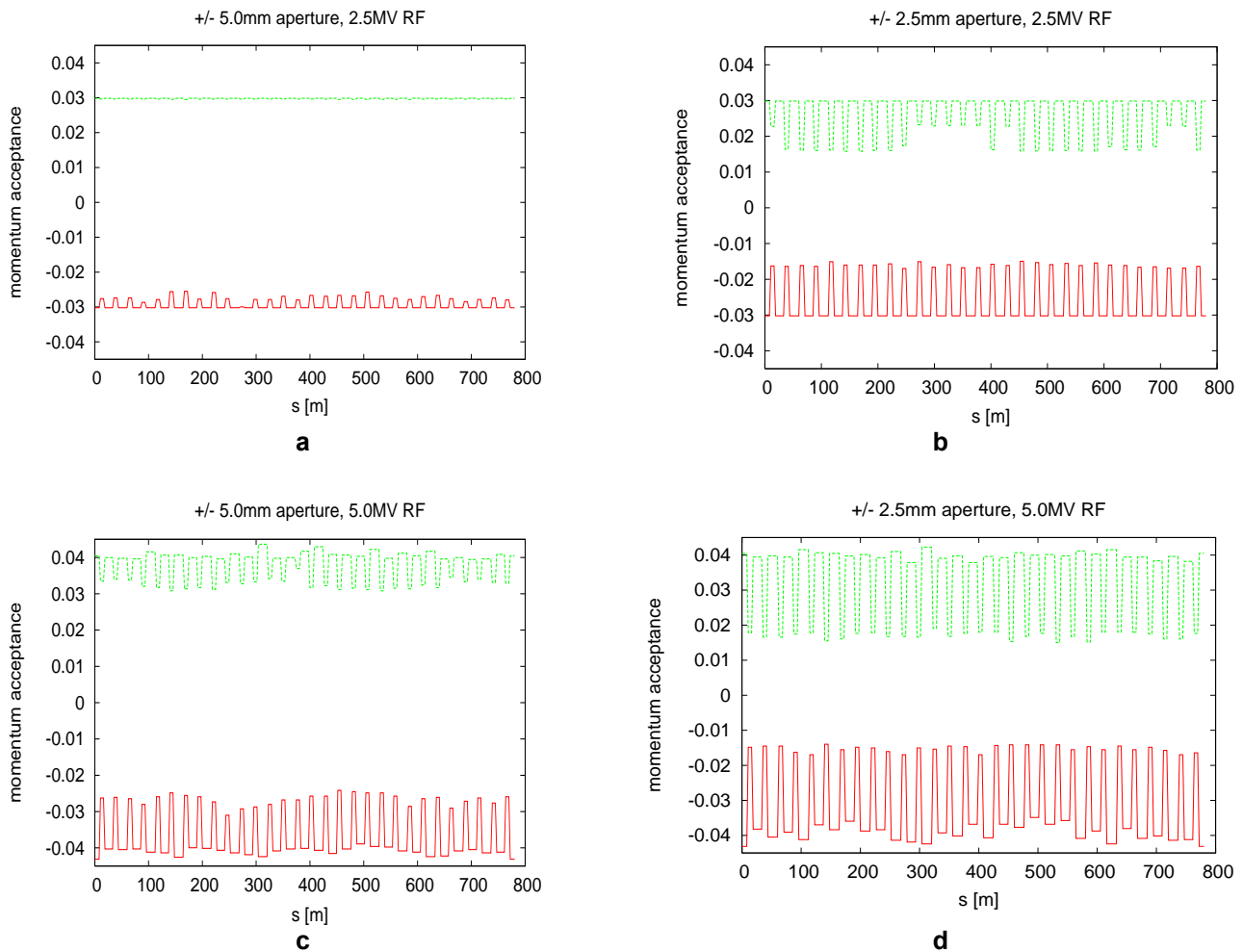
Figure 6.2.12 Momentum acceptance for: a) minimum vertical aperture of ± 5 mm and 2.5 MV RF voltage; b) minimum vertical aperture of ± 2.5 mm and 2.5 MV RF voltage; c) minimum vertical aperture of ± 5 mm and 5.0 MV RF voltage; and d) minimum vertical aperture of ± 2.5 mm and 5.0 MV RF voltage.

At the nominal RF voltage of 2.5 MV, which provides an RF energy acceptance of 3%, the resulting Touschek lifetime with a ±1.5 m long, ±5.0 mm vertical aperture in the short straights is 2.5 hours. When the aperture is reduced to ±2.5 mm, the Touschek lifetime drops by nearly a factor of two, to 1.3 hours. Doubling the RF voltage to 5.0 MV results in a Touschek lifetime of 1.1 hours for the ±2.5 mm aperture, and 3.6 hours for the ±5.0 mm aperture. This counterintuitive behavior is attributed to the decreasing bunch length at higher RF voltage, 2.1 mm vs. 3.0 mm, which results in a higher electron density within the bunch, thus overcompensating the effect of the larger momentum acceptance.

Assuming a constant RMS bunch length of 5.0 mm independent of RF voltage, which may be achieved by damping wigglers, the Touschek lifetimes are 2.2 hours and 4.2 hours for ±2.5 mm and ±5.0 mm vertical aperture, respectively, in the 2.5 MV RF voltage case. At the raised RF voltage of 5.0 MV, these lifetimes increase to 2.7 hours for the ±2.5 mm aperture, and 8.7 hours for the ±5.0 mm aperture.

6.2.7   Landau Cavity

Let us begin by reviewing the operation of a higher-harmonic, bunch-lengthening cavity (HHC) [6.2.38]. The fundamental cavity operates at an angular frequency, $\omega_{rf} = h\omega_0$, where h is an integer and $\omega_0 = 2\pi/T_0$ is the angular frequency of revolution. Assuming the Landau cavity is operating at the nth harmonic of the frequency of the fundamental RF, the voltage seen by an electron with temporal deviation τ is

$$V(\tau) = V_0 \left[\sin\left(\omega_{rf}\tau + \phi_s\right) + \kappa \sin\left(n\omega_{rf}\tau + \phi_n\right) \right].$$
(6.2-34)

In the ideal operation of such a cavity, one chooses to satisfy the conditions

$$U_0 = V_0 \left[\sin\phi_s + \kappa \sin\phi_n \right]$$
$$0 = \cos\phi_s + n\kappa\cos\phi_n$$
$$0 = \sin\phi_s + n^2\kappa\sin\phi_n,$$
(6.2-35)

where energy loss (U_0) and gain are balanced, and the first and second derivatives of the waveform are set to zero, at zero phase. In this case, the voltage has the form

$$V(\tau) = \cos\phi_s \left(\sin\omega_{rf}\tau - \frac{1}{n}\sin n\omega_{rf}\tau \right) + \sin\phi_s \left(\cos\omega_{rf}\tau - \frac{1}{n^2}\cos n\omega_{rf}\tau \right).$$
(6.2-36)

Approximating this for small τ yields the cubic form

$$V(\tau) \cong \cos\phi_s \left(\frac{n^2-1}{6} \right) \left(\omega_{rf}\tau\right)^3 + \sin\phi_s \left(1 - \frac{1}{n^2} \right).$$
(6.2-37)

As we will operate the Landau cavity passively, i.e., powered only by the beam, we cannot satisfy all of the ideal conditions. A superconducting cavity, in particular, absorbs very little power, implying that ϕ_n is fixed at $-\pi/2$, a few degrees from the ideal phase. Fortunately, this phase shift has little impact on the bunch profile. Figure 6.2.13 shows an unstretched bunch (blue) plotted with a stretched bunch (red) in a uniform fill with HHC detuning at +82 kHz.

A third-harmonic Landau cavity can be used to increase the electron bunch length without increasing the energy spread. This increases the Touschek lifetime and reduces the effect of intrabeam scattering on emittance. The nonlinear voltage resulting from the use of a Landau cavity results in a large increase in the dependence of the synchrotron tune on the amplitude of synchrotron oscillations. Energy transfer from potentially unstable resonant particles within a bunch to the surrounding nonresonant particles often provides a powerful mechanism for the suppression (Landau damping) of longitudinal coupled-bunch dipole modes. Also, the increase of bunch length can increase the stabilizing effect of positive chromaticity on the transverse dipole oscillations. The increased synchrotron tune spread can also help stabilize the higher-order head-tail modes.
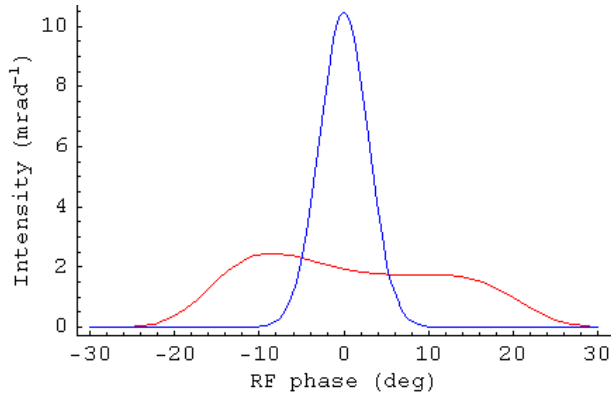
Figure 6.2.13   An unstretched bunch (blue) plotted with a stretched bunch (red) in a uniform fill with HHC detuning at +82 kHz.

If, as expected, there is a gap in the fill for ion clearing, then there will be a periodic transient induced in the cavity fields, causing non-uniform bunch profiles across the bunch train [6.2.39, 6.2.40, 6.2.41]. This effect is proportional to the *R/Q*s of the cavities, which favors superconducting cavities due both to their lower *R/Q* and their higher sustainable fields (requiring fewer cavities). Away from the center of the bunch train, bunches are much shorter and are peaked near the local synchronous phase, which can be a distance from the center of the nominal bucket. These peripheral bunches have shorter Touschek lifetime. This effect was found at ALS [6.2.40] to significantly reduce the overall lifetime of the beam. Figure 6.2.14 shows the bunch profiles for a 90% fill pattern and harmonic-cavity detuning of +82 kHz. Average RMS bunch length is 2.7 times the unstretched length.
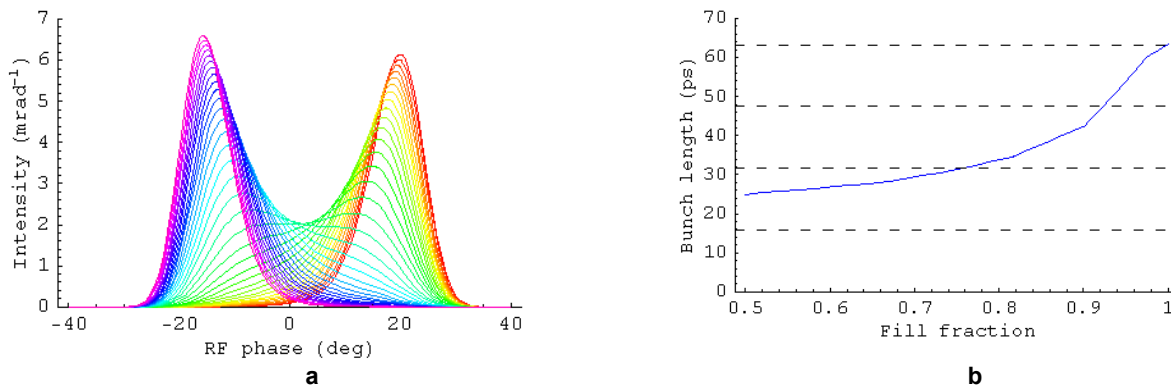
Figure 6.2.14   Bunch profiles. **a)** Along the bunch train for a 90% fill pattern and harmonic-cavity detuning of +82 kHz. **b)** Average bunch length as a function of fill fraction. Dashed lines are placed at multiples of the unstretched bunch length.

The average bunch length varies with the fill fraction. Smaller fill fractions aggravate the variation of bunch shapes along the train. Figure 6.2.14b shows the average bunch length as a function of fill fraction with cavities detuned to 82 kHz. Dashed lines are placed at multiples of the unstretched bunch length.

Bunch lengths vary with position along the train, being greatest near the center. In Figure 6.2.15a, each trace corresponds to a particular cavity field. From bottom to top, the detunings are +120, 105, 92, 85, 82, and 79 kHz. Dashed lines are drawn at multiples of the unstretched bunch length. As HHC fields increase, bunch and lifetimes tend to increase; but bunches that become double peaked, however, can show large RMS bunch length but reduced lifetime. Bunch centroid phases (arrival times) also vary with position along the train. In Figure 6.2.15b, the phase along the train is plotted for a 90% fill and the same fields as in Figure 6.2.15a. The

synchronous phase is a sensitive function of local shifts in the RF wave due to the $(\omega_{rf}t)^3$ inflection; that sensitivity increases with increasing HHC field, even beyond the optimal HHC field.
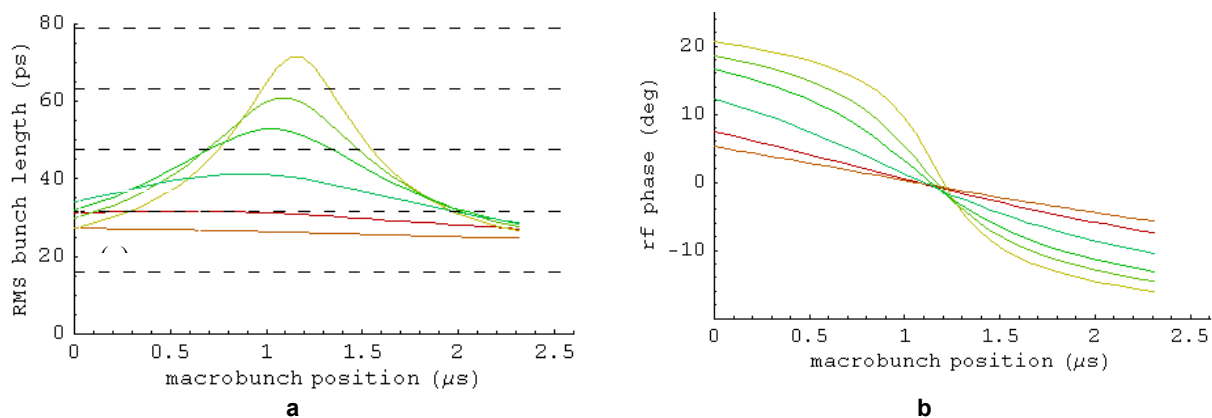

Figure 6.2.15 **a)** Each trace corresponds to a particular cavity field. From bottom to top, the detunings are +120, 105, 92, 85, 82, and 79 kHz. Dashed lines are drawn at multiples of the unstretched bunch length. **b)** Phase along the train is plotted for a 90% fill and the same fields as in **a**.

The HHC field required for nominal bunch stretching is 1.17 MV. Since the maximum sustained fields reached in HHCs developed to date are 0.5 MV per cell in 1500 MHz cavities, three cells are required, either in three single-cell cavities, or two double-cell cavities. The performance plots above were computed assuming three cells. In practice, significantly longer lifetimes are achievable by operating the HHCs at fields slightly higher than the ideal described above, as the NSLS VUV ring is operated now. The useful fields are limited by the onset of higher-order longitudinal instabilities.

The Day 1 configuration employs a reduced number of damping wigglers and consequently requires less main- and harmonic-cavity fields. Since two harmonic-cavity cells are capable of providing 1.0 MV of the 1.1 MV nominally required during this phase, most of the benefit of the HHC is obtained from this one cavity. Figures 6.2.16a and b show the bunch profiles and lengths expected by operating two cells at about 1.0 MV total field, but with the full complement of wigglers. Since the impedance is only that of two cells, the impact of the bunch train on bunch profiles is reduced in proportion. Fill fraction and detuning are 90% and +67.67 kHz, respectively. There is two-fold gain in the average bunch length.
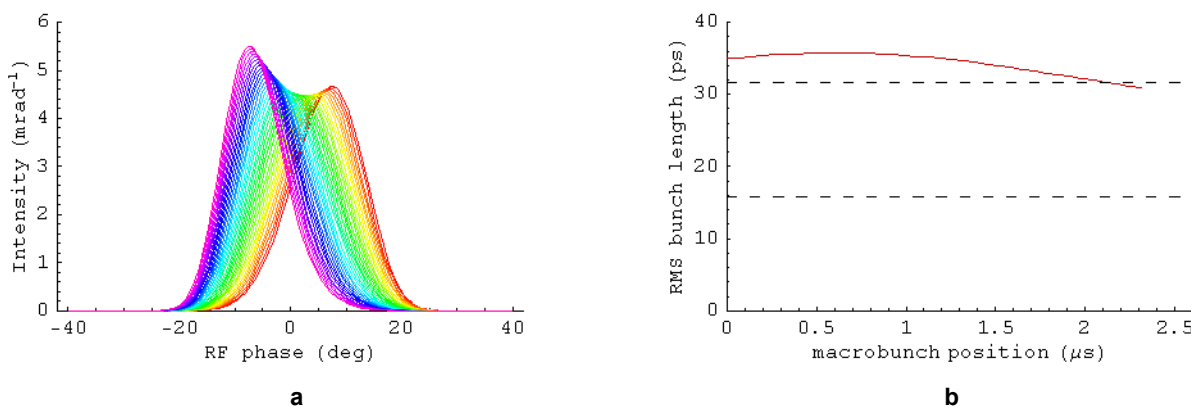

Figure 6.2.16 Bunch profiles (**a**) and lengths (**b**) expected by operating two cells at about 1.0 MV total field, but with the full complement of wigglers.

Compressed bunch operation for timing experiments is possible by detuning the HHC below the RF harmonic, instead of above. The bunch length at small single-bunch currents is reduced to less than half the bunch length without a harmonic cavity. But at finite currents, potential-well distortion by the ring's broadband impedance, and microwave instability, if present, inevitably increases the bunch lengths. The short bunch lengths may also permit higher-frequency, higher-order modes in the HHC and elsewhere to drive coupled-bunch instabilities. Short-bunch operation may drive the need for longitudinal feedback.

NSLS-II can opt to use an active HHC, i.e., HHCs that are powered by conventional amplifiers, such as was done in the NSLS VUV ring. In this configuration, resistive and reactive power are applied to control the phase of the cavity relative to the beam, almost arbitrarily. But the numerical results presented above, and the example of the VUV ring, which uses an active system to set the cavity (a NC cavity) phase to –90 degrees, show that the impact of the difference between –90 degrees and the nominal phase for stretching, even in the uniform-fill case, is insignificant. And in a fill with a significant gap, the improvement in the profiles is swamped by the effect of the periodic transient. Furthermore, an active system would require development of a cavity with an input coupler, could introduce multipacting, and could complicate HOM suppression. For these reasons, a passive cavity has been selected for NSLS-II.

6.2.8   Conclusions

Using a simplified model of the storage ring impedance, we have estimated the instability thresholds for NSLS-II. The longitudinal motion is found to be stable. At zero chromaticity, the transverse resistive wall impedance will make the beam unstable at 15 mA average current. According to simulations, increasing the chromaticity above 4 should provide stability. However, there is concern about the effect on DA at higher chromaticity; therefore, we will also use a transverse feedback system.

We have made significant progress in calculating the impedance of the storage ring using GdfidL. The results obtained thus far are within the envelope of the model we have used to estimate thresholds. Thus, we believe our model is conservative. We plan to complete the calculation of the storage ring impedance and then use the numerically determined wakefields in a tracking code to determine the instability thresholds.

Calculations indicate that the increase of emittance due to intrabeam scattering should be less than 20%. For the present state of the lattice design, the 5 mm full vertical aperture of the in-vacuum undulators reduces the energy acceptance from 3% down to 1.5% at large-dispersion locations. This results in a Touschek lifetime of 2 hrs. We plan to investigate whether further optimization of the working point can reduce the nonlinear coupling and thus increase the Touschek lifetime. Use of a Landau third-harmonic bunch lengthening cavity is planned. This will reduce the effect of intrabeam scattering on the emittance, lengthen the Touschek lifetime to more than 3 hrs, and provide enhanced longitudinal and transverse stability.

References

[6.2.1]   A.W. Chao, *Physics of Collective Beam Instabilities in High Energy Accelerators* (Wiley, NY, 1993).

[6.2.2]   See, e.g., K. Harkay, R. Nagaoka, J.L. Revol, and T. Nakamura, "A Preliminary Comparison of Beam Instabilities among ESRF, APS, and SPrinG-8 X-Ray Storage Ring Light Sources, Proc. EPAC2002, 1505 (2002).

[6.2.3]   W. Bruns, http://www.gdfidl.de.

[6.2.4]   G.V. Stupakov, "Wake and Impedance," SLAC-PUB-8683 (2000).

[6.2.5]   B. Zotter and S.A. Kheifets, *Impedances and Wakes in High-Energy Particle Accelerators* (World Scientific Publishing Co., Singapore, 1998).

[6.2.6]   A. Chao, S. Heifets, and B. Zotter, "Tune Shifts of Bunch Trains due to Vacuum Chambers Without Circular Symmetry," *Phys. Rev. ST-AB* **5**, 111001 (2002).

[6.2.7] K. Bane, and M. Sands, "Short-Range Resistive Wall Wakefields," AIP Conf. Proc. **367**, 131 (1995).

[6.2.8] B. Podobedov, "Extreme Anomalous Skin Effect Wakefields," unpublished.

[6.2.9] Y.C. Chae, "The Impedance Database and its Applications to the APS Storage Ring," Proc. PAC2005, 3017.

[6.2.10] See, e.g., S. Krinsky, "Simulation of Transverse Instabilities in the NSLS-II Storage Ring," BNL-75019-2005-IR.

[6.2.11] J. Haissinski, *Il Nuovo Cimento* **18**, 72 (1973).

[6.2.12] K. Oide and K. Yokoya, "Longitudinal Single-Bunch Instability in Electron Storage Ring," KEK Preprint 90-10 (1990).

[6.2.13] M. Borland, ELEGANT, http://www.aps.anl.gov/Accelerator_Systems_Division/Operations_Analysis/software.shtml

[6.2.14] D. Boussard, CERN LABII/RF/INT/75-2 (1975).

[6.2.15] M. Blaskiewicz, "The TRANFT User's Manual," unpublished.

[6.2.16] J. Kirchgessner, Part. Accel. **46**, 151 (1995).

[6.2.17] M. de Jong et al., *J. Microwave Power Electromagnetic Energy* **27**, 136 (1992).

[6.2.18] K. Halbach and R.F. Holsinger, "SUPERFISH-A Computer Program for Evaluation of RF Cavities with Cylinderical Symmetry," *Part. Accel.* **7**, 213 (1976).

[6.2.19] Mark deJong, private communication.

[6.2.20] M.S. Zisman, S. Chattopadhyay, and J.J. Bisognano, "ZAP User's Manual," LBL-21270, UC-28 (1986), 168.

[6.2.21] R. Nagaoka, "Numerical Evaluation of Geometric Impedance for SOLEIL," Proc. EPAC2004, 2038.

[6.2.22] K. Yokoya, "Resisitive Wall Impedance of Beam Pipes of General Cross Section," *Part. Accel.* **41**, 221 (1993).

[6.2.23] G. Stupakov, "Coupling Impedance of a Long Slot and an Array of Slots in a Circular Vacuum Chamber," *Phys. Rev. E* **51**, 3515 (1995).

[6.2.24] E. Karantzoulis, V. Smaluk and L. Tosi, "Broad Band Impedance Measurements on the Electron Storage Ring ELETTRA," *Phys. Rev. ST-AB* **6**, 030703 (2003).

[6.2.25] B. Podobedov and S. Krinsky, "Transverse Impedance of Elliptical Cross-Section Tapers," Proc. EPAC2006, 2973 (2006).

[6.2.26] A. Blednykh, S. Krinsky, B. Podobedov, and J.M. Wang, "Transverse Impedance for Small-Gap Undulators for NSLS-II," Proc. EPAC2006, 2973 (2006).

[6.2.27] P. Stefan et al., "Small-Gap Undulator Research at the NSLS: Concepts and Results." *Nucl. Instr. Meth. A* **412**, 161 (1998).

[6.2.28] A. Blednykh, "Trapped Modes in an Elliptic Vacuum Chamber," *Nucl. Instrum. Meth. A*.

[6.2.29] P.J. Chou, "Numerical Analysis of Higher-Order Modes for Superconducting RF Cavity at SRRC," Proc. Pac2003, 1368.

[6.2.30] P.J. Chou, J. Chen, K.-T. Hsu, C.-C. Kuo, C. Wang, and M.-H. Wang, "Collective Effects in the TLS Storage Ring after the Installation of Superconducting Cavity," Proc. PAC2005, 2360.

[6.2.31] A. Piwinski Tech. Rep. HEAC 74, Stanford, 1974; See Also A. Piwinski in A. Chao and M. Tigner, *Handbook of Acclerator Physics*, World Scientific (1999) 125.

[6.2.32] J. Bjorken and S. Mtingwa, "Intrabeam Scattering," *Part. Accel.* **13**, 115 (1983).

[6.2.33] K. Kubo and K. Oide, "Intrabeam Scattering Formulas for High Energy Beams," *Phys. Rev. ST-AB* **4**, 124401 (2001).

[6.2.34] K.L.F. Bane, "A Simplified Model of Intrabeam Scattering," SLAC-PUB-9226 (2002).

[6.2.35] T. Raubenheimer, *Part. Accel.* **45**, 111 (1994).

[6.2.36] K. Oide, *SAD User's Guide*.

[6.2.37] A. Streun, "Momentum Acceptance and Touschek lifetime," SLS Note 18/97.

[6.2.38] A. Hofmann and S. Meyers, "Beam Dynamics in a Double RF System," Proc. 11th International Conference on High Energy Accelerators, Geneva (Birkhauser Verlag, Basel, (1980), p 160.

[6.2.39] N. Towne, "Stretched Bunch Shapes in the NSLS VUV Ring," Proc. PAC1999 (1999) 2828.

[6.2.40] J.M. Byrd, S. De Santis, J. Jacob, and V. Serriere, "Transient Beam Loading Effects in Harmonic RF Systems for Light Sources," *Phys. Rev. ST-AB* **5**, 092001 (2002).

[6.2.41] A. Blednykh, S. Krinsky, B. Podobedov, J. Rose, N.A. Towne, and J.M. Wang, "Harmonic Cavity Performance for NSLS-II," Proc. PAC2005 (2005) 2544.

6.3   Orbit Feedback System

The linac is located on the same level as the booster. In future design we will determine whether the linac is installed on the floor supports or suspended from the ceiling.

6.3.1   Requirements for Beam Stability

To realize the benefits of the high brightness and small beam sizes of NSLS-II, it is essential that the photon beams are exceedingly stable, assuring constant intensity after apertures, constant photon energy after monochromators, and minimal photon source size and highly precise steering accuracy for focusing on small samples. For example, in the common case of 1:1 focusing optics, positional stability of the photon beam on the sample is directly related to that of the electron beam. The position of the photon beam should be stable to a level of $\Delta_y/\sigma_y \sim 10\%$. We require beam motion of no more than 10% of beamsize, particularly in the frequency range from ~10 mHz to 100 Hz. This tolerance has been adopted by many synchrotron radiation laboratories. Since the minimum vertical beta function is about 1 m, when we take the vertical emittance as $10^{-10}/4\pi$ m, the vertical beamsize is 2.7 μm RMS. Therefore, the beam position stability should be ~0.3 μm in the short straight section.

6.3.2   Fast Orbit Motion with Feedback Loop On and Off

For the NSLS-II ring with a DBA30 lattice as shown in Figure 6.1.1 (only half a super-period is shown), the performance of a fast, closed-orbit feedback system with 120 BPMs and 120 correction trims was calculated (for BPM positions, see Figures 6.1.4 – 6.1.6).

We averaged over 400 different sets of random numbers for all the quads, assuming they vibrate randomly with uncorrelated RMS displacement of 1 μm. The resulting beam RMS motion $\sigma_{\Delta y}$ is shown in blue in Figure 6.3.1. It is well approximated by the function $14\sqrt{\beta_y[m]}$ μm, which is shown in green.
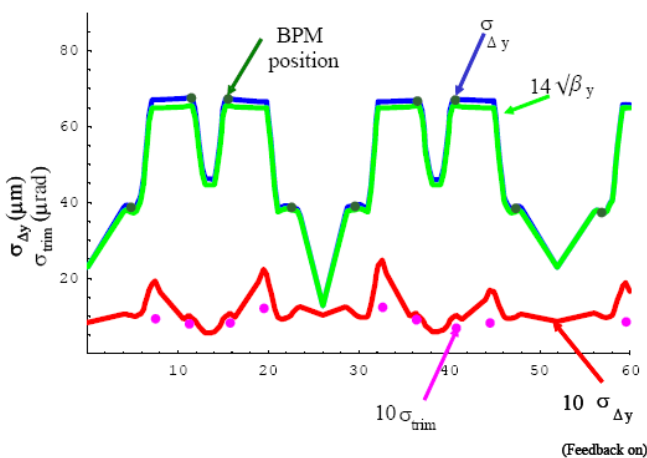

Figure 6.3.1   Open (green) and closed-loop (red) RMS orbit motion and RMS corrector strengths in the feedback loop. The x axis is the distance along the ring circumference, in meters.

For each set of Gaussian random errors for the quad vibration and BPM vibration, all with RMS displacement of 1 μm, the open-loop BPM signal was calculated, then the SVD matrix was used to calculate the corrector strength, and finally the orbit with the feedback loop closed. After averaging over 400 random samples, the residual RMS beam motion shown in Figure 6.3.1 was obtained, represented by the red curve. The open-loop BPM signal and the corrector strength used in the feedback loop are marked by dark green and purple dots, respectively.

The residual orbit is multiplied by a factor of 10 in Figure 6.3.1 to make it visible. The height of the purple dots represents 10 times the RMS strength of the correctors, in units of μrad. The figure shows that the feedback loop reduces the beam motion at the center of the long straight section ($z = 0$) from 25 μm to 0.7 μm. The maximum RMS corrector strength is on the order of 1.2 μrad.

The tolerance on the floor motion required to keep beam motion within 10% of beamsize was determined using the following assumptions: 1) $\varepsilon_y = 0.1$ nm/4π, 2) all the quads and BPMs mounted on the girders have uncorrelated random vibration of 0.4 μm, and 3) the BPM electronic noise is negligible. Averaging over 400 samples gave the ratio of the vertical beam motion divided by the RMS beamsize as a function of z in the ring, shown in Figure 6.3.2. At the 5 m straight section, the ratio of beam motion over beamsize is 11%. This implies that the tolerance for the quad vibration is <0.3 μm RMS. This calculation ignored the fact that for low-frequency ground motion, the movement of different components mounted on the girders can be correlated, since the sound wavelength at low frequency can be larger than the girder dimension. Actually, simulation for correlated movement of quads mounted on the same girder shows a reduced amplification factor, since the quads moving together tend to cancel each other [6.3.1]. The noise caused by ripples in the power supply corrector magnet current was also ignored. Compared with this effect, the orbit motion due to the vibration of BPMs is much more difficult to suppress. Actually, it is very difficult to reduce the beam motion to much less than the amplitude of the BPM vibration. Similar calculations for horizontal orbit show that if quads and BPMs have random vibration of RMS value 1 μm, the residual RMS value of beam motion is 0.7 μm at the straight sections. Since the horizontal beamsize is much larger than the vertical beamsize, the horizontal requirement is much easier to satisfy than the vertical.

Figure 6.3.2   Closed-loop orbit deviation normalized by beamsize.

$Z\,(m)$
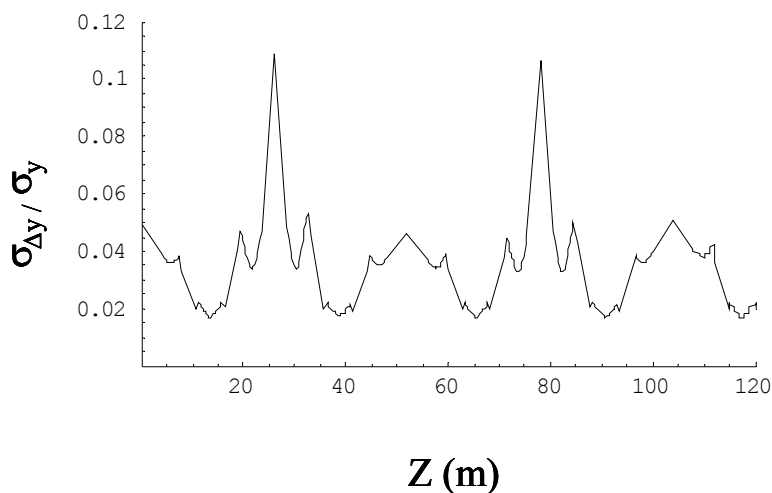
The beam motion due to power supply noise in a digital feedback system is determined by the voltage corresponding to the last bit of the power supply and the power supply current noise itself [6.3.1, 6.3.2]. Similar to the vibration simulation, we find that if we require beam motion (due to trim noise at the beam waist where $\beta_y = 1$ m) to be less than 0.25 μm, the RMS trim noise should be less than 10 nrad. Hence the

power supply should be accurate to 10 n-rad/0.29 = 30 nrad. If the maximum trim strength is 1 mrad, we need the last digit to be 30 ppm so the RMS noise should be less than 10 ppm.

6.3.3   Ground Movement at the NSLS-II Site

Floor vibration measurement near beamline X5 at the NSLS site on Feb. 22, 2006 is shown in figure 6.3.3. The measurement is the RMS value of vibration above 0.5 Hz. Note that between 10 p.m. (22 hrs) and midnight, the vibration reached a minimum of about 70 nm. It reached a maximum near noontime of about 200 nm. Since the sound speed in concrete is 3 km/s below 0.5 Hz, the effect of the vibration below 0.5 Hz is not critical.
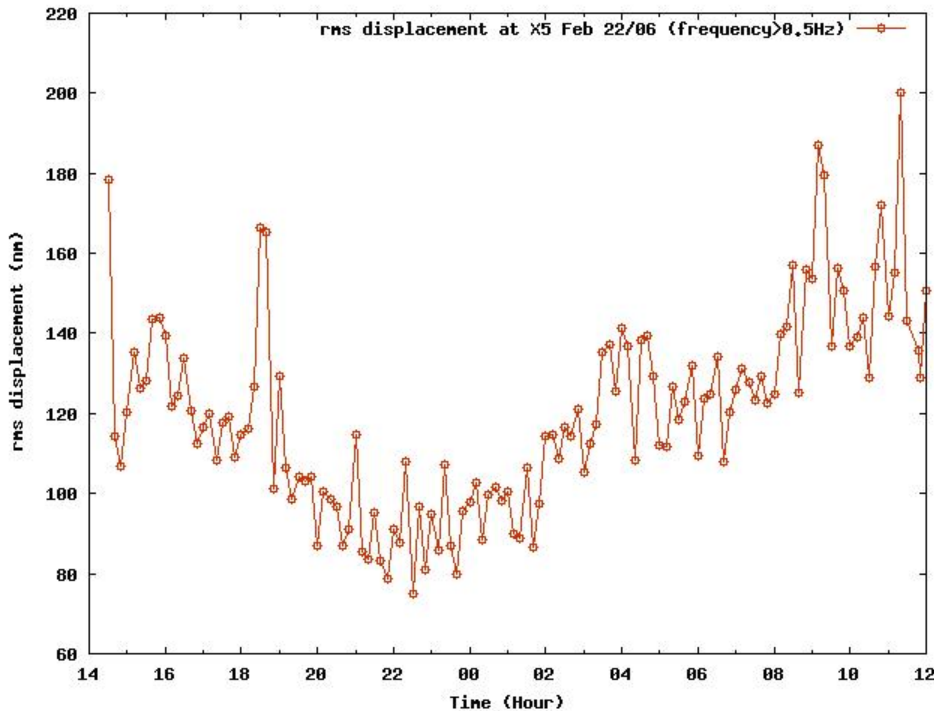
Figure 6.3.3   Floor vibration measurement near beamline X5 at the NSLS site on Feb. 22, 2006.

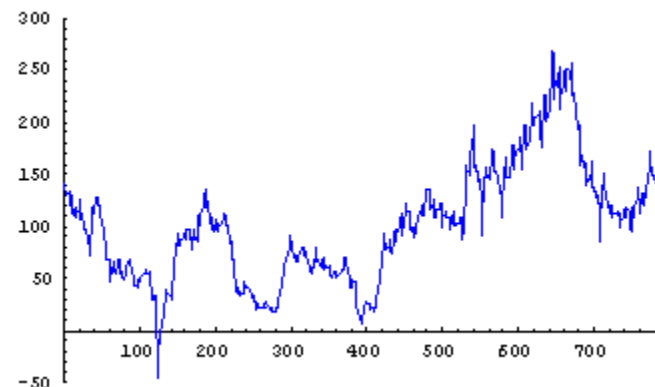#### 6.3.3.1   Long-Term Ground Movement

As for long-term ground movement at the BNL site, measurements carried out at RHIC between 1997 and 2002 show the coefficient A in the ATL law is $A \cong 3\times10^{-18}$ m^2/m/s [6.3.4, 6.3.5]. Based on this, we estimate that the RMS movement within the 248 m diameter of NSLS-II over a half-year is about 110 m.

We simulated the performance of the slow feedback system on long-term ground motion using the ATL law [6.3.6] at the NSLS-II site over a half year, with the same set of BPMs and correctors as mentioned in Section 6.3.2. The results are shown in Figure 6.3.4. In this specific example, the maximum ground movement was 250 μm, with an RMS value of 60 μm.

Feedback Loop Off

Electron beam motion (vertical) without feedback loop; maximum is 800 µm.
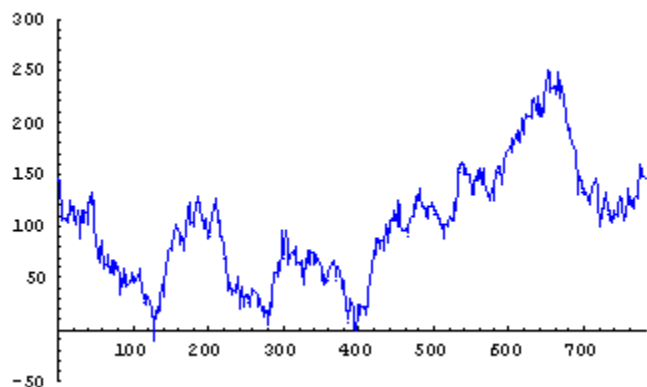
Floor motion around the ring. While the RMS maximum value around the ring for a large number of examples is 100 µm, in this specific example the maximum is 250 µm.
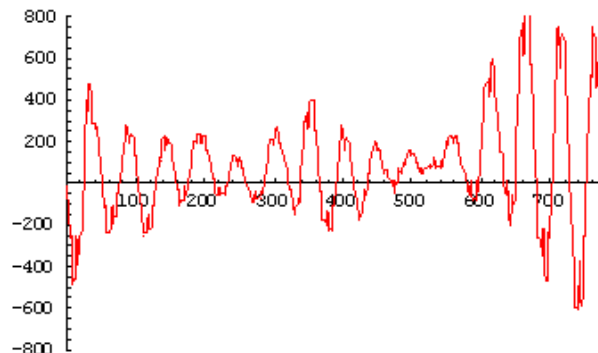
Feedback Loop On

Electron beam motion relative to floor (the difference between the two plots on the left) with the feedback loop on; maximum is 60 µm, RMS 12 µm.

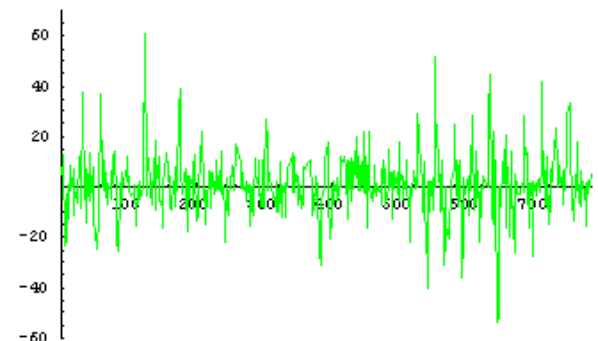Electron beam motion with the feedback loop on.

Figure 6.3.4 Simulated long-term ground motion and electron beam motion within half a year, with feedback system on and off. The horizontal axis is the distance along the circumference. Although the x-axis on the fourth plot is difficult to read, it aligns with the x-axis of the plot above it and the same labels apply to both.

The maximum relative movement between the beam and the ground was about 800 µm without feedback; with feedback, it was 60 µm with an RMS value of about 12 µm. Based on the ratio of 250 µm/12 µm, we estimate that, for the RMS value of the maximum ground movement of 110 µm across the diameter, the residual movement is about 5.3 µm over half a year. Hence, according to the ATL law, the residual RMS movement within a day should be reduced to about 0.4 µm.

If the orbit is realigned every six months, then within that half year the required corrector strength for the global orbit correction is about 0.1 mrad. (As mentioned in Section 6.3.2, to feedback on 1 µm movement, the required corrector strength is about 0.1 µrad.) To leave a margin for error, the maximum strength of the corrector is specified to be 0.5 to 1 mrad. As shown in Section 6.3.2, this requires the last bit of the power supply to be 30 ppm. To relax this condition, it is desirable have separate fast and slow feedback systems. This way, the slow feedback system correctors have a maximum strength of 0.5 to 1 mrad to handle the larger long-term motion, and the fast feedback system correctors have a lower maximum strength of 0.15 mrad;

thus, the last digit may be relaxed to 200 ppm. The fast feedback system uses the four correctors SL4, SD1, SD1, and S4 for each half super-period, as mentioned in Section 6.3.2. These correctors are located around stainless steel bellows, and hence can have high frequency response.

6.3.3.2   Temperature Stability

The air temperature stability in the storage ring tunnel is specified to be ±0.1ºC. Due to thermal expansion of the girder and vacuum chamber support system (~12 μm/m/ºC), the BPMs will move about ±1.2 μm. This motion is in the acceptable range everywhere in a super-period except in the 5 m and 8 m straight sections, where the BPM motion is required to be less than 0.3 μm (see Figure 6.3.2). A local feedback system will be used with two correctors on each side of an installed insertion device to stabilize the x-ray beam based on user's supplied feedback on its position. The local and global feedback systems will be decoupled, thus isolating the global orbit correction from the thermal displacements of the BPMs in the straight sections.

6.3.4   BPM Resolution and Noise Floor

A power density spectrum plot of measurement of orbit motion at NSLS using an RF BPM is reported in Figure 6.3.6, with beam motion shown in blue and the noise floor of the BPM in red. The plot shows that above 200 Hz, the beam motion is dominated by the noise floor. Hence, a feedback system with frequency higher than 200 Hz will not improve the orbit stability. The feedback system based on our BPM should have a cut-off point set below 200 Hz. Measurements at NSLS show that the vibration amplitude between 50 Hz and 200 Hz is less than 10 nm, which is negligibly small. Therefore, to relax the requirement on the feedback system bandwidth, the cut-off point is set at 60 Hz. A long-term drift test of the BPM offset is still needed, to show it is sufficiently small (lower than 0.2 μm). BPMs with better performance are available, and work in developing better BPMs is needed.
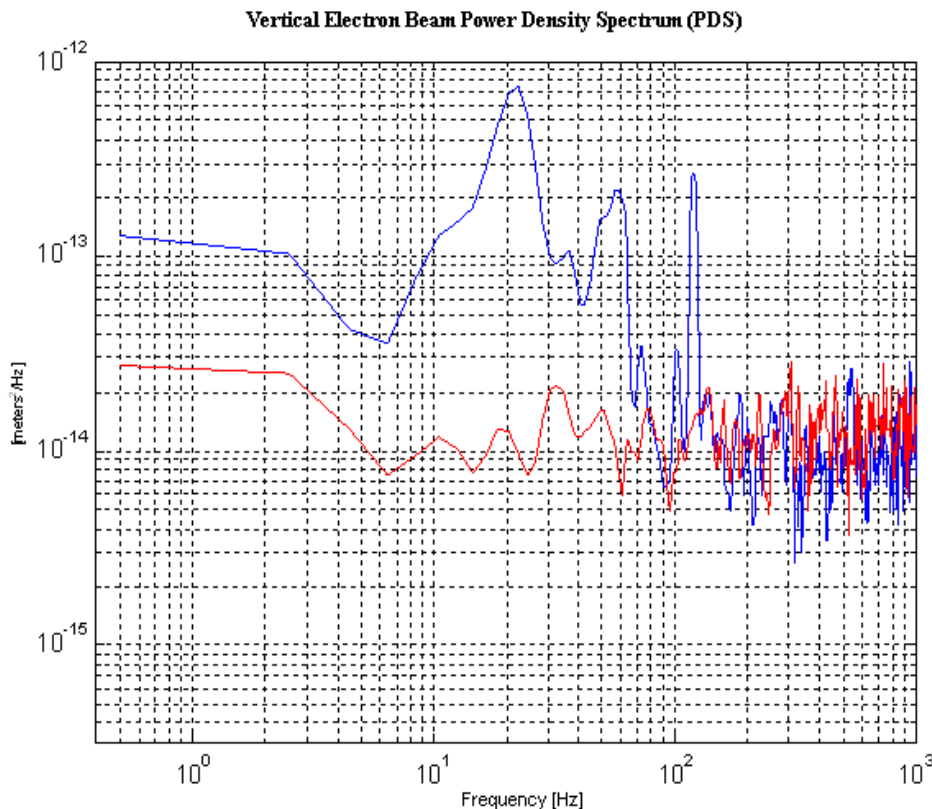

Figure 6.3.5   Power density spectrum of beam motion.

6.3.5   Requirements for the Feedback System

Based on these considerations, the ground vibration of 0.2 μm above 0.5 Hz satisfies the 0.3 μm requirement determined by the feedback system performance calculation presented in Section 6.3.2. However, since the ring tunnel temperature stability of ±0.1°C can only provide 0.5 μm girder stability, it is clearly a rather stringent requirement. As the most stringent requirement comes from the 5 m straight section, R&D work is needed to satisfy this condition. One approach is to develop local feedback systems for these sections and improve the temperature stability in the tunnel.

As mentioned in Section 6.3.4, the measured beam motion coincides with the BPM noise floor for frequencies higher than 200 Hz (see Figure 6.3.2). In addition, since most of the motion comes below 60 Hz, it is desirable to design the feedback system PID circuit to reach a 60 Hz bandwidth.

Because eddy currents are proportional to the thickness and electrical conductivity of materials, only thin laminations (1 mm thickness) or air coils should be used for correctors and the low-conductive materials preferred for vacuum chambers. Eddy currents in vacuum chambers usually impose the most critical bandwidth limitation on the feedback loop [6.3.1].

When designing the feedback system bandwidth, it is crucially important to design the vacuum chamber and power supplies for all the correctors to be used in the fast global feedback system such that they have the same frequency response. For the same reason, all four trims used in any one local feedback system should have the same frequency response. If the vacuum chambers or power supplies are very different for different correctors in the local bumps, or in the global feedback loop, it will be difficult to equalize the trim frequency response. Without excellent equalization, there will be interaction between the different systems; hence there will be instability, which may force us to narrow the bandwidth of the feedback system or lower the gain of the system. In addition, to avoid coupling between the fast global feedback system and the local feedback system, it is important to have at least one additional BPM and four fast correctors in all the straight sections with undulator beamlines, and to be sure that no global feedback system BPMs or fast correctors lie between them.

To maintain the dynamical aperture regardless of long-term ground movement requires the beam to stay within 50 μm of the center of the sextupoles. According to the simulation based on the ATL law, described in Section 6.3.2, if the ring is regularly realigned every six months, this can be achieved. RF frequency will also be used as an additional corrector to compensate for energy drifts.

The analysis in Section 6.3.2 also addresses the maximum strength for the trim correctors. Assuming the mechanical error when realigning the ring is 100 μm, the strength required for the feedback system trims is 120 μrad. Given a factor 2.5 margin, a 0.5 to 1 mrad strength should be sufficient for the slow feedback system. Because the fast and slow feedback systems are separate, and the maximum strength of the fast feedback system is lowered to 0.15 mrad, the analysis on the trims' last digit noise in Section 6.3.2 shows that the last digit can be relaxed to less than 200 ppm of the maximum strength.

References

[6.3.1] M. Borg, PAC '01, talk on IWBS'02, and EPAC 04 paper.
[6.3.2] J. A. Carwardine and F. R. Lenkszus, "Real-Time Orbit Feedback at the APS," p.12, 1997 beam instrumentation workshop at SSRL.
[6.3.3] Heiko Ehrlichmann, private communication (2/2006).
[6.3.4] Vladimir Shiltsev, "Space-Time Ground Diffusion: The ATL Law for Accelerators," DESY-MPY, Notkestrasse 85, 22603 Hamburg, Germany.
[6.3.5] Vadim Ptitsyn, private communication (7/2004).
[6.3.6] A. Walski, and N.J. Walker, Proceedings of 2003 PAC.